HUMBA: the Hundred Millikelvin Bolometer Array for 2 mm Continuum Observations

Dissertation

zur

Erlangung des Doktorgrades (Dr. rer. nat.)

der

Mathematisch-Naturwissenschaftlichen Fakultät

der

Rheinischen Friedrich-Wilhelms-Universität Bonn

vorgelegt von

Andrea Raccanelli

aus

Rom

Bonn, Juni 2003

Angefertigt mit Genehmigung der Mathematisch-Naturwissenschaftlichen Fakultät der Rheinischen Friedrich-Wilhelms-Universität Bonn

1. Referent: Prof. Dr. K. Menten
2. Referent: Prof. Dr. U. Klein

Tag der Promotion: 16.07.2003

Abstract

High resolution maps of the Sunyaev-Zel'dovich effect in clusters of galaxies offer a powerful tool for studying physics in clusters and cosmology. The Hundred Millikelvin Bolometer Array (HUMBA) for 2 mm continuum observation is a unique instrument devoted to the observations of the thermal Sunyaev-Zeldovich effect in cluster of galaxies. I report on my work on this instrument and on the results of test observations in November 2001 at the IRAM 30 m telescope.
The performance of HUMBA was seriously limited by an excess of low-frequency noise in the detectors. The source of this noise was investigated and found to originate in the continuously filled 1 K pot of the dilution unit. The noise could be eliminated by converting the helium coming from the main bath to its superfluid state before injecting it into the 1 K pot. The thermalization of the helium to the pot temperature is provided by a heat exchanger internal to the pot. The improvement to the dilution unit has been covered by a patent application.
After being tested with new detectors, HUMBA was installed at the IRAM 30 m telescope. During two days of tests on the sky, we observed the three bright, compact clusters of galaxies RXC J2228.6+2036, RXC J1023.6+0411, and RXC J1401.0+0252 and detected a SZ signal from two of them. Other objects, including the comet C/2000 WM1, Pluto and stars were also detected.
Our measurement on the clusters are compared to existing X-ray data from the ROSAT satellite. The Comptonization parameters derived from the 2 mm data are found to be in good agreement with those expected from X-ray data using an isothermal beta model.

Contents

Chapter 1

Sunyaev-Zel'dovich Effect in Galaxy Clusters

Clusters of galaxies are the largest gravitationally bound structures in the Universe. The number of galaxies they contain varies from the several thousand in a large cluster to a few galaxies in a group. The diameters of the larger clusters are in the range of 3 to 10 Mpc, and their mass is of the order of 10^{14} to 10^{15} solar masses, of which only a few percent is contained in galaxies. The majority of the gravitational mass is constitued of dark matter. The mass of the clusters forms a deep gravitational potential well in which the gas (15% to 20% of the total mass) must be very hot to form a stable extended atmosphere. This is what is observed in a number of large clusters in the X-ray band (see for example Sarazin 1986). The X-ray emission is extended and the gas responsible for it has a temperature in the range 10^7 to 10^8 K This is confirmed by the presence of spectral lines of highly ionized iron in the emission from the intracluster (IC) gas.

1.1 The Sunyaev-Zel'dovich effect

In 1972 Sunyaev & Zel'dovich argued that the hot intracluster medium should produce a measurable distortion in the spectrum of the cosmic microwave background (CMB) radiation via Compton scattering. This has come to be known as the thermal Sunyaev-Zel'dovich (SZ) effect, and it has been observed and measured in several clusters of galaxies. A detailed theoretical treatment, together with a discussion of the experimental results, can be found in the fundamental review by Birkinshaw (1999).

The bulk motion of the IC medium relative to the CMB rest frame produces another distortion in the CMB spectrum, giving rise to the so-called kinetic SZ effect. Due to its weakness, this second effect is more challenging to detect and is not discussed here. In both cases the effect is proportional to the inverse Compton (or equivalently Thompson) optical depth along the line of sight through the cluster:

$$\tau = \sigma_{\mathrm{T}} \int n_{\mathrm{e}} dl \tag{1.1}$$

where $\sigma_{\mathrm{T}} = 6.65 \cdot 10^{-29}$ m^2 is the Thomson cross section. For a rich cluster of 1 Mpc

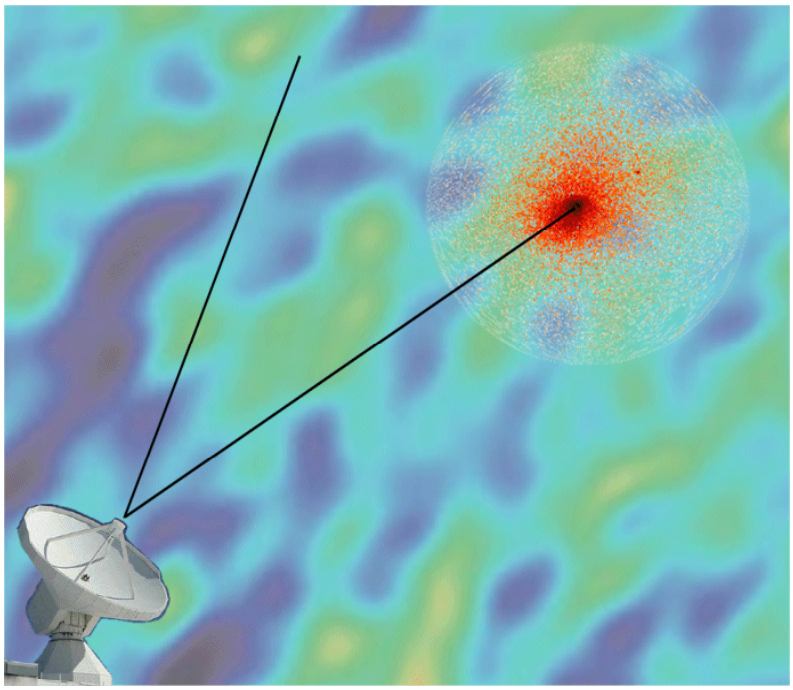

Figure 1.1: The Sunyaev-Zel'dovich effect produces a distortion of the CMB spectrum, measurable by comparing the CMB photons observed through a cluster with the unperturbed photons propagating along a nearby line of sight that avoides the cluster. In background of this figure is the "photo" of the last scattering surface as seen by WMAP (Bennett et al., 2003a). The cluster is a CHANDRA image of RXC J1023.6+0411.

diameter with an electron density $n_{\rm e} = 10^3$ m^{-3}, $\tau \sim 10^{-2}$.
The net result of the thermal SZ effect is an overall heating of the CMB by the IC plasma. This effect can be seen as a temperature difference between the cluster and nearby background (Fig. 1.1). The number of CMB photons is preserved in Thomson scattering, but their average energy is increased by interaction with the energetic electrons (Fig. 1.2). Since the IC medium is optically thin, each photon is scattered only once. In the non-relativistic limit, valid for electron temperatures $T_{\rm e} < 20$ keV, the scattering process simplifies substantially and can be described by the Kompaneets (1956) approximation, which allows a simple solution for the variation of the photon occupation number, $\Delta\eta$:

$$\Delta\eta = xy\frac{e^x}{(e^x-1)^2}\left[x\coth\left(\frac{x}{2}\right)-4\right] \ , \tag{1.2}$$

where x is the dimensionless frequency

$$x = \frac{h\nu}{k_{\rm B}T_{\rm CMB}} = \frac{\nu}{56.8\ {\rm GHz}} \tag{1.3}$$

for a CMB temperature of 2.725 K (Bennett et al., 2003b), and y is a dimensionless measure of the time spent by the photon in the electron distribution,

$$y = \frac{\sigma_{\rm T}k_{\rm B}}{m_{\rm e}c^2}\int n_{\rm e}T_{\rm e}dl \tag{1.4}$$

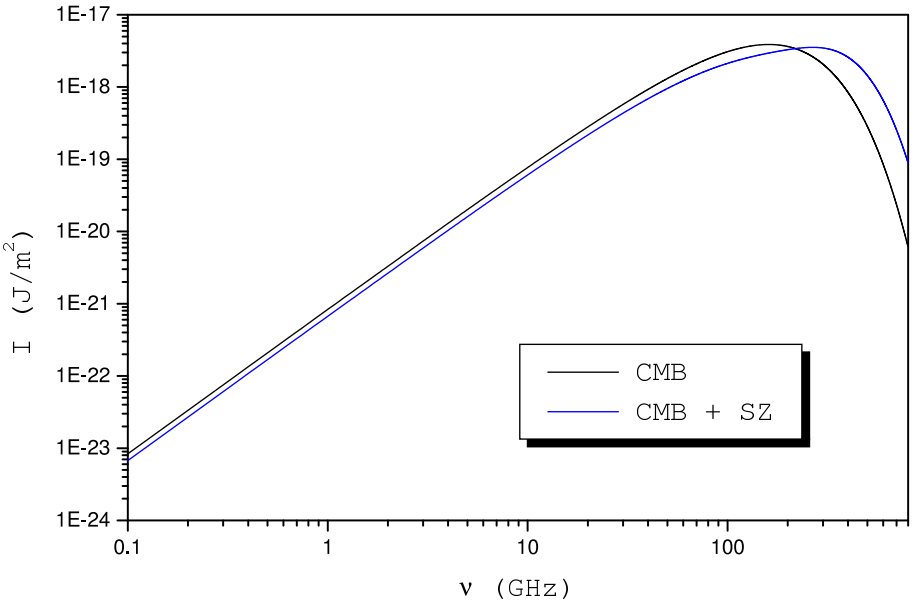

Figure 1.2: The thermal spectrum of the CMB radiation (black) compared with the spectrum resulting after interaction with a 5 keV temperature plasma. The difference has been enhanced by setting a high value of optical depth.

which is usually known as the Comptonization parameter and determines the amplitude of the effect.
The corresponding change in intensity is

$$\Delta I = y f(x) I_0 \tag{1.5}$$

where

$$I_0 = 2\frac{(k_{\rm B}T_{\rm CMB})^3}{(hc)^2} \approx 2.7 \cdot 10^{11}\ {\rm mJy\,sr^{-1}} \tag{1.6}$$

and

$$f(x) = g(x)h(x) \tag{1.7}$$

with the functions $g(x)$ and $h(x)$ defined as follows:

$$g(x) = x\frac{e^x+1}{e^x-1} - 4 \tag{1.8}$$

$$h(x) = x^4\frac{e^x}{(e^x-1)^2}\ . \tag{1.9}$$

The temperature distortion produced by the thermal SZ effect is given by

$$\Delta T = g(x) T_{\rm CMB} y\ . \tag{1.10}$$

Eq. 1.7 describes the spectral shape of the intensity variation. Since the CMB photons gain energy in the scattering process, this corresponds to a decrease in the CMB intensity at lower frequencies and an increase at higher frequencies (Fig. 1.3). The

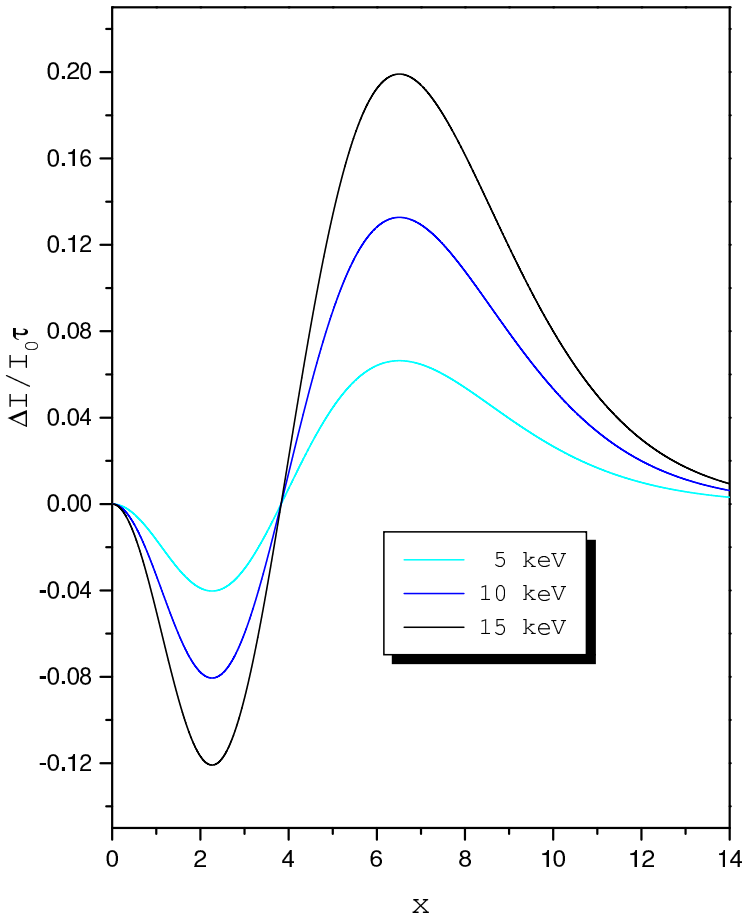

Figure 1.3: Spectral dependence of the thermal intensity change ΔI, in units of $I_0 = 2\frac{(kT_{\rm CMB})^3}{(hc)^2}$, normalized for the cluster optical depth $\tau = \sigma_T \int n_e dl$, as function of the dimensionless frequency $x = \frac{h\nu}{kT_{\rm CMB}}$, for electron temperatures $kT_{\rm e} = 5$ (cyan), 10 (blue), and 15 (black) keV.

function described by Eq. 1.7 has a minimum at a frequency of about 128 GHz, vanishes at 218 GHz and has a maximum at 370 GHz. These values, as well as the spectral shape of the effect, change slightly when the non-relativistic limit approximation is no longer valid. An exact relativistic calculation is described in detail by Rephaeli (1995). The spectral intensity profile can also be alterated if the distribution of electron energies follows a power law instead of a thermal distribution. Such a population might be found in a radio galaxy lobe and would have the effect of enhancing the up-scattered tail of the spectral profile compared to that produced by a thermal electron energy distribution.

1.2 Studying Clusters

The study of clusters through the SZ effect has a number of advantages compared to X-ray observations. First, the SZ effect is redshift independent whereas the X-ray

surface brightness b_x decreases with the third power of the redshift:

$$b_{\rm X}(E) = \frac{1}{4\pi(1+z)^3} \int n_e^2 \Lambda(E, T_e) dl \tag{1.11}$$

where z is the redshift of the cluster and Λ is the spectral emissivity of the gas at the observed X-ray energy E, including both line and continuum processes. The redshift independence of the SZ effectarises from the fact that the CMB temperature and the frequency of the scattered photons evolve with the same reshift dependence. Therefore, the observations of distant clusters are not limited for SZ measurements as they are for X-ray measurements.

The dependence of the surface brightness (Eq.1.11) on the square of the electron density $n_{\rm e}$, has two implications. First, if the IC medium is isothermal but shows density clumping on a scale less than the resolution of the images or along the line of sight, then the X-ray emissivity is enhanced by a factor

$$C_n = \frac{\langle n_{\rm e}^2 \rangle}{\langle n_{\rm e} \rangle^2} \tag{1.12}$$

whilst the value of $\langle n_{\rm e} \rangle$, measured with the SZ effect, remains unchanged.
The second implication affects the possibility of studying the outer region of a cluster. The structure of the cluster atmosphere is often described according to the isothermal beta model (Cavaliere & Fusco-Femiano, 1976), where the parameter beta expresses the square of the ratio between the avarage velocity of the galaxies and that of the gas particles:

$$\beta \equiv \frac{\mu m_{\rm p} \sigma^2}{k_{\rm B} T} = 0.76 \left(\frac{\sigma}{10^3 \, {\rm km/s}} \right)^2 \left(\frac{T}{10^8 \, {\rm K}} \right)^{-1} \tag{1.13}$$

Here $\mu = 0.63$ a.m.u. is the mean molecular weight, $m_{\rm p}$ is the proton mass, T is the temperature of the gas, and σ is the radial galaxy velocity dispersion. The density $\rho(r)$ of the gas at a radius r from the center of the cluster as a function of the density of the number of galaxies $n_{\rm gal}(r)$ at the same distance (we use here ρ instead of the n used previously to avoid confusion with the number density) is described by the relation

$$\left(\frac{\rho(r)}{\rho_0} \right) = \left(\frac{n_{\rm gal}(r)}{n_{0,\rm gal}} \right)^{\beta} \tag{1.14}$$

where ρ_0 and $n_{0,\rm gal}$ are the density of the gas and of the number of galaxies at the center of the cluster.
If the distribution of the galaxies in a cluster is represented by the function (King, 1972):

$$n_{\rm gal} = n_{0,\rm gal} \left[1 + \left(\frac{r}{r_{\rm c}} \right)^2 \right]^{-3/2} \tag{1.15}$$

where $r_{\rm c}$ is the core radius of the cluster, it is possible to describe the distribution of the gas with

$$\rho(r) = \rho_0 \left[1 + \left(\frac{r}{r_{\rm c}} \right)^2 \right]^{-3\beta/2} . \tag{1.16}$$

Eq. 1.16 can be inserted in the appropriate emission expressions and integrated along the line of sight through the cluster to derive the profile of the X-ray surface brightness:

$$I_{\rm X}(r) \propto \left[1 + \left(\frac{r}{r_{\rm c}}\right)^2\right]^{-3\beta+\frac{1}{2}} \tag{1.17}$$

and of the SZ brightness:

$$I_{\rm SZ}(r) \propto \left[1 + \left(\frac{r}{r_{\rm c}}\right)^2\right]^{-\frac{3\beta}{2}+\frac{1}{2}} \tag{1.18}$$

which are shown in Fig. 1.4. This shows that it is more difficult to obtain information on the outer region of the cluster from X-ray maps than from SZ measurement.

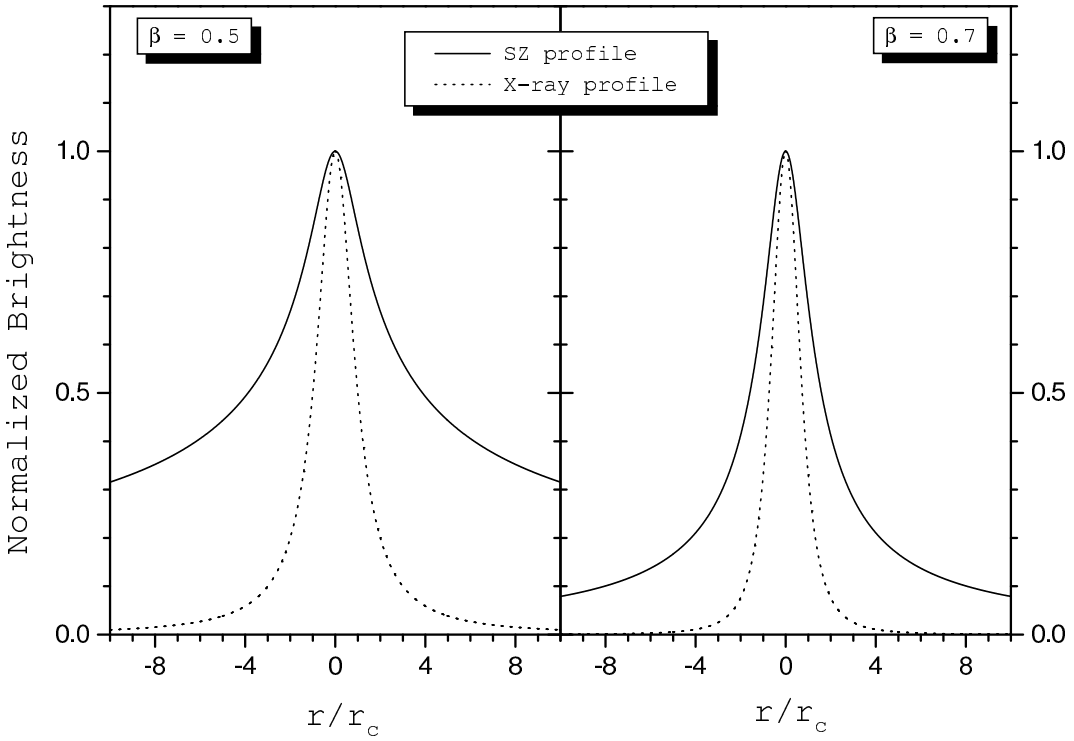

Figure 1.4: The X-ray and SZ profiles of an isothermal sphere of gas. The brighness, normalized to central value, is plotted for $\beta = 0.5$ and $\beta = 0.7$ as function of the angular distance from the center, in units of the angular core radius.

Gravitational lensing of background sources by galaxy clusters provides information complementary to that obtained from SZ effect and X-rays. Using gravitational lensing one can reconstruct the two-dimentional projected mass profile. X-ray observations measure a convolution of the squared electron density with a function of the temperature, integrated on the line of sight. Even when high-resolution spectroscopy allows the determination of the gas temperature, it is not possible to

disentangle the contributions of temperature, electron density and depth in the cluster. The SZ effect is not modified by clumpiness of the gas but, by itself does not allow to separate temperature effects from density variation. Due to the number of degeneracies, a better study of the clusters is provided by a combination of lensing, SZ and X-ray observations. For example, the projected gas density and temperature can be deduced from joint gravitational lensing and SZ data (Doré et al., 2001). The cluster's physical properties can be derived from joint galaxy cluster mapping observations in X-ray and the SZ effect, even without X-ray spectroscopy (Pointecouteau et al., 2002).

1.3 Scientific Motivation

Due to the weakness of the Sunyaev-Zel'dovich effect, the first experimental confirmations came only twenty years after this distortion of the CMB spectrum was theoretically predicted. Since its first measurement, the SZ effect has been used to constrain the value of the Hubble constant H_0 (for example Birkinshaw et al. 1991, Holzapfel et al. 1997, Huges & Birkinshaw 1998, Andreani et al. 1999, Reese et al. 2000), assuming regularity of the distribution and isothermality of the cluster gas. For this purpose, the telescope beam can be matched to the size of the cluster, which maximizes the signal. The X-ray emission and the inverse Compton scattering provide a measure of both $\int n_e^2 dl$ and $\int n_e dl$, and thus permit one to solve for the electron density, n_e, and the depth of the cluster, L. If this depth is assumed to be the same as the tranverse cluster diameter, $D\theta$, where D is the distance to the cluster and θ its angular diameter, we can solve for $D \sim \theta^{-1} L$. If the redshift, z, of the cluster is known, it is possible to estimate $H_0 = zc/D$, or more precisely, in the model of the Robertson-Walker metric it is possible to estimate

$$H_0 = \frac{c}{D q_0^2} \frac{\left[q_0 z + (q_0 - 1)\left(\sqrt{1 + 2q_0 z} - 1\right)\right]}{(1+z)^2} \tag{1.19}$$

if the deceleration parameter, q_0, is known or if one has good enough statistics to derive both parameters from a best fit of the data based on Eq. 1.19.
Although the last generation of baloon and satellite CMB experiments has constrained with high precision the value of the Hubble constant and of the other cosmological parameters, the SZ effect holds its importance for cosmological studies (Carlstrom et al., 2002). Future SZ effect surveys (Planck, APEX) will build a large catalogue of clusters, based on the cluster mass, which is the most appropriate selection criterion for cosmological purposes (Bartlett, 2002). Such catalogs will provide observational constraints on the growth of large-scale structure, and will allow one to study the density and nature of the dark energy (Mohr & Majumdar, 2003; Munshi et al., 2003).

Calculation of the cosmological parameters based on large scale mass distribution depends on accurate derivation of the cluster mass. This derivation is normally based on the assumption of isothermality of the cluster gas. A high-resolution SZ map of RX J1347-1145 (Komatsu et al., 2001) revealed inhomogeneous morphological features that are not well described by a simple regular isothermal β-model. Temperature differences up to a factor of two can also occur in a cluster in the presence of a significant merger.

Since deviations from isothermality inside clusters will not, unlike geometrical effects, be canceled by averaging on large samples a statistical study of the properties and of the structural evolution of galaxy clusters, possible through high-resolution SZ and X-ray maps, is important for cosmology.

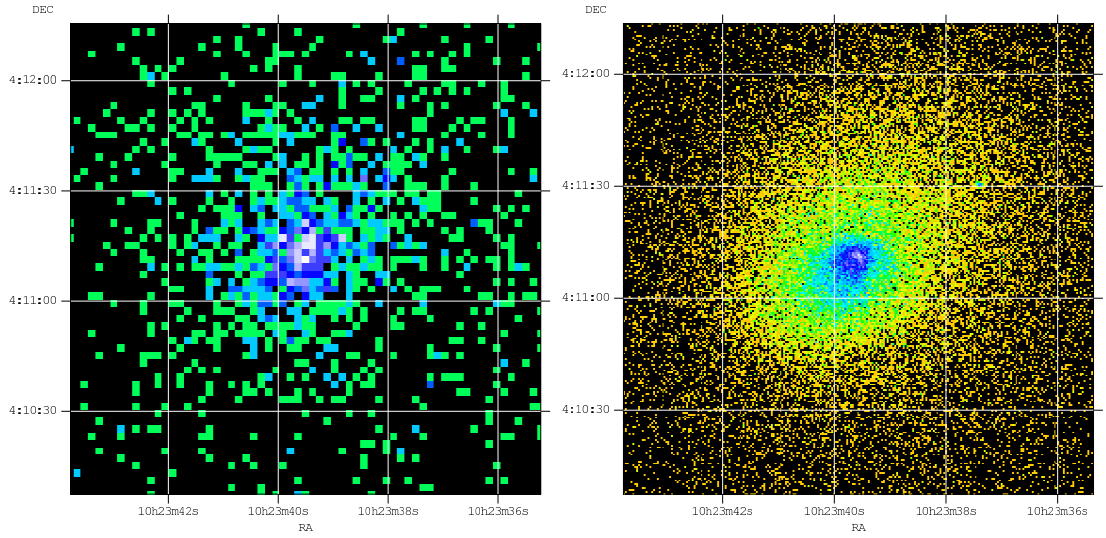

Figure 1.5: X-ray images of the cluster RXC J1023.6+0411 (Zw 3146) seen by ROSAT (left) and CHANDRA (right). Even for a regular cluster, a higher resolution image show decreased spherical symmetry and emerging of features, e.g. the central cD galaxy.

The physics in clusters of galaxies is a subject with several open questions. X-ray observations have revealed that the radiative cooling time of the ICM in the central region of very bright clusters is shorter than the cluster age (Edge et al., 1992). As the pressure support decreases, the gas would infall toward the bottom of the cluster potential well, generating the so-called "cooling flow" (Fabian, 1994). This can be detected as a surface-brightness enhancement in the X-ray emission from a region typically ∼100 to 200 kpc in radius (e.g. Edge et al. 1994; Tamura et al. 2001). Most of the cooled gas or its product have not been found (see for example Kaastra et al. 2001). Peterson et al. (2001) suggested a cooling process more complicated than simple isobaric radiative cooling or differential cold absorption of the gas as a possible explanation. McCarthy et al. (2002) suggested that a contribution from a non-thermal source to the total X-ray emission would significantly reduce the thermal contribution to the X-ray flux and hence reduce the calculated cooling rate. Without entering into this debate, we note that high-resolution SZ maps could provide an independent measure of the cluster temperature profile and possibly contribute to a better understanding of the physical processes occurring in the cluster atmosphere.

High-resolution SZ maps could be exploited to test models on dark-matter-driven structure formation. CMB experiments have proven that most of the matter in the Universe is in form of dark and non-baryonic matter. Since dark matter interacts with baryons and photons only through gravitation, its fluctuations can grow already be fore

the epoch of recombination and create the potential wells into which the baryons will later fall. Kochfar (2003) has built a semi-analytical model to simulate the formation of elliptical galaxies starting from the evolution of the dark matter component through the cooling of gas, the star formation and the merging of galaxies. Using the scale invariance of dark matter clustering, it would be possible to use this model to calculate the fraction of clusters, within a defined mass range and at a certain redshift, that should be undergoing a major merger (Burkert, 2003). If this number is relatively large, it could be compared to the number of mergers identified in a sample of high-resolution SZ maps of clusters.
Thus, studies on cluster physics and cosmology are most powerful when using a combination of high-resolution SZ an X-ray observations.

1.4 Millimeter Observations of the SZ effect

The observation of the SZ effect is easiest at the wavelengths at which the signal is greatest, at 2.3 mm for the decrement and 800 μm for the increment. Although the absolute value of the effect is higher at the positive maximum and at this wavelength a higher resolution can be achieved for the same telescope, the observation of the decrement might be easier in ground based experiments for a number of reasons. First, the atmospheric window at 2 mm is wider than at 800 μm (Fig. 1.6) allowing observations with a broader bandwidth, and the atmospheric opacity is lower and more stable and so the production of maps, for which a long integration time is required, is less affected by background fluctuations.

Second, source confusion is less in the 2 mm window. Confusion limits to measurements of the thermal SZ effect have been discussed by Fischer & Lange (1993), based on the extrapolation of available data on radio source counts, IR source counts, and the spatial distribution of Galactic cirrus. Thermal dust emission from the cluster is found to be negligible. Estimates of the Galactic free-free emission based on Hα emission indicate a contribution at a level somewhat below that of extragalactic radio sources. The results are presented in Fig. 1.7 for a single reference beam subtraction experiment with a 2' beam size and 4' throw. The 1 σ confusion limit in the band around the SZ decrement is six times lower than in the band of the increment.

Confusion may come also from gravitationally lensed images of distant dusty star-forming galaxies in the background of the cluster. This contribution becomes more important at frequencies higher than 200 GHz and for telescopes with smaller beams (Blain, 1998).

From the sensitivity discussion above, observations of the SZ effect carried out in the 2 mm band present some advantages. The resolution in the 2 mm band of an instrument installed at the IRAM 30 m telescope at Pico Veleta would be comparable to that of the X-ray satellite XMM, allowing a powerful combined analysis of clusters.

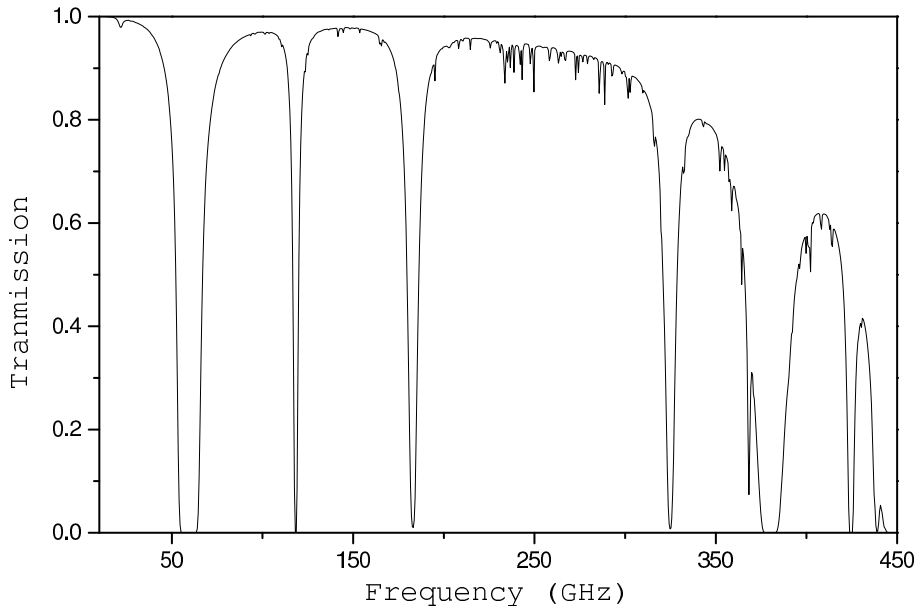

Figure 1.6: Simulation of the transmission of the atmosphere, for a precipitable water vapor content of 2 mm, as function of the wavelength.

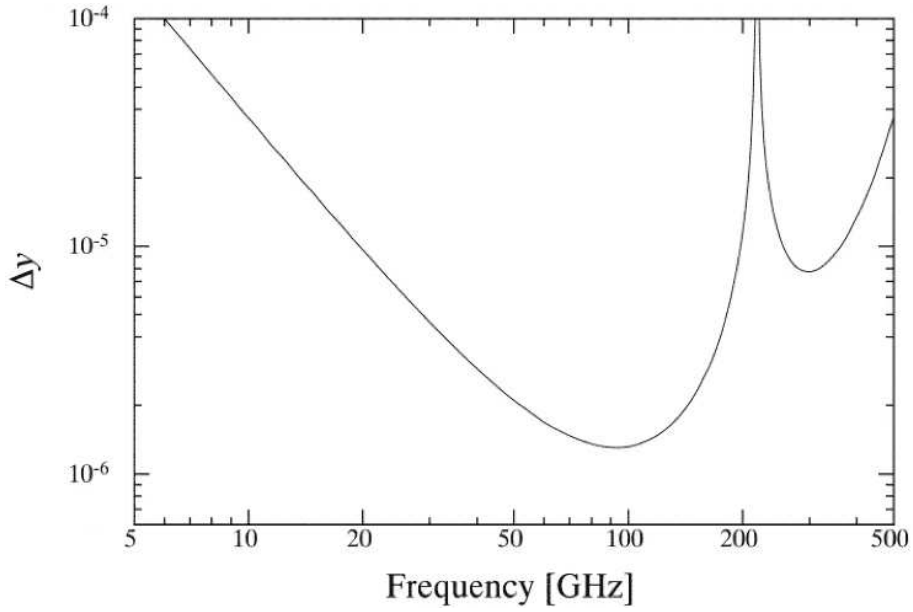

Figure 1.7: Estimated 1 σ confusion limit to the measurement of the thermal SZ effect in units of the Comptonization parameter, Δy, assuming an optical depth through the cluster $\tau = 0.01$. The curve represents the confusion expected from the quadrature sum of the contributions from radio galaxies, IR galaxies, and IRAS cirrus. At 218 GHz the confusion limit diverges because the thermal SZ effect vanishes at this frequency. From Fischer & Lange (1993).

Chapter 2

Bolometers

2.1 Thermal Detectors

Bolometers are the most sensitive detectors for broad-band electromagnetic radiation at wavelengths between 250 μm and 3 mm. They are thermal detectors, i.e. photons are absorbed and produce a variation in a thermometric quantity that can be measured. To detect small signals, the thermal energy kT available in the detector must be small compared to the energy of the photons $h\nu$. To give a qualitative idea of the order of magnitude, if we require

$$kT = h\nu/100 \tag{2.1}$$

then for millimetric wavelengths one must cool the detectors to temperatures of 300 mK or lower.

2.2 Principles of Bolometer Operation

For a detailed discussion of bolometric theory and for an exhaustive review see for example Clark Jones (1953) and Richards (1994) and references therein.
In a simple model, the radiation incident on the detector is converted into heat, is distributed in the bolometer which has a heat capacity C, and flows to a thermal bath at constant temperature T_0 through a weak link of average thermal conductivity G. In bolometers the temperatura-sensitive element is a resistor, whose value can be measured by biasing it and reading the voltage drop across its ends:

$$\frac{dV}{dT} = \alpha I_{\rm bias} R \tag{2.2}$$

$$\alpha = \frac{1}{R}\frac{dR}{dT} \tag{2.3}$$

The detector is heated also by the electrical power necessary for the resistance measurement. The steady state is reached when the sum of the radiation power, Q, flowing into the absorber and the electrical power, P, dissipated in the thermistor is equal to the power flowing out of the detector into the thermal bath:

$$Q + P = G(T - T_0) \tag{2.4}$$

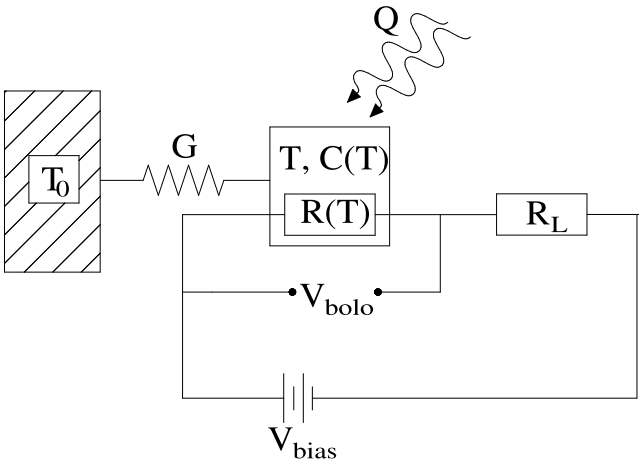

Figure 2.1: Schematic of the electrical and thermal circuit of a bolometer. The bolometer, which has a heat capacity C and resistance R, is connected to a thermal bath at constant temperature T_0 through a weak link of average thermal conductance G. The optical power, Q, is absorbed and converted into head, causing the temperature, and thus the resistance of the bolometer, to change. The bolometer is inserted in a bias circuit and its resistance is measured by reading the voltage drop across its ends.

A change in the radiative power ΔQ will cause the temperature to rise by ΔT and consequently will cause the bolometer resistance, R_0, to change by $\frac{dR}{dT}\Delta T$. Disregarding terms of order higher than the first, the thermal balance equation becomes

$$Q + \Delta Q + I_{\rm bias}^2 \left(R_0 + \frac{dR}{dT}\Delta T \right) = G(T - T_0) + G_{\rm d}\Delta T + C\frac{d\Delta T}{dt} \tag{2.5}$$

where

$$G_{\rm d} = G_0 + \frac{dG}{dT}(T - T_0) \tag{2.6}$$

is the dynamic thermal conductance. Subtracting the steady term Eq. 2.4 from Equation 2.5:

$$\Delta Q + I_{\rm bias}^2 \alpha R_{\rm bol}\Delta T = C\frac{d\Delta T}{dt} + G_{\rm d}\Delta T \tag{2.7}$$

Introducing the effective thermal conductance, $G_{\rm eff}$, and the effective time constant, $\tau_{\rm e}$, defined as:

$$G_{\rm eff} = G - {I_{\rm bias}}^2 \alpha R \tag{2.8}$$

$$\tau_{\rm e} = \frac{C}{G_{\rm eff}} \tag{2.9}$$

then

$$\frac{\Delta Q}{G_{\rm eff}} = \tau_{\rm e}\frac{d\Delta T}{dt} + \Delta T \tag{2.10}$$

Note that we assumed that the bolometer resistance depends only on temperature. This is true in general, but it might not be correct in the presence of a large potential drop that produces a strong electric field (Grannan et al., 1992).

If the radiation power has a step-like shape of amplitude ΔQ, the solution for equation 2.10 is

$$\Delta T = \frac{\Delta Q}{G_{\text{eff}}} \left(1 - e^{-\frac{t}{\tau_e}}\right) \tag{2.11}$$

From this relation one sees that for a given ΔQ, in order to produce a large ΔT, one wants a small G_{eff} and so the bolometer should have a weak thermal connection to the heat sink.
Looking at Equations 2.8 and 2.9 it worth noting that when $\alpha < 0$ (i.e. for semiconductors), the bolometer exchanges heat with the thermal bath with a $G_{\text{eff}} > G_{\text{d}}$. This effect is called electro-thermal feedback (ETF): when the optical power increases, the resistance decreases, thus reducing the electrical power dissipated and allowing a better cooling through a better contact with the thermal bath. Through this mechanism, the effective time constant becomes shorter than the thermal one:

$$\tau_{\text{e}} = \frac{C}{G_{\text{eff}}} < \frac{C}{G} = \tau \ . \tag{2.12}$$

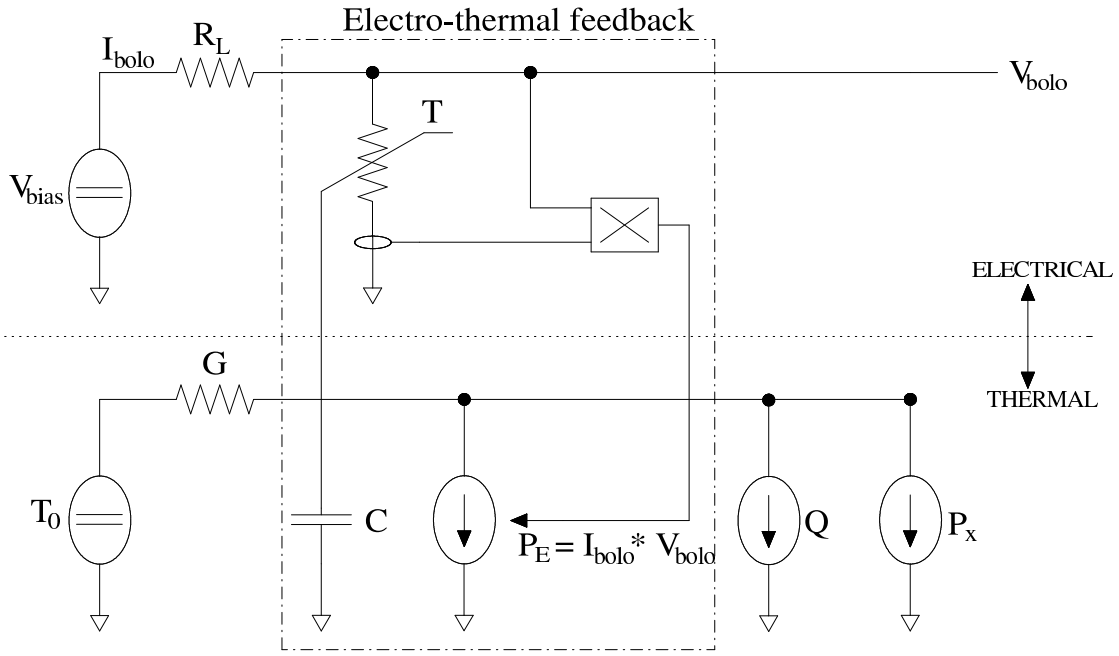

Figure 2.2: The electrical and thermal circuits of a bolometer with emphasis on the electro-thermal feedback mechanism: the value of the resistance R depends on the equilibrium temperature in the thermal circuit, which depends on the dissipated electrical power, function of the resistance R itself. In a real situation, besides the electrical and the radiative power P_{E} and Q, one has to include the stray power P_{x}, due for example to microphonic heating.

Often the radiative signal is modulated at a frequency ω:

$$\mathbf{\Delta Q} = \Delta Q e^{i\omega t} \tag{2.13}$$

Looking for solutions of the form

$$\mathbf{\Delta T} = \Delta T e^{(i\omega t - \theta)} \tag{2.14}$$

one obtains

$$\begin{aligned} \frac{\Delta T}{\Delta Q} &= \frac{e^{i\theta}}{i\omega C + G_{\text{eff}}} \\ \left|\frac{\Delta T}{\Delta Q}\right| &= \frac{1}{G_{\text{eff}}\sqrt{1+\omega^2\tau_{\text{e}}^2}} \end{aligned} \tag{2.15}$$

Combining Equation 2.3 and Equation 2.15, it is possible to find the voltage responsivity $\Re$ of the bolometer, i.e. the change in voltage caused by a known signal ΔQ:

$$\Re(\omega) = \left|\frac{dV}{dQ}\right| = \left|\frac{dV}{dT}\right|\left|\frac{dT}{dQ}\right| = \frac{\alpha I_{\text{bias}} R}{G_{\text{eff}}} \tag{2.16}$$

Where we assumed the bolometer is biased by a perfect current source. In general this is obtained by applying a voltage, V_{bias}, across the series-connected bolometer and load resistor of resistance R_{L} (Fig. 2.1), causing a bias current, I_{bias}, to flow, given by:

$$I_{\text{bias}} = \frac{V_{\text{bias}}}{R + R_{\text{L}}}\,. \tag{2.17}$$

Eq. 2.16 for the responsivity can be generalized for an imperfect current source by substituting

$$R \to \frac{R_{\text{L}} R}{R_{\text{L}} + R}\,. \tag{2.18}$$

This reduces to the previous result (Eq. 2.16) when $R_{\text{L}} \gg R$ as is usually the case.
To optimize the performance of the detector one can measure the bolometer responsivity, $\Re$, by observing a blackbody at a defined temperature if the thoughput $A\Omega$ of the system is known. The throughput can be measured easily, however, it is difficult to build a standard source of calibration at these wavelengths. Instead, one can measure a quantity proportional to the optical responsivity, the electrical responsivity, $\Re_{\text{e}}$, which is related to the optical responsivity by the optical efficiency, η.

$$\Re_{\text{e}} = \frac{\Re_{\text{opt}}}{\eta}\,. \tag{2.19}$$

To calculate the electrical responsivity we define the parameter $\mathcal{H}$:

$$\mathcal{H} = \frac{d\log P}{d\log R} = \frac{RdP}{PdR} \tag{2.20}$$

When the power on the bolometer is purely electrical

$$\mathcal{H} = \frac{V/Id(VI)}{VId(V/I)} = \frac{Z+R}{Z-R} \tag{2.21}$$

where

$$Z = \frac{dV}{dI} \tag{2.22}$$

is the dynamic resistance. When we add an optical power Q, $\frac{dV}{dI} = -R_{\rm L}$. Recalling that $\Re_{\rm e}(0) = \frac{dV}{dQ}$, the parameter $\mathcal{H}$ becomes

$$\mathcal{H} = \frac{-\frac{R}{R_{\rm L}} + 1 + \frac{1}{I}\frac{1}{R_{\rm e}(0)}}{1 + \frac{R}{R_{\rm L}}} \; . \tag{2.23}$$

By comparing Equations 2.21 and 2.23 one finds the Jones formula (Clark Jones, 1953)

$$\Re_{\rm e}(0) = \frac{R_{\rm L}}{2IR}\frac{Z - R}{Z + R_{\rm L}} \; . \tag{2.24}$$

The load curve is defined as the relation between the steady voltage V across the bolometer and the steady current I through the bolometer. Since

$$I = \frac{V_{\rm bias} - V}{R_{\rm L}} \; , \tag{2.25}$$

it is possible to build the load curve by measuring the bolometer voltage, V, as function of the bias voltage,$V_{\rm bias}$. From the load curve one can calculate the dynamic resistance Eq. 2.22 and the bolometer resistance $R = \frac{V}{I}$. Equation 2.24 shows that is possible to measure the bolometer responsivity from a load curve, i.e. by purely electrical means.

2.3 Noise

Bolometer sensitivity is often described in terms of the Noise Equivalent Power (NEP). The NEP is the change in incident power required to generate a signal with signal to noise ratio of unity. Sources of noise in bolometric detectors have been discussed in details in Mather (1984a), Mather (1984b), Lamarre (1986) and Benford et al. (1998), and can be devided into frequency-dependent sources and frequency-independent sources. The voltage noise at a certain frequency, $V_n(\omega)$, is the quadrature sum of of all the noise sources, $V_i(\omega)$

$$V_n^2(\omega) = \sum_i V_i^2(\omega) \; . \tag{2.26}$$

The NEP is related to the voltage noise (Eq. 2.26) by the bolometer responsivity (Eq. 2.16)

$$\mathrm{NEP}^2(\omega) = \frac{V_n^2(\omega)}{\Re^2(\omega)} \; . \tag{2.27}$$

2.3.1 Johnson Noise

Spontaneous fluctuation of electrical charge in a material of resistivity R can be described by the same equations of Brownian motion, the charge, the current and the resistivity playing the role of position, velocity and viscosity. The resulting spectrum is:

$$V_{\mathrm{J}}^2(\omega) = 4kTR\,. \tag{2.28}$$

This relation was first experimentally verified by Johnson (Johnson, 1928) and theoretically interpreted by Nyquist (1928).
The corresponding NEP is

$$\mathrm{NEP}_{\mathrm{J}} = \frac{\sqrt{4kTR}}{\Re(\omega)} \tag{2.29}$$

For a given resistance, the only way to reduce the Johnson noise is to cool the detector, and so bolometers are cooled to very low temperature.

2.3.2 Phonon Noise

Since thermal energy is quantized in phonons, even at equilibrium the thermal energy of a bolometer will fluctuate. From statistical physics (see for example Kittel 1958) we know that for a system in thermal contact with a heat reservoir,

$$\langle E\rangle = \frac{\sum_i E_i e^{-\frac{E_i}{kT}}}{\sum_i e^{-\frac{E_i}{kT_0}}}\,, \tag{2.30}$$

$$\langle E^2\rangle = \frac{\sum_i E_i^2 e^{-\frac{E_i}{kT}}}{\sum_i e^{-\frac{E_i}{kT_0}}}\,. \tag{2.31}$$

Defining the partition function, Z, to be

$$Z = \sum_i e^{-\frac{E_i}{kT}} \tag{2.32}$$

and defining the variable $\beta = -1/kT$, one finds the following relations:

$$\langle E^2\rangle = \frac{1}{Z}\frac{\partial^2 Z}{\partial\beta^2}\,, \tag{2.33}$$

$$\langle E\rangle = \frac{1}{Z}\frac{\partial Z}{\partial\beta}\,, \tag{2.34}$$

$$\frac{\partial\langle E\rangle}{\partial\beta} = \frac{1}{Z}\frac{\partial^2 Z}{\partial\beta^2} - \frac{1}{Z}\frac{\partial Z}{\partial\beta} = \langle E^2\rangle - \langle E\rangle^2 = \langle\Delta E^2\rangle\,. \tag{2.35}$$

The heat capacity is defined as

$$C = \frac{\partial\langle E\rangle}{\partial T} = \frac{\partial\langle E\rangle}{\partial\beta}\frac{\partial\beta}{\partial T} = \frac{\partial\langle E\rangle}{\partial\beta}\frac{1}{kT^2} \tag{2.36}$$

therefore

$$\langle \Delta E^2 \rangle = kT^2 C \ . \tag{2.37}$$

The bolometer will read temperature fluctuations with an RMS value of:

$$\langle \Delta T^2 \rangle = \frac{\langle \Delta E^2 \rangle}{C^2} = \frac{kT^2}{C} = \int_0^\infty W_T(\omega) d\omega \tag{2.38}$$

where $W_T(\omega)$is the power spectrum of the temperature fluctuations and T is the temperature of the heat reservoir.
The temperature fluctuations ΔT correspond to a random power $H(t)$ applied to the device which we will assume to have a white spectrum. The equation that relates $H(t)$ to ΔT is

$$C\frac{d\Delta T(t)}{dt} + G\Delta T(t) = H(t) \ . \tag{2.39}$$

Taking the Fourier transform of $\Delta T(t)$ and $H(t)$ and substituting in Equation 2.39 one finds the relation between the power spectra W_T and W_H:

$$W_T(\omega) = \frac{W_H}{(2\pi\omega C)^2 + G^2} \ . \tag{2.40}$$

Using Eq. 2.38, one can derive the spectrum of the power fluctuations

$$W_H(\omega) = 4kT^2 G \ . \tag{2.41}$$

The corresponding NEP is

$$\mathrm{NEP}_{\mathrm{phon}} = \frac{\sqrt{4kT^2 G}}{\eta} \tag{2.42}$$

where we introduced the optical efficiency, η, to refer the NEP to an effective power at the input. For a given time constant, τ, the thermal conductance $G = C/\tau$ scales with either T or T^3 depending whether the heat capacity is dominated by metallic or crystal components. The NEP will then be proportional to $T^{3/2}$ or to $T^{5/2}$. Once more, the only way to reduce these fluctuations is to cool down the system.

2.3.3 Photon Noise

The RMS value of the fluctuations of the occupation number of a single eigenstate for a gas of bosons in equilibrium is (Kittel, 1969)

$$\langle \Delta n^2 \rangle = \langle n \rangle \left(1 + \langle n \rangle\right) \ , \tag{2.43}$$

where

$$n(\nu) = \frac{1}{e^{\frac{h\nu}{kT}} - 1} \ . \tag{2.44}$$

The corresponding fluctuations of the power are

$$\begin{aligned} \langle (\Delta P)^2 \rangle &= \int_{\Delta\nu} (h\nu)^2 \langle \Delta n^2 \rangle d\nu \\ &= \int_{\Delta\nu} (h\nu)^2 \cdot \left[\frac{1}{e^{\frac{h\nu}{kT}} - 1} + \left(\frac{1}{e^{\frac{h\nu}{kT}} - 1} \right)^2 \right] \cdot d\nu \ . \end{aligned} \tag{2.45}$$

If the detector has throughput $A\Omega$, the number of modes, N, that can be detected is

$$N = 2A\Omega\frac{\nu^2}{c^2} \tag{2.46}$$

and the corresponding NEP is

$$\mathrm{NEP}^2_{\mathrm{phot}} = \int_{\Delta\nu} 2A\Omega\frac{\nu^2}{c^2}(h\nu)^2 \cdot \left[\frac{1}{e^{\frac{h\nu}{kT}}-1} + \left(\frac{1}{e^{\frac{h\nu}{kT}}-1}\right)^2\right] \cdot d\nu \ . \tag{2.47}$$

This source of noise is unavoidable and the only way to reduce it is a proper selection of the frequency band, $\Delta\nu$, by means of filters. For ground-based experiments the fluctuation of the photon background is the dominant source of noise.

2.3.4 $1/f$ Noise

Most bolometers have excess electrical noise, especially at low frequency, which is usually called "$1/f$ noise". The frequency below which the noise starts diverging from a white spectrum is called the "$1/f$ knee". Typical sources of this kind of noise are bad electrical contacts and impurities, and a distribution of time constants, due for example to an oxidized surface on semiconductors. It can be shown (Van der Ziel, 1970) that the resulting spectrum is proportional to the square of the bias current and to the inverse of the frequency:

$$W_i(f) \propto \frac{\alpha I^2}{fN_0} \ . \tag{2.48}$$

Temperature fluctuations of the thermal bath, with noise spectrum W_T, constitute another source of noise at low frequency, with NEP given by:

$$\mathrm{NEP}^2_{\mathrm{T}} = \frac{G^2 W_T(\omega)}{\eta^2} \ . \tag{2.49}$$

Amplifier noise is typically a combination of white noise and sources with a $1/f$ spectrum, e.g. a long term drift.

2.3.5 Microphonics

The term microphonics generally refers to all the noise signals generated by mechanical vibrations.
The dissipation of vibrational energy may cause a drift in the system temperature or variations in the detector temperature, often due to the piezoelectric effect at the level of the soldering of wires on the thermistor or on the absorber; this gives rise to a spurious signal and then increases the noise at low frequency.
The modulation by mechanical motion of stray capacitances to ground induces a voltage level (Bhatia et al., 1999):

$$V = i\omega a C V_0 \left(\frac{R}{1+i\omega CR}\right) \tag{2.50}$$

with a=fraction of capacitance which is modulated, C=capacitance; V_0=steady-state voltage, and R=resistance of wiring.
Vibrations may also modulate the capacitive coupling between the electrical wires or induce parasitic currents if the wires are moving in a magnetic field, for example the field generated by cooler motors and drive electronics or the residual field following adiabatic demagnetization cooling.

2.4 Noise - Non Equilibrium Theory

The results derived in the previous section are valid under the assumption that the system is isothermal and in equilibrium. This is not strictly true, as there is a temperature gradient in the thermal link and the electrothermal feedback simulates a better thermal contact to the bath and reduces the time constant of the bolometer. A more correct derivation leads to the following results for the Johnson and the phonon noise (Mather, 1982):

$$\mathrm{NEP}_{\mathrm{J}}^2 = 4kTP\left(\frac{Z+R}{Z-R}\right)^2\left(1+\omega^2\tau^2\right) \tag{2.51}$$

$$\mathrm{NEP}_{\mathrm{phon}}^2 = \frac{4kGT^2}{\eta}\frac{\int_{T_0}^{T}\left[\frac{tk(t)}{Tk(T)}\right]^2 dt}{\int_{T_0}^{T}\frac{k(t)}{k(T)}dt} \tag{2.52}$$

where τ is the physical time constant and $k = k(T)$ is the thermal conductivity of the link. According to these equations, the consequent reduction of noise with respect to results 2.29 and 2.42 can be as much as 60 % for the Johnson noise and 30 % for the phonon noise.

2.5 Bolometer Optimization

Equation 2.16 shows that responsivity can be improved by the proper choice of the parameters α, I_{bias}, R, and G_{eff}. The thermistor is chosen with the highest possible α, since this is the only parameter that is independent from other considerations. I_{bias} and R cannot be increased without affecting the noise (see Equations 2.48 and 2.28); G must be chosen depending on the estimated optical power, to avoid overloading the detector. Furthermore, G can be reduced only if the heat capacity, C, is reduced at the same time, or the improvement will cost a slower detector.
If we minimize the phonon noise (Eq. 2.42) with respect to the difference, ΔT, between the temperatures of the bolometer, T, and of the reference bath, T_0, then one requires

$$\frac{d\mathrm{NEP}_{\mathrm{phon}}}{d\Delta T} = 0\ . \tag{2.53}$$

For a given loading, P, and using $G = P/\Delta T$, we find for an optimum bolometer that

$$\Delta T = T_0\ \text{, and} \tag{2.54}$$

$$G = P/T_0 \ . \tag{2.55}$$

Substituting the Equations 2.54 and 2.55 in Equation 2.29 we find:

$$\begin{aligned} \mathrm{NEP_J} &= \frac{\sqrt{8kT_0R}}{\sqrt{(\alpha IR)^2}/(G-\alpha I^2)} \\ &= \frac{\sqrt{8kT_0R}}{\sqrt{\alpha^2 P_e R}/(G-\alpha P_e)} \\ &= \left(\frac{P_e+P_o}{\alpha T_0} - P_e\right)\sqrt{\frac{8kT_0}{P_e}} \ , \end{aligned} \tag{2.56}$$

where we called P_o and P_e respectively the optical and the electrical power, we used Equation 2.8, and we neglected the frequency-dependent term in the responsivity. Equation 2.56 can be used to calculate the electrical bias for which the Johnson noise is minimized:

$$P_e = \frac{P_o}{1-\alpha T_0} \ . \tag{2.57}$$

Since the parameters with respect to which the noise expression has to be minimized are not independent, a more correct way to optimize the detectors is the numerical solution of the entire set of equations at the same time (Mather, 1984a; Griffin & Holland, 1988; Grannan et al., 1997). Furthermore, at very low temperatures, e.g. below 100 mK, some of the assumptions that we used in the treatment of the bolometer theory are not appropriate, for example, the Kapitza thermal resistances will give a large contribution to the thermal conductance, G. For this reason, the only way to optimize the detectors at these temperatures is empirical.

2.6 Bolometer Construction

The functions of radiation absorption and temperature measurement are carried out by the same element in monolithic bolometers (Downey et al., 1984) or by two different components in composite bolometers (Coron et al., 1971). The latter design has the advantage of allowing the optimization of the functions independently.
Since 1961 (Low, 1961), the most widely used thermistor is doped germanium, which reached the peak of its evolution with the neutron transmutation doping (NTD) techniques (Haller et al., 1984), in which an ultrapure Germanium sample is exposed to thermal neutrons generated in a nuclear reactor. Compared to the traditional doping techniques, the NTD process (Table 2.1) generates an excellent homogeneity of the doping concentration and compensation. This allows the production of closely matched chips, suitable for the construction of bolometer arrays. Furthermore, homogeneity and implanted electrical contacts result in an excellent performance of the chips at low frequency.

The relationship between resistance and temperature in doped Germanium can be represented by an analytic expression over a wide range of temperatures. For the

Isotope	Abundance (%)	Neutron Capture and Decay Reactions	Dopant Type
$^{70}_{32}$Ge	20.5	$^{70}_{32}\mathrm{Ge}(n,\gamma)^{71}_{32}\mathrm{Ge} \xrightarrow[11.8d]{EC} {}^{71}_{31}\mathrm{Ga}$	p
$^{72}_{32}$Ge	27.4	$^{72}_{32}\mathrm{Ge}(n,\gamma)^{73}_{32}\mathrm{Ge}$	
$^{73}_{32}$Ge	7.8	$^{73}_{32}\mathrm{Ge}(n,\gamma)^{74}_{32}\mathrm{Ge}$	
$^{74}_{32}$Ge	36.5	$^{74}_{32}\mathrm{Ge}(n,\gamma)^{75}_{32}\mathrm{Ge} \xrightarrow[82.8m]{\beta^-} {}^{75}_{33}\mathrm{As}$	n
$^{76}_{32}$Ge	7.8	$^{76}_{32}\mathrm{Ge}(n,\gamma)^{77}_{32}\mathrm{Ge} \xrightarrow[11.3h]{\beta^-} {}^{77}_{33}\mathrm{As} \xrightarrow[38.8h]{\beta^-} {}^{77}_{34}\mathrm{Se}$	n

Table 2.1: Scheme of the NTD process. From Haller et al. (1984).

temperature and doping values generally employed this relation is (Mott, 1969):

$$R(T) = R_0 e^{\sqrt{\frac{\Delta}{T}}} \tag{2.58}$$

where the parameter Δ depends on the doping concentration and R_0 depends on the doping concentration and on the thermistor dimensions. By controlling the doping process it is then possible to realize chips with the desired resistance at the expected working temperature (Fig. 2.3).

The most common way to build an infrared (IR) absorber is by metallic deposition on a dielectric substrate, the substrate usually being chosen among materials with a high Debye temperature to keep the heat capacity small. In the last years, silicon nitride membranes have found wide use due to their excellent thermal and mechanical properties and because they can be processed using photolithographic techniques, which allow easy production of bolometric arrays.

The optical properties of the absorber may be optimized for the specific purpose by varying the thickness of the metallic film depending on the thickness and refractive index, n, of the substrate (Carli & Iorio Fili, 1981; Mónzon & Sánchez-Soto, 1994). Monochromatic absorption with 100 % efficiency has been achieved, and frequency-independent absorption with 50 % efficiency has been demonstrated for any value of n. It is also possible (Kreysa et al., 2001) to use a quarter wave reflector to couple the electro-magnetic field directly onto a metal film deposited on the silicon nitride. This method provides almost maximum efficiency for monochromatic absorption, and greatly simplifies the bolometer construction.

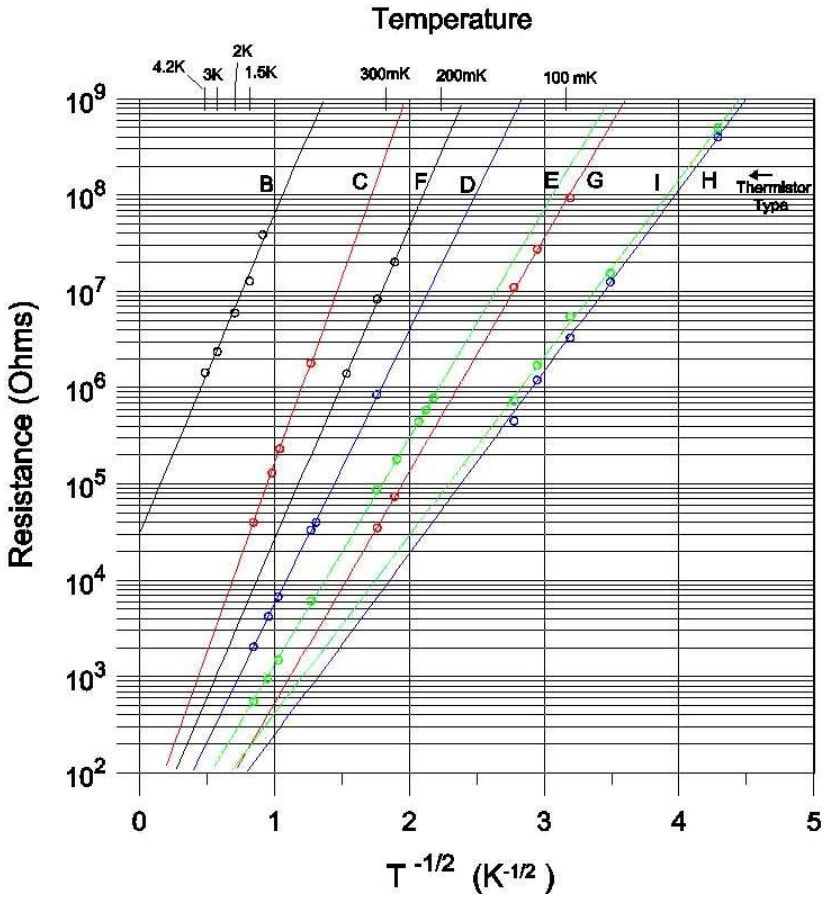

Figure 2.3: Resistance vs. temperature$^{-1/2}$ for NTD Germanium samples of size $250 \times 250 \times 250$ μm. From Haller & Beeman Assoc. Inc..

2.7 Read-Out Electronics

The low intrinsic noise of bolometers demands electronic amplifiers with low noise and good stability. Designing the amplifier (Hristov, 2001) and chosing the bias strategy (Raccanelli, 1999) becomes a challenging part of a successful experiment.
Since the typical resistance of a bolometer is of the order of one to a few MΩ, it is necessary to lower the impedance of the circuit for the signal to be amplified and to prevent microphonics and RF pick up. This can be done by means of a JFET stage configured as a "source follower" (see for example Horowitz & Hill 1989). The source

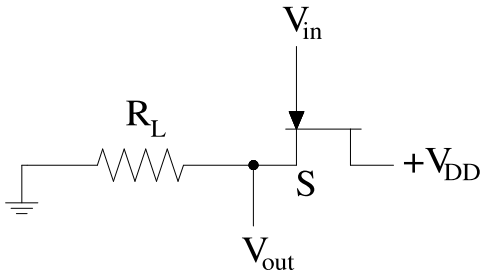

Figure 2.4: The simplest source follower.

follower leaves the voltage signal unchanged but amplifies the current, thus allowing the reduction in the impedance.
To reduce microphonics, the JFETs stage must be placed as close as possible to the detectors. On the other hand, JFETs require a temperature of at least $\sim$ 90 K to operate and have minimal noise between 100 K and 130 K. Thus, when choosing the JFETs one has to take into account the desired noise level and also the maximum power tolerable by the cryogenics.

2.8 Coupling of Infrared and Millimeter Waves to Bolometers

Bolometers are sensitive to radiation at all wavelengths and can also be used to detect energetic particles. The desired frequency band is usually determined by a series of optical filters placed in front of the detector. Since the in-band radiation power passed by the filters for millimeter-wave bolometers is typically several orders of magnitude smaller than the infrared radiation power at the input of the filters, particular care must be taken to avoid high-frequency leaks that could compromise the in-band sensitivity. The radiation is generally coupled to the detectors by means of light concentrators which also define the acceptance angle, Ω. For multi-mode detection, the Winston cones (Winston, 1970) of parabolic shape are used. For diffraction-limited detection, conical lightpipes act as single mode antennas. Although corrugated horns have significantly reduced sidelobe levels (Padman & Murphy, 1991), straight cones are often used because they are easier to machine.

2.9 Calibration of a Bolometric Receiver

There are different ways to calibrate bolometers, depending on the purpose and the required accuracy. Thus, calibration to optimize the receiver is different from calibration on the sky with the aim of including the whole optical system for astronomical observations.

Basic calibration

By chopping a source, i.e. by alternately observing two black bodies at different temperatures, it is possible to measure the responsivity. The accuracy that can be reached with this method is limited by the uncertainity with which the temperature of the sources is known. Also, since responsivity is a function of bolometer temperature, chopping a large temperature difference can lead to a calibration error.

Intermediate calibration

An intermediate calibration can be obtained from the load curves (see section 2.2). One takes two load curves under different backgrounds and plots them on the same graph (see Fig. 2.5); a straight line starting from the origin of the axes represents a line of constant resistance and therefore of equal temperature. By taking the difference between the electrical power at the two intersections of the straight line with the load curves, one can evaluate the difference in the optical power reaching the detector:

$$\Delta(Q) = (IV)_2 - (IV)_1 \tag{2.59}$$

The sensitivity can then be derived by dividing the value of the responsivity (Eq. 2.24) measured with the load curve by the ratio between the power (Eq. 2.59) and the difference between the two temperatures.

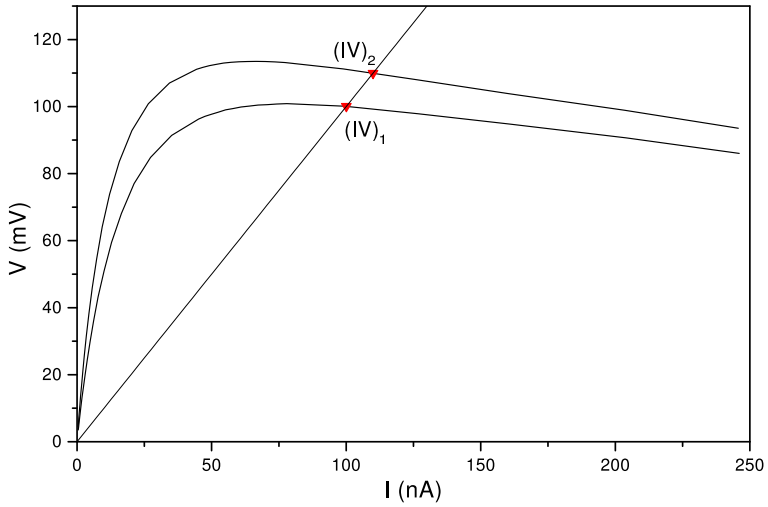

Figure 2.5: Load curves taken during observation of blackbodies at 300 K (lower) and 77 K (upper). A line of constant resistance and therefore of constant temperature is plotted.

Advanced calibration

The best calibrator on the sky for space or balloon-borne experiments is the CMB dipole, measured to better than 1 % precision by COBE (Fixsen et al., 1996).
For ground-based experiments one can use the planets, which unfortunately are not known with the same precision, leading to an error of 5 to 10 % in the best case. When the planets are not visible, the calibration can be done with the so-called secondary calibrators, i.e. objects with a constant flux density measured against planets.

Chapter 3

Cooling Below 1 K

As seen in the previous chapter, bolometers have to be cooled to a temperature close to absolute zero to operate and to minimize the noise contributions. In particular, for observations at 2 mm where the atmospheric emission is relatively low, cooling below 100 mK is required to avoid being limited by the system noise.

3.1 Cooling Fundamentals

The simplest way of cooling to low temperature makes use of a liquid with low boiling point. The liquid stays cold thanks to evaporation, i.e. the heat inflow from the surroundings is absorbed and produces the phase transition. The smaller the latent heat of vaporization is, the better the liquid has to be thermally insulated to reduce the loss per unit time. A discussion of such techniques is outside the scope of this thesis, but for a detailed review see for example White (1979). Latent heats of some typical cryo-liquids are given in Table 3.1. A further decrease in the temperature

Gas	CO_2 §	O_2	N_2	Ne	H_2	^{4}He	^{3}He
Latent heat (J/g)	173	213	199	86	441	20.6	8.2
Latent heat (J/ml)	933	243	161	103	31	2.6	0.48
Boiling point (K)	194.6	90.2	77.3	27.2	20.4	4.2	3.2
Density (g/ml)	1.63	1.14	0.81	1.20	0.070	0.125	0.059

Table 3.1: Latent heat of vaporization, boiling point and density at standard atmospheric pressure of cryogenic fluids. § Solid.

can be obtained by pumping off the vapour phase which is in equilibrium with the liquid, in order to lower the boiling point. As one can see from Fig. 3.1, the vapour pressure diminishes exponentially as a function of temperature and so the minimum achievable pressure limits the minimum temperature. To reach temperatures lower than 0.3 K, other methods have to be used. The only technique that allows continuous operation at temperature as low as few mK is based on the "evaporation" of ^{3}He in a ^{4}He environment, instead of in vacuum as for standard ^{3}He refrigerators. To describe

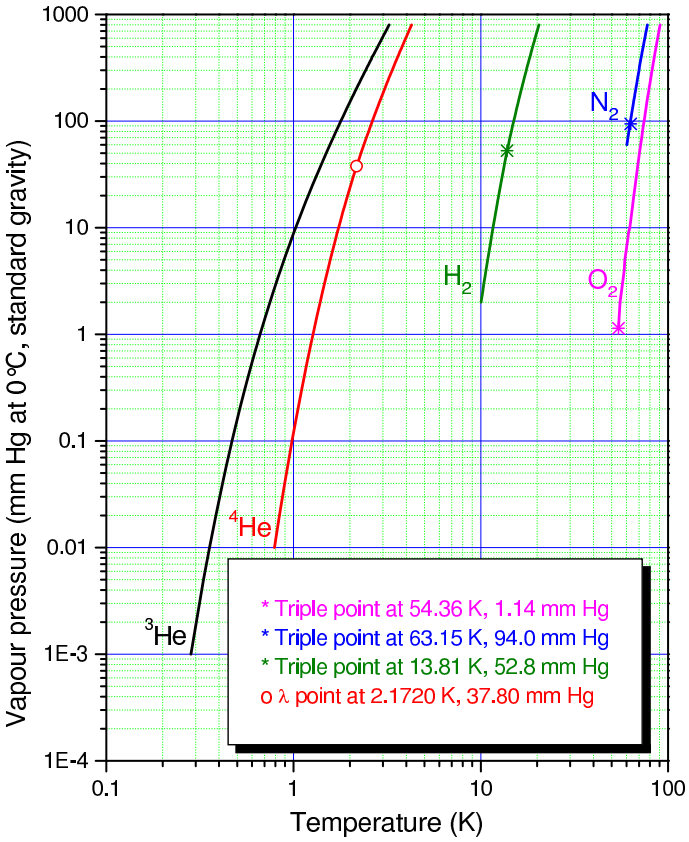

Figure 3.1: Temperature vs vapour pressure diagram for common cryofluids.

the operation principle of the so called ^{3}He/^{4}He dilution refrigerators, it is useful to recall the basic properties of these two isotopes.

3.2 Liquid Helium Properties

The common stable isotope of helium is ^{4}He, which is obtained today exclusively from helium-rich natural-gas sources where the geological structure that holds the natural gas also traps helium that is a product of radiactive alpha decay. The rare isotope ^{3}He constitutes a fraction (1 to 2)$\cdot 10^{-7}$ of helium gas from natural gas sources and about $1.3 \cdot 10^{-6}$ of the helium gas in the atmosphere. Separating ^{3}He in a reasonable amount from these two sources is very costly, thus the ^{3}He used today in low-temperature physics experiments comes from nuclear reactors as a byproduct of tritium manufacture (Eq. 3.1). Because of this method of production, ^{3}He remains very expensive (about 150 euro per liter of gas at STP) and the refrigerators that require its use are normally sealed.

$$\begin{aligned} {}^6_3\mathrm{Li} + {}^1_0\mathrm{n} &\Rightarrow {}^3_1\mathrm{T} + {}^4_2\mathrm{He}\ , \\ {}^3_1\mathrm{T} &\overset{12.3\,\mathrm{yr}}{\Longrightarrow} {}^3_2\mathrm{He} + {}^0_{-1}\mathrm{e} + \bar{\nu} \end{aligned} \tag{3.1}$$

Liquid helium displays important quantum mechanical effects because of its low molecular weight and chemical inertness. The closed electronic s-shell of helium makes the binding van der Waals forces between the atoms very weak, and so helium has no static dipole moment. Also, due to the small atomic mass,m, the two helium isotopes have a large quantum mechanical zero-point energy, E_0, given by

$$E_0 = \frac{h^2}{8ma^2}$$

where $a = (V_m/N_0)^{1/3}$ is the radius of the sphere to which the atoms are confined, N_0 is Avogadro's number, and V_m is the molar volume. For these reasons, the boiling point of helium is lower than for any other liquid and there is no triple point (helium is solidified only under pressure). Thus, it can be used as a refrigerant at extremely low temperatures.

3.2.1 Superfluidity

About 1927 Keesom and Wolfke at Leiden measured the dielectric constant of liquid helium as a function of temperature. They found a small apparent discontinuity in the curve at a temperature in the vicinity of 2.2 K. it was suggested that liquid helium at that temperature undergoes some sort of tranformation. ^{4}He nuclei have integer total spin and thus obey Bose-Einstein statistics. The transformation discovered by Keesom and Wolfke is the liquid helium Bose-Einstein condensation, a second order phase transition that leads helium into a superfluid state (He II). The resulting anomaly in the curve of specific heat as a function of temperature

$$C_V = -T \left. \frac{\partial^2 G}{\partial T^2} \right|_V$$

where G is the Gibbs heat function, is named the lambda transition due to its shape (Fig. 3.2). The properties of liquid ^{4}He below lambda can be described by using the two-fluid model, proposed by Landau and Kapitza (a history of the investigation is reported by Andronikashvili 1990). This model relies on two postulates:

1. The He II consists of a "background phase" (superfluid) plus an excited (higher energy) phase (normal fluid). These two phases can be formally described by densities ρ_s and ρ_n, where the subscripts refer to superfluid phase and normal phase, respectively. The concentration of the two phases with respect to the "ordinary" density of the liquid, ρ, depends on the temperature:

$$\begin{array}{lll} \rho_s + \rho_n = \rho & & \\ \rho_s = \rho & \rho_n = 0 & T = 0 \text{ K} \\ \rho_s = 0 & \rho_n = \rho & T = \lambda \text{ point } (T_\lambda) \end{array}$$

2. The viscosity of the superfluid is zero and is energetically at absolute zero, i.e. its entropy is zero. In contrast, the normal fluid possesses both viscosity and entropy.

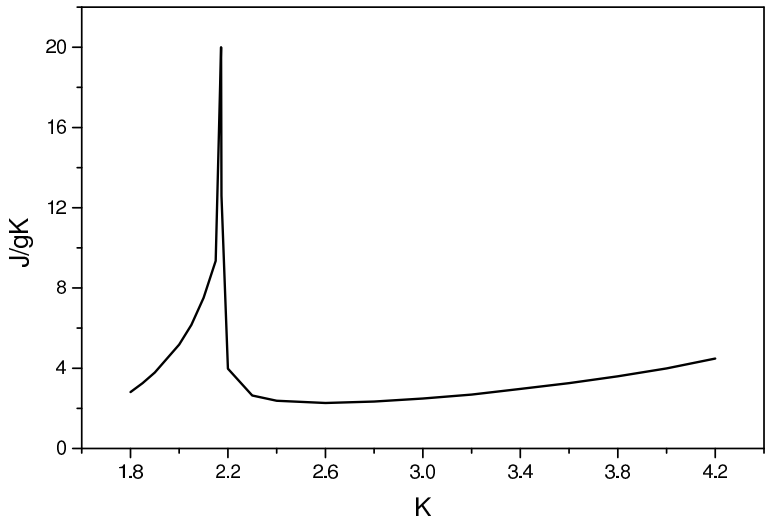

Figure 3.2: Heat capacity of ^{4}He at saturation.

The correctness of these postulates has overwhelming experimental evidence. Despite the apparent simplicity of these assumptions, they are sufficient to explain all peculiar properties and behaviour of superfluid helium, such as fountain effect and mechano-caloric effect (for a review, see for example Lane 1962). The absence of entropy in the superfluid component has the important consequence that these particles do not interact with either the normal component or with any other particle. As we will see, this is of major relevance in the ^{3}He/^{4}He dilution principle.
The ^{3}He nucleus is composed of an odd number of elementary particles (i.e. two protons and one neutron). Thus it has an antisymmetric wave function and follows Fermi-Dirac statistics. Therefore, single ^{3}He atoms cannot undergo the analogue of a Bose-Einstein momentum condensation into a superfluid state. A weak interaction between ^{3}He atoms in the liquid gives rise to pairing of ^{3}He atoms. Like the paired conduction electrons in a superconducting metal, the paired ^{3}He atoms behave like bosons and can undergo a transition into a superfluid state. However, because the pairing forces are rather weak, this transition occurs only at 2.5 mK, and for most experimental conditions ^{3}He behaves like a normal fluid.

Second Sound Waves

Due to its poor thermal conductivity (about 10^4 times lower than the thermal conductivity of copper) in the normal fluid state, ^{4}HeI boils with strong bubbling. Conversely, below lambda, in the superfluid state, the thermal conductivity of ^{4}HeII is quite large, and can be more than 80 times higher than the thermal conductivity of copper at room temperature. Therefore, a temperature gradient between the bottom and surface of the liquid cannot be established, and the boiling of superfluid ^{4}He is quiet. Thanks to the high thermal conductivity, temperature waves or entropy waves can propagate in this unusual liquid. These waves are improperly referred to as second sound waves, to distinguish them from the usual first sound, the density waves. A mathematical treatment of the second sound in ^{4}He can be found in Bennemann &

Ketterson (1976). The coupling between first and second sound waves in superfluid helium is weak, because it occurs via second-order terms. On the other hand, coupling between second sound in superfluid and first sound in the gas above the liquid is possible and can have important effects. We will come back to this in the next chapter.

3.3 ^{3}He/^{4}He Dilution Refrigerators

A detailed treatment of dilution refrigeration is provided by Lounasmaa (1974) and Pobell (1996), and the thermodynamic properties of dilute solutions of ^{3}He in ^{4}He are elegantly reviewed by Ebner & Edwards (1971).
The principle of the dilution refrigerator was originally suggested by London (1951). It is based on the property of a ^{3}He/^{4}He mixture to separate spontaneously into two phases below 0.867 K (Fig. 3.3): a ^{3}He-rich phase and a ^{4}He-rich phase. The ^{3}He-rich phase is less dense and therefore floats on top of the ^{4}He-rich phase. The cooling is

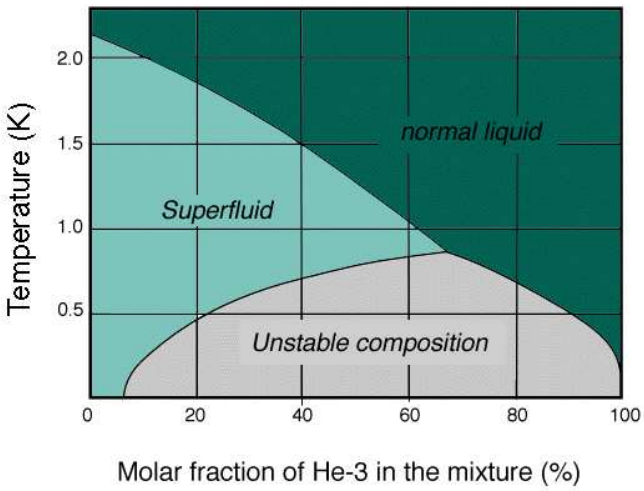

Figure 3.3: Phase diagram of ^{3}He/^{4}He mixtures. From Berglund (1995).

produced by the ^{3}He atoms when they move across the boundary from the upper, almost pure ^{3}He phase, to the lower, dilute phase. The mechanism is somewhat similar to ordinary evaporation, with the superfluid ^{4}He acting as mechanical vacuum in which the Fermi-Dirac ^{3}He gas is evaporating. This process is an efficient way to reach very low temperatures because the equilibrium concentration of ^{3}He in ^{4}He remains finite and rather high (about 6.6%) even at absolute zero.

In practical dilution refrigerators, the phase separation occurs in a mixing chamber (Fig. 3.4) from which an osmotic pressure gradient drives the ^{3}He atoms, through the heat exchangers, to a still where they are evaporated. At the temperature of the still (about 0.7 K) the vapour pressure of ^{4}He is two orders of magnitude lower than the vapour pressure of ^{3}He, therefore the evaporated gas is mainly ^{3}He. The vapour is removed by pumping (normally by a turbo-molecular pump in series with an oil-free

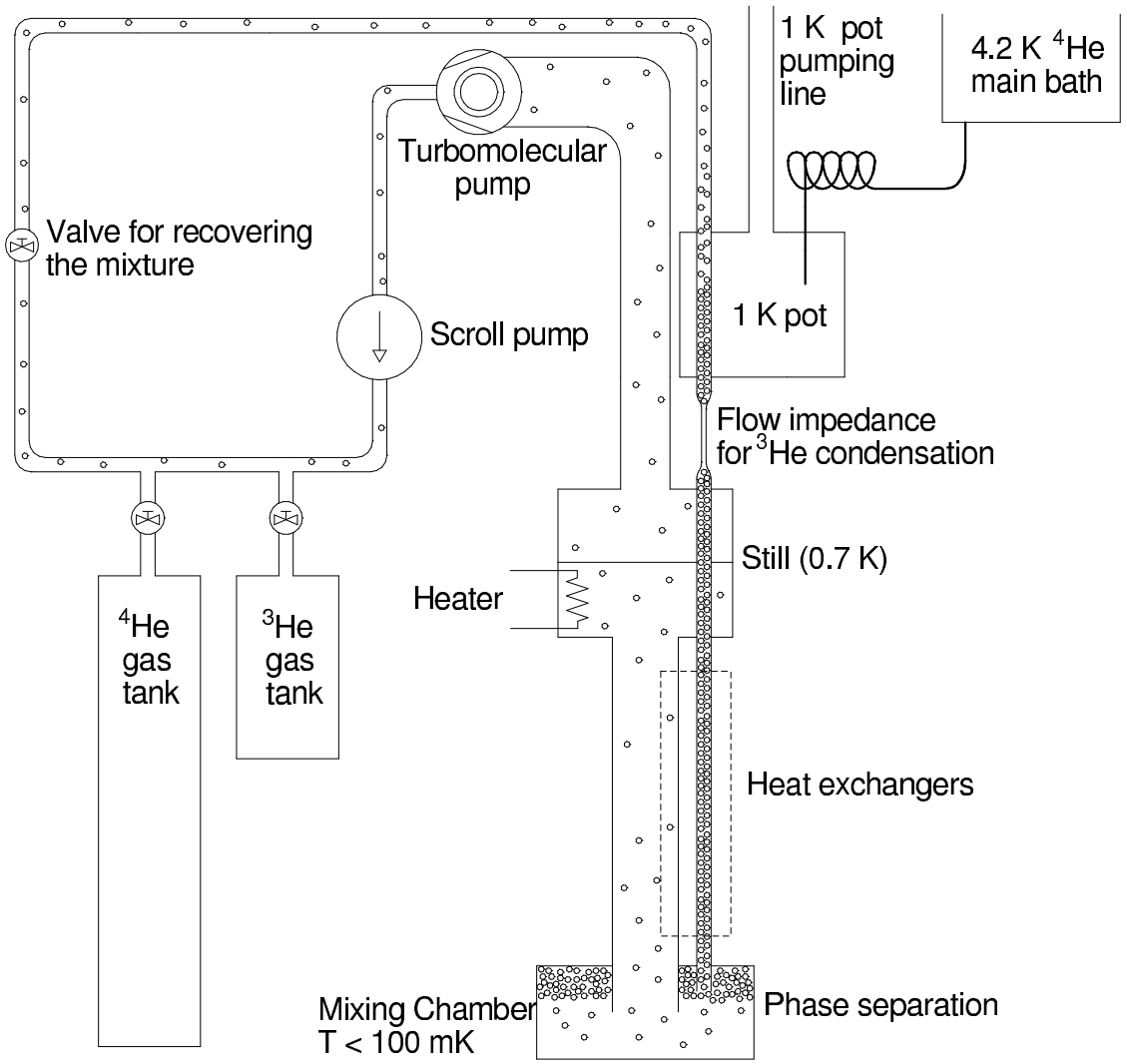

Figure 3.4: Schematic set-up of a dilution unit. Circles represent the ^{3}He atoms. See text for description.

pump such as a membrane or scroll pump). The gas is then precooled and liquified in a condenser at about 1 K. The pressure of ^{3}He is kept sufficiently high to allow condensation by means of a flow impedance. The condenser is attached to a ^{4}He pumped chamber, generally called the 1 K pot. This pot is continuously replenished from the main ^{4}He bath at 4.2 K through a flow impedance. The temperature of liquid ^{3}He is lowered by exchanging heat with the column of dilute phase before reinserting it in the mixing chamber.

Chapter 4

The Hundred Millikelvin Bolometer Array

The Bolometer Development Group at the MPIfR has built HUMBA (HUndred Millikelvin Bolometer Array), a bolometer array for observations at 2 mm wavelength (Reichertz et al., 2001a). To operate with background limited sensitivity even under excellent weather conditions, the system noise is greatly reduced by cooling the bolometers below 100 mK. Such a low temperature is reached by means of a MiniKelvin Model 40 T (Leiden Cryogenics B.V.) ^{3}He/^{4}He dilution refrigerator. The dilution unit is mounted in a special cryostat designed and built by a German company (Cryovac GmbH) to our specifications. HUMBA saw first light in February 1998 at the Heinrich-Hertz-Telescope (HHT) in Arizona and provided first astronomical results in November 1998, including a preliminary detection of SZ effect in the cluster CL0016+16 (Gromke et al., 2001). In the original configuration (Gromke, 2000), HUMBA operated with an array of seven channels, arranged in a close-packed hexagon. The performance of the system was seriously limited by an excess of low-frequency noise in the detectors, whose origin was at that time unknown. This problem was solved during the work of this thesis; the subsequent improvement to the dilution unit has been covered by a patent application (Raccanelli et al., 2001d). The investigation and the solution are reported in section 4.5 of this chapter.

4.1 Optics

The millimeter radiation is coupled to the detectors through conical horns. Since bolometers are in principle sensitive to radiation at any wavelength, the desired bandpass is selected by a series of optical filters (Fig. 4.1), placed in front of the array at various temperature stages. A high density, 10 mm thick polyethylene disk plus a 0.1 mm black polyethylene foil at the 300 K window of the cryostat stop visible and near-infrared radiation. At 77 K, a capacitive multilayer mesh system acts as a long-wavelength bandpass filter, and a 4 mm thick crystal quartz absorbs radiation with wavelength between 5 μm and 330 μm. A 6 mm thick Duran plate and a bandpass filter, consisting of an interference stack of resonant inductive meshes, are installed at

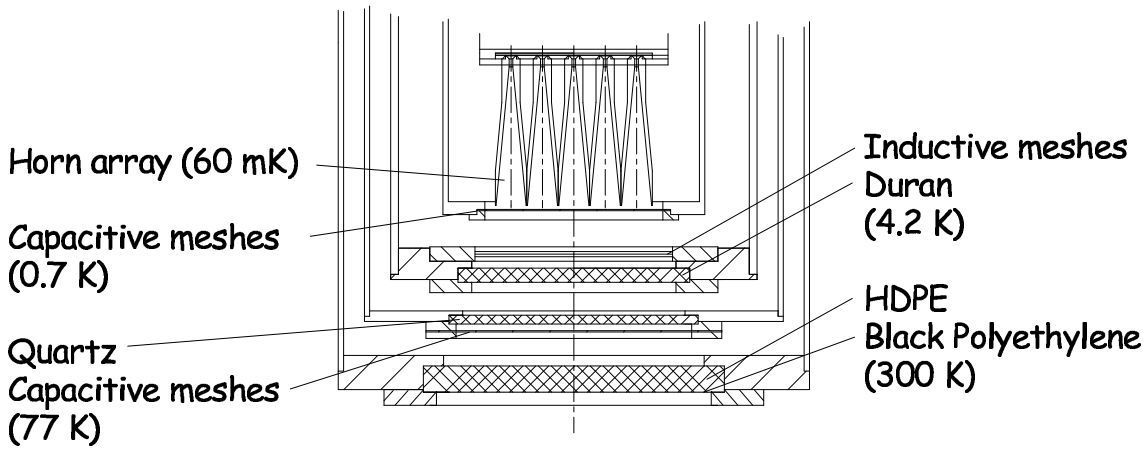

Figure 4.1: Layout of the optics inside the cryostat. Conical horns couple the radiation from the telescope optics to the bolometers. A short piece of cylindrical waveguide acts as an efficient high pass. A combination of filters on the various temperature stages provide define the frequency bandpass for the bolometers.

4.2 K. On the last shield before the horns, at 0.7 K, there is a further lowpass filter made of multilayer capacitive meshes. Cylindrical waveguides about two diameters long at the end of each horn provide a high pass. The polyethylene, the glass, and the quartz windows have anti-reflection grooves for 2 mm wavelength. The use of interference meshes at 4.2 K resuls in good RF-shielding of the inner chamber.

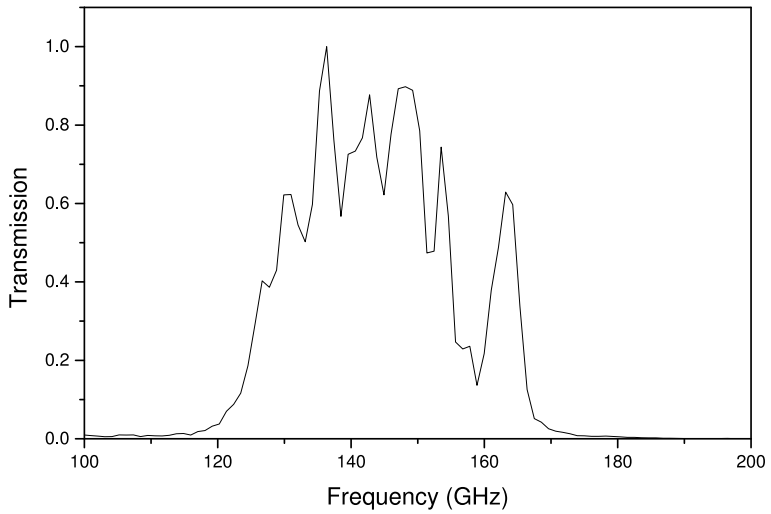

Figure 4.2: Measured spectral response of the filter system. The presence of fringes is due to possible interference between the two surfaces of a filter or between two filters with high refractive index (as quartz and Duran). These fringes proved to be stable and reproducible and therefore do not constitute a problem for the performance of the system.

The transmission properties of the filters are known only at room temperature.

Furthermore, when using filters with a significant reflection, the spectral response of the system cannot be calculated by simple multiplication of the individual spectra, and must be derived experimentally. The spectral response of the filter system was measured with a Martin-Puplett (M-P) Interferometer (Martin & Puplett, 1969) observing a 77 K blackbody. The transmission spectrum was corrected for the source emission profile and is shown in Fig. 4.2. These measurements also allow one to check for near-band leaks. Possible leaks at higher frequencies are rarely seen because of the reduced sensitivity of the M-P, but their existance can be deduced by the overall performance of the system (e.g. load curves of the bolometers will show an excess radiative load). Since any overlap of the bandpass with atmospheric absorption lines would introduce additional noise, a careful match to the atmospheric window is required. In Fig. 4.3 the spectral response of the HUMBA bolometers is compared to the atmospheric transmission in the submm/mm wavelength range.

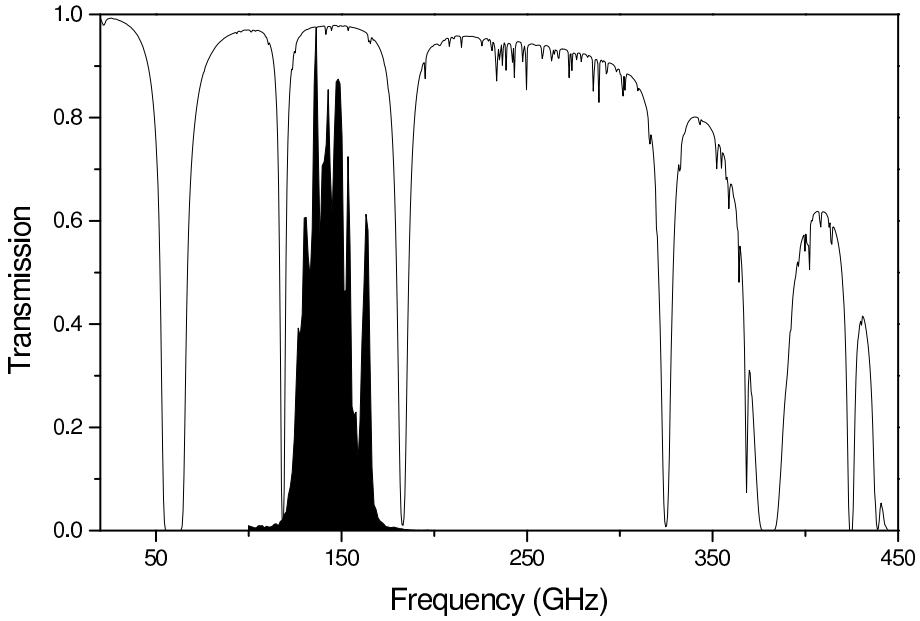

Figure 4.3: Atmospheric transmission in the submm/mm wavelength range at 2 mm precipitable water vapor (solid line) and spectral response of the 2 mm bolometer (filled area).

4.2 Detectors

The bolometer array of HUMBA has been upgraded to 19 detectors. Three-dimensional numerical simulations were carried out by the group of Prof. Hansen at the University of Wuppertal to maximize the wideband absorption of bolometers placed close to the exit of a circular waveguide. These simulations show that for a quarter wavelength thick silicon substrate with a metal film on the back, efficient absorption can be obtained even without a back mirror (Fig. 4.4). When the metal film is on the silicon nitride

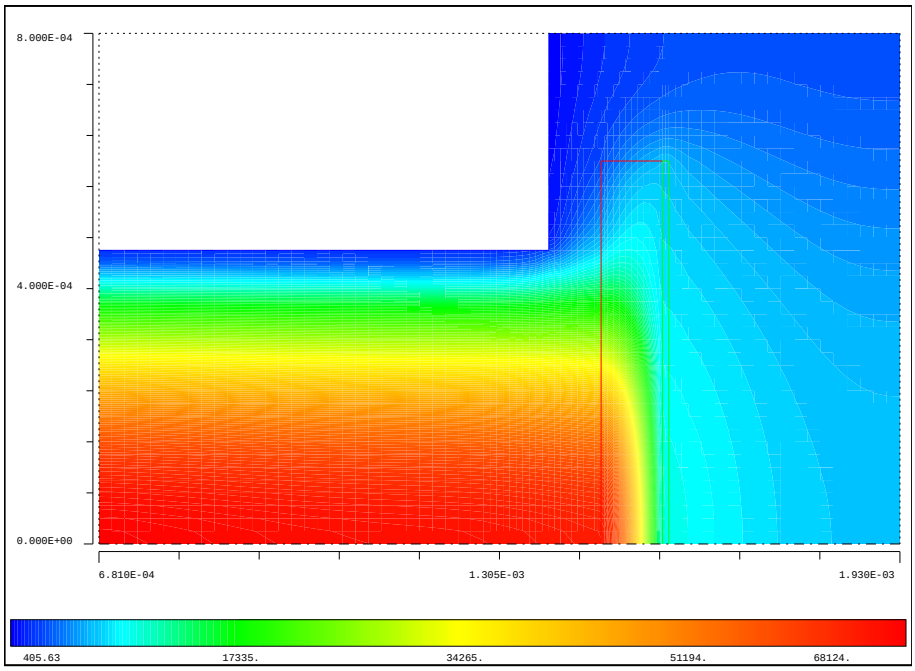

Figure 4.4: Numeric simulation of the electromagnetic field close to the exit of a cylindrical waveguide. On the right of the waveguide there is the silicon substrate (red box), which acts as a tranformer, followed by a quarter wavelength thick metal layer (green box) that absorbs the radiation. The horizontal axis is the distance along the waveguide. The vertical axis is the distance from the axis of the waveguide. Units are meters. EM field intensity in arbitrary units. From Hansen (1998).

membrane only and a quarter-wavelength reflector is placed behind it, satisfactory absorption can be achieved if the waveguide is flared into a small horn (Kreysa et al., 2001). The new MPIfR bolometer arrays are built according to this principle. Omitting the silicon substrate (Fig. 4.5 a) greatly simplifies the bolometer construction, as the substrate had to be added manually and therefore was the weak point of the bolometer production chain. The silicon nitride membrane is 1 μm thick; the NTD Germanium thermistor is connected across the edge of one of the gaps of the gold ring (Fig. 4.5 b and c); the electrical connections, provided by either brass wires or photolithographed metal, define the thermal conductivity of the bolometer. If the electrical contacts are located on the same surface of the NTD chip, the thermistor can be bonded directly onto the metal ring. Otherwise the connections to the ring are provided by either bonded or glued wires.

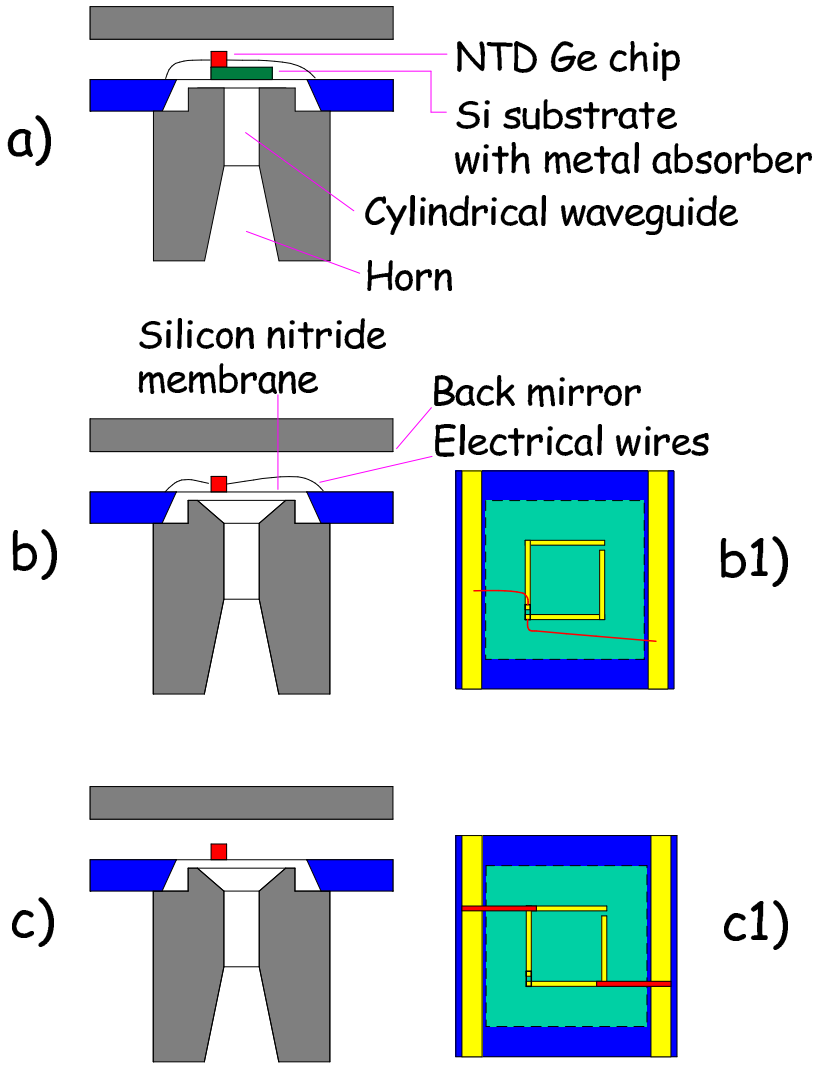

Figure 4.5: a) Layout of a composite bolometer with the metal absorber deposited onto a silicon substrate. b) Layout of a bolometer with the metal film deposited onto the silicon nitride membrane, with electrical connections to the bolometer provided by brass wires. b1) is a top view of the figure in b). The silicon nitride membrane (acquamarine) is 5 x 5 mm in size. The thermistor (solid black line) is connected across the lower left gap of the gold ring (yellow). Electrical connections are provided by brass wires (red). c) and c1): same as b) and b1), with the electrical connections provided by a photolithographed layer of niobium or gold (red).

4.3 Cryogenics

Fig. 4.6 shows a sketch of the cryostat. A liquid nitrogen bath and a liquid ^{4}He bath provide heat sinks for the radiation shields that surround the dilution insert. The bolometer array is mounted on the mixing chamber, at the lower end of the dilution unit, looking downwards through the windows at the bottom of the cryostat. A further cylinder is connected to the still at 0.7 K to shield the low temperature environment.

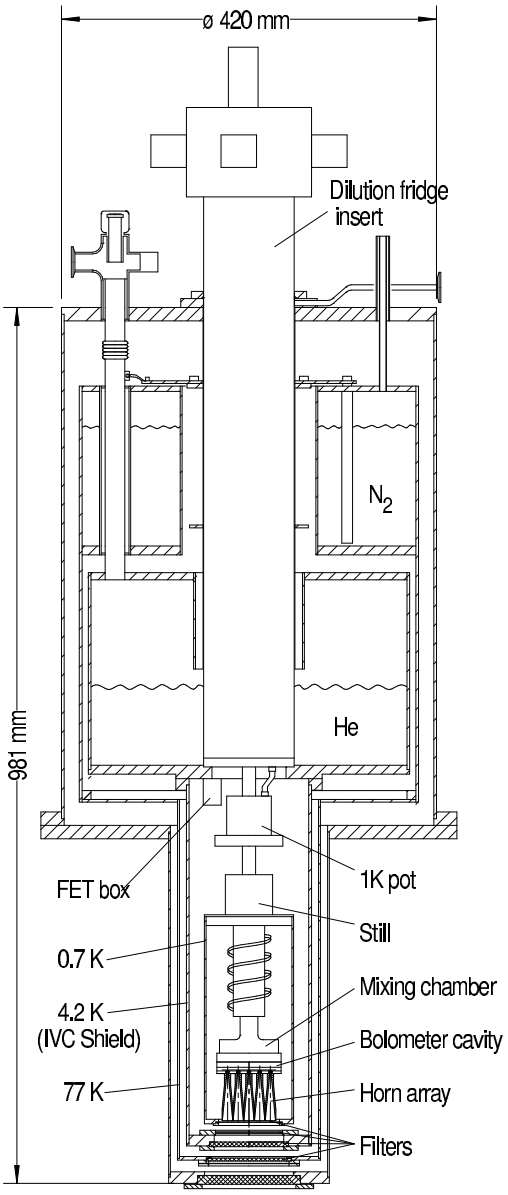

Figure 4.6: HUMBA cryostat. The dilution insert is surrounded by shields at liquid nitrogen and liquid helium temperatures. The bolometer environment is further shielded by a cylinder connected to the still, at 0.7 K.

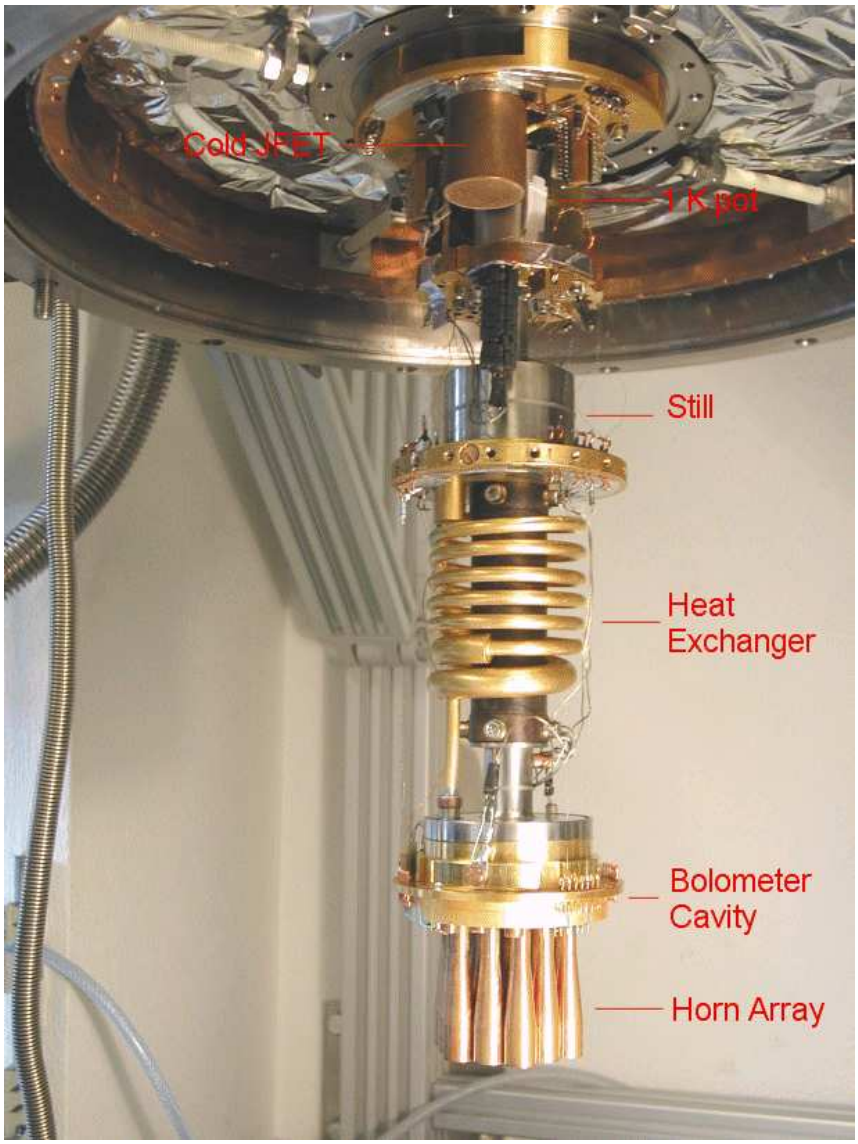

Figure 4.7: The lower part of the HUMBA dilution insert, with the bolometer and horn array mounted.

The inner part of the cryostat is divided into an inner vacuum chamber (IVC) and an outer vacuum chamber (OVC). The two chambers are separated by the 4 K shield, which is indium sealed to the ^{4}He tank.

To allow fast precooling of the insert, the IVC is pressurized with about 150 mbar of ^{4}He gas, and the ^{3}He line with about 250 mbar. After evacuating the OVC, liquid nitrogen is transferred to the 12 liters nitrogen tank and to the 8 liters helium tank. During precooling of the helium tank the 1 K pot is kept under He pressure to keep liquid nitrogen out. Once thermalization to 77 K is reached (after at least six hours), the nitrogen is removed from the helium tank and liquid helium is transferred. The system thermalizes to 4.2 K in about three hours. The 1 K pot pump is then started and, after about 20 minutes to allow the 1 K pot to fill, the mixture can be condensed. The working temperature of about 60 mK is reached about four hours after starting

the dilution process. Continuous operation is provided by circulating 60 μMol/s of ^{3}He by means of a turbomolecular pump in series with a scroll pump. The system needs refilling with liquid helium and liquid nitrogen once every 24 hours. ^{4}He consumption is reduced by cooling the dilution insert with the evaporating ^{4}He gas. The use of the enthalpy of the helium gas substancially reduces the heat load on the 4 K environment (see for example Conte 1970 or Raccanelli 1997 for a more detailed treatment).

4.4 Electronics

To use HUMBA at a telescope equipped with a secondary mirror wobbling at a typical frequency of about 2 Hz, the read-out electronics need to have their best noise performance in this low audio-frequency range. Best results in voltage and current noise for the high impedance germanium thermistors are obtained with JFETs, which have best performance at a temperature of about 130 K. The bolometer signals are read out with a source follower amplifier using Toshiba SK369 JFETs. These JFETs are inside a shielded box at the 4 K plate, the closest possible place for a 130 K source in the environement of 100 mK bolometers. The close proximity of this first amplification stage to the detectors is necessary to minimize the length of the high-impedance circuitry, thus reducing the amount of wiring susceptible to microphonic pick-up, channel-to-channel cross-talk, and radio frequency (RF) interference. Warm electronics outside the cryostat amplify the signals by means of differential amplifiers, consisting of a pair of SK369's, and subsequent operational amplifiers for each channel (Fig. 4.8). To prevent radio interference from reaching the bolometers via wires, we use

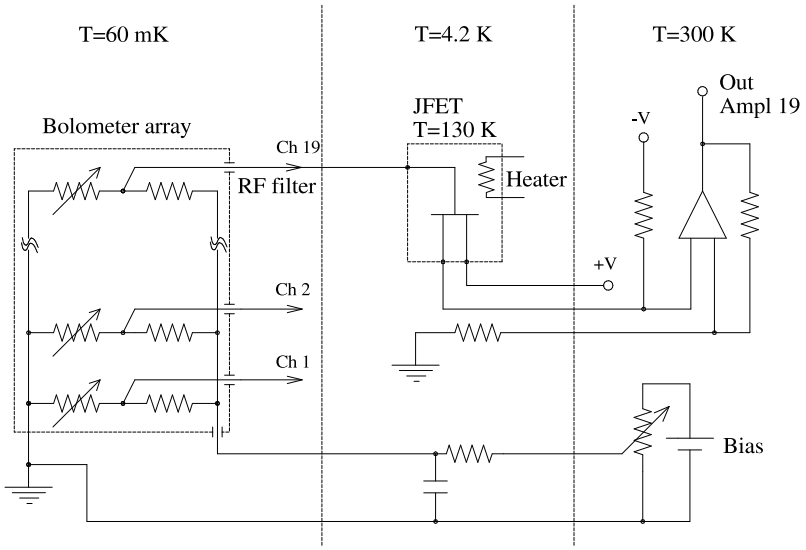

Figure 4.8: The read-out electronics. The bolometer impedance is lowered by means of the cold JFET stage in source-follower configuration, and the signal is amplified by the warm electronics.

cold RF feedthrough filters in each signal line entering the bolometer cavity.

Once the operating temperature for the bolometer has been reached, a heater on the cold JFET stage is switched on to raise the stage temperature to above 100 K. The cold electronics is then started and the temperature is maintained by self heating of the JFETs.

4.5 Noise Excess

Based on the paper by Raccanelli et al., published in Cryogenics ***41****, 763 (2001).*

The noise spectra of the HUMBA bolometers showed an excess low-frequency noise, changing in amplitude from time to time (Fig. 4.9) in an unpredictable way, and increasing by almost three orders of magnitude in the worst case. It is known that

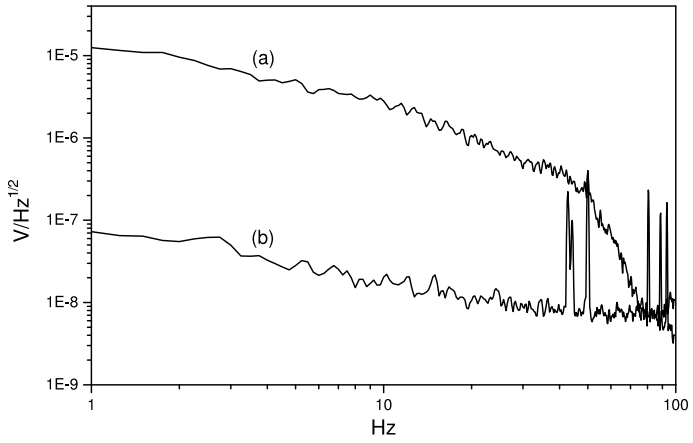

Figure 4.9: Noise spectra of the bolometer signal. The noise varied in amplitude from time to time from a maximum (a) to a minimum (b), possibly due to different experimental conditions (e.g. depending on the heat load and on the He level insiede the pot).

continuously filled 1 K pots are a source of vibrations that affect cooled experiments, and vibrations can result in electrical, mechanical, and thermal noise (Bhatia et al., 1999). Electrical noise is generated by mechanical modulation of the capacitive couplings or by generation of parasitic currents if the detector wires are moving in magnetic fields. The mechanical vibrations themself constitute an unwanted signal for detectors measuring a position (gravitational-wave antennas and torsional oscillators). Thermal noise is of particular interest for bolometers. As discussed in chapter 2, the dissipation of vibrational energy may cause variations in the detector temperature or a drift in the system temperature. This gives rise to a spurious signal whose amplitude increases with the integration time and therefore appears as noise at low frequencies.

4.5.1 State of the Art

Two approaches for reducing the vibrational noise in the 1 K pot have been suggested: mechanically decoupling the experiment (Pirro et al., 2001), or regulating of the helium flow from the main bath and adjusting of the helium level inside the 1 K pot itself (Lawes et al., 1998). The first method can be expensive in terms of time and money, especially if it is necessary to rebuild the cryostat. Decreasing the helium flow toward the 1 K pot may be in conflict with the requirements of cooling power, and making a level adjustment by means of a heater causes an increase in the thermal load and therefore in the liquid helium consumption. Moreover, these methods provide only a partial attenuation of the noise and do not eliminate its origin and in some experiments may not be sufficient to solve the problem.

4.5.2 Investigation

No systematic study of the mechanism of vibrational noise generation has been reported in the literature, even though this noise source affects several experiments in different fields of research (e.g. gravitational-wave antennas, torsional oscillators, bolometer detectors, ultra-low temperature physics). In order to understand and to eliminate the source of noise, we investigated the known mechanisms that can induce vibrations, and we made the following tests and observations.

Resonant oscillations of the gas column (Taconis et al., 1949) can occur a in long, narrow tube with a large temperature gradient its length, if the bottom end is below about 20 K. These oscillations can occasionally be quite useful, for example for a simple helium level detector commonly used in laboratories (Gaffney & Clement, 1955). However, when they occur in the helium venting line of a cryostat, they can dramatically increase the evaporation rate and lead to strong acoustic vibrations. To prevent possible resonant oscillations in HUMBA, we inserted a damping structure inside the 1 K pot pumping line but no improvement of the bolometer noise was observed.

Fluctuations of the base temperature may be a cause of $1/f$ noise but the cold plate temperature was found to be sufficiently stable, as measured by a thermistor mounted outside the array.

An important step forward was taken with the following observation. After switching off the 1 K pot pump and allowing the pressure to rise for a short time above about 50 mbar, corresponding to a temperature higher than the lambda point, the excess noise suddenly disappeared. Restarting the pump, the noise appeared again once the temperature of the 1 K pot had dropped below the lambda transition. This effect was perfectly reproducible.

Since the noise disappeared when the bolometers were not biased, its source could not be electrical (e.g. mechanical modulation of the capacitive couplings) and therefore it was a pure bolometric signal. We replaced the bolometer array with a set of NTD germanium thermistors and the noise disappeared. The noise level of this sample of thermistor was similar to that of the bolometers in the noise-off state obtained by switching off the 1 K pot pump. We concluded that it was the vibrations of

the bolometer membrane that provided the mechanism of conversion of mechanical vibrations into thermal fluctuations.

We installed a piezoelectric crystal microphone so that it was in contact with the top flange of the 1 K pot. (Fig. 4.10). We observed that the 1 K pot, in its noisy state,

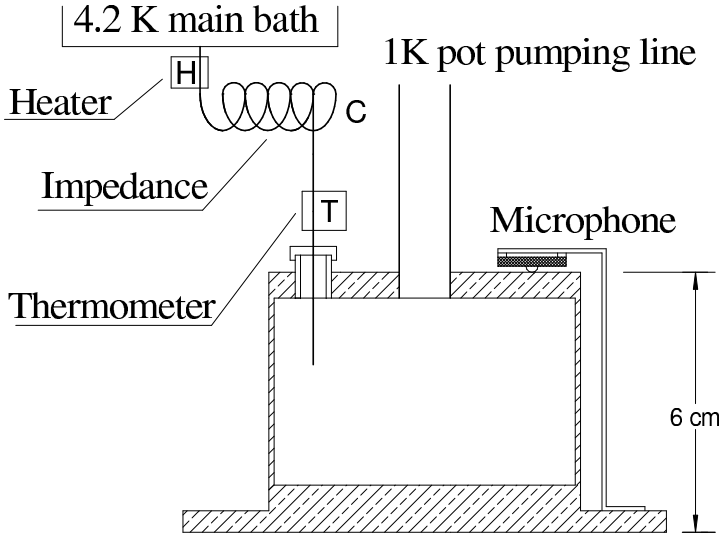

Figure 4.10: Sketch of our 1 K pot. H) resistive heater; T) thermometer; C) capillary acting as a flow impedance from the main bath at 4.2 K to the 1 K pot.

vibrates at a frequency between 816 and 880 Hz (Fig. 4.11), depending slightly on the contact point of the microphone. This allowed us to study the problem without having to run the dilution refrigerator, thus restricting our attention to the 1 K pot.

The connection between the vibration and the presence of superfluid helium inside the pot suggested us to investigate a mechanism of production of acoustic vibrations that is related to the possible presence of second sound waves. As in the Lane and Fairbank experiments (Lane et al., 1946, 1947), the periodic dissipation of power in a superfluid helium bath could cause the helium to evaporate in bursts and, by means of the coupling between second and first sound waves, generate vibrations of the top flange of the 1 K pot. Such electrical power could be generated through the pick up of the 50 Hz hum of the commercial net and dissipated in a stray resistance on the 1 K pot flange. To test for this, we removed all electrical connections anchored to the 1 K pot with the exception of the microphone and observed during a cryogenic run with this configuration that the noise persisted.

To explore the effect of rate of low of helium into the 1 K pot, we installed a thermometer and a resistive heater on the capillary that acts as flow impedance from the main bath. The thermometer was mounted next to the pot and the heater was soldered to the side of the main bath (Fig. 4.10). By activating the heater, it was possible to reproduce some of the published results (Lawes et al., 1998); applying electrical power, some of the liquid helium inside the capillary was vaporized which increased the impedance of the capillary. By reducing the helium flow, it was possible

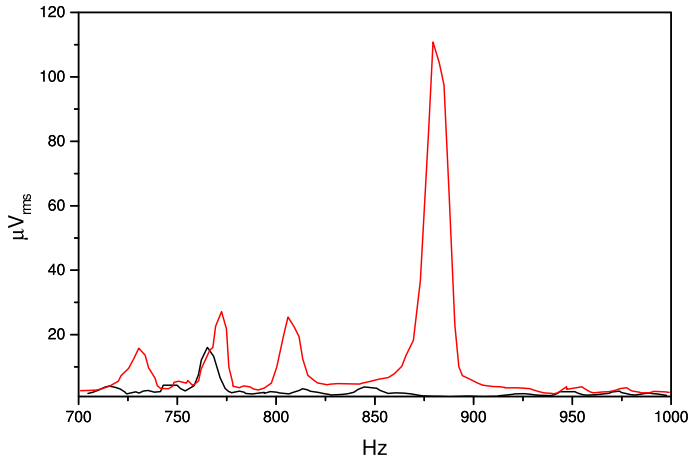

Figure 4.11: Noise spectrum of the microphone signal, before (red) and after (black) the solution. The line at about 880 Hz is the mechanical resonance of the pot. The residual exitation at about 730 Hz is not related to the 1 K pot vibration phenomenon, being possibly due to external mechanical vibrations of the apparatus.

to reduce the noise partially; if the flow was completely interrupted excess noise was reduced to zero.

We pumped on the main bath to reduce the temperature of the helium flowing into the 1 K pot, as measured by the thermometer on the capillary. A slight reduction of the noise was observed, until the transition to superfluid was moved inside the capillary itself, which occurred at main bath pressures below 300 mbar. Under these conditions, with the helium entering the 1 K pot already at a temperature below lambda, the noise completely disappeared.

4.5.3 Solution

The correlation of the noise with the helium in the 1 K pot being superfluid, the dependence on the temperature and particularly on the phase of the helium entering the pot indicated to us that the noise could be eliminated by introducing the helium into the 1 K pot already in its superfluid state. So, we arranged a simple heat exchanger internal to the pot by inserting a length of thin-walled copper-nickel capillary inside the 1 K pot (Fig. 4.12) so that it was immersed in the superfluid helium bath. The helium flowing from the main bath through the impedance flowed inside this capillary and thermalized to the bath temperature. In our case the capillary was 70 cm long and had 300 μm outer diameter and 100 μm wall thickness, but dimensions can be changed according to the size of the 1 K pot and the required flow.

Installing the heat exchanger eliminated the vibrations of the pot (Fig. 4.11). A further confirmation of the effectiveness of this solution came from measuring the noise spectra of the bolometric detectors (Fig. 4.13): the excess noise disappeared and the spectra were flat down to frequencies lower than the ones of interest for our experiment (a few Hz).

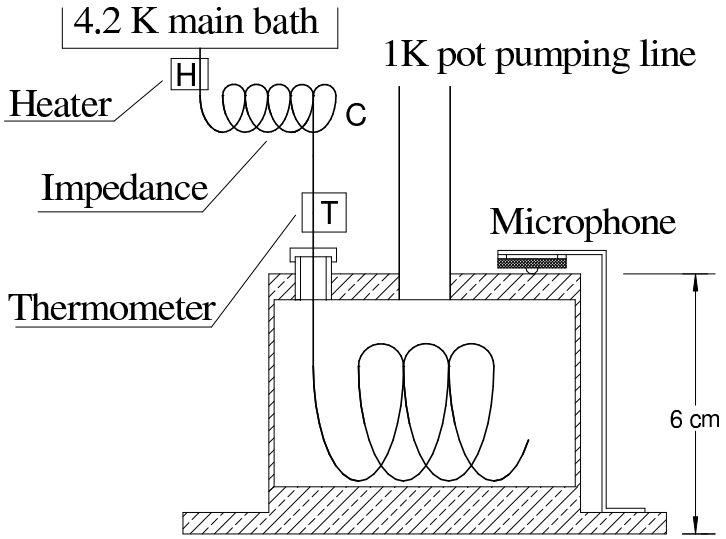

Figure 4.12: Sketch of the 1 K pot with the capillary inserted to act as heat exchanger. The helium coming from the main bath through the impedance flows inside this capillary and thermalizes to the bath temperature of the 1 K pot.

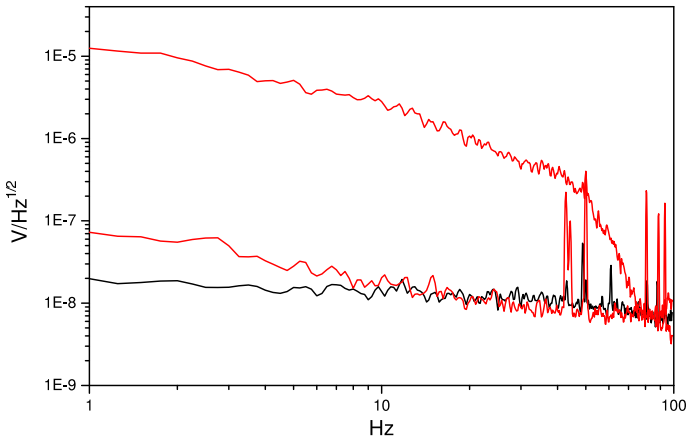

Figure 4.13: Noise spectra of the bolometer signal, before (red, taken from Fig. 4.11) and after (black) the procedure. In the noise-off state (black) the spectrum appears to be flat down to frequencies lower than the ones of interest for our experiment (a few Hz). The white noise level is slightly higher in the noise-off state than in the noise-on state at frequencies > 25 Hz, possibly due to a different base temperature of the system in the runs.

4.5.4 Discussion

When one injects HeI into the HeII bath inside the 1 K pot, the HeI deposits a large heat load onto a relatively small surface area of HeII due to the peak in the heat capacity of He at T_λ. This large heat current locally destroys the superfluid state and generates turbulence which results in an acoustic vibration of the pot.

A related phenomenon has been studied in the simple case of planar and cylindrical

heaters immersed in a superfluid helium bath with electrical power applied in pulses for very short times (Zhang et al. 1999 and references therein).

The mechanism of generation of vibration is probably more complex than simple cavitation, and a full theoretical treatment is beyond the aim of this work. The mechanical vibrations are transmitted down to the low-temperature stage, where they are converted into heat probably by the bolometer membrane. Since a bolometer is a relatively slow thermal detector, high-frequency variations of the temperature are integrated and converted into a slow and smoothed signal. Therefore, the resulting temperature fluctuations appear in the bolometers as low-frequency noise.

4.5.5 Further Experimental Evidence

The effectiveness of the technical solution that we have found to eliminate the vibrations in continuously filled 1 K pot has received confirmation from other research groups that became aware of this work at the international conferences where this investigation was presented (Raccanelli et al., 2001b,c).

The group of Prof. Packard, University of California at Berkley, implemented a heat exchanger internal to the 1 K pot of the dilution refrigerator that they use for superfluid ^{3}He weak links experiments (Simmonds et al., 1998). Our technology allowed them to solve the problem of vibrations (Hoskinson, 2002).

The Weak Interactions Group at the INFN (Italian National Institute for Nuclear Physics) in Milan had tried several modifications to their apparatus, including the mechanical decoupling of the experiment (Pirro et al., 2001) and the implementation of an additional flow impedance from the main bath, which was installed by Oxford Instruments, the company from which they bought the dilution unit. None of these methods had solved the problem. They eliminated the vibrations after hearing about our work when they cooled the helium flowing from the main bath below lambda, in a heat exhanger installed on top of the 1 K pot (Bucci, 2002).

Other groups are currently evaluating the modifications necessary to implement this solution.

4.6 Bolometer Test

Once the problem of the excess noise was solved, we started preparing a bolometer array to test HUMBA at the telescope. A new array was produced with the new layout described in Section 4.2 (see Fig. 4.5). For a preliminary test, only four NTD-Ge chips were mounted in the array. To characterize the array, a first run was made with no optical load (blind run). The detectors were obscured by means of a flange installed in place of the horns. Load curves taken at five different temperatures between 50 mK and 105 mK showed that the thermal conductance of the bolometers was too low (Fig. 4.14). Qualitative evidence comes from the well pronounced peak in the load curve at the lowest temperature, and from the fast decrease of the bolometer response when going to higher bath temperature. Since the background power that will be present during observations is not known accurately, we repeated the load-curve measurement

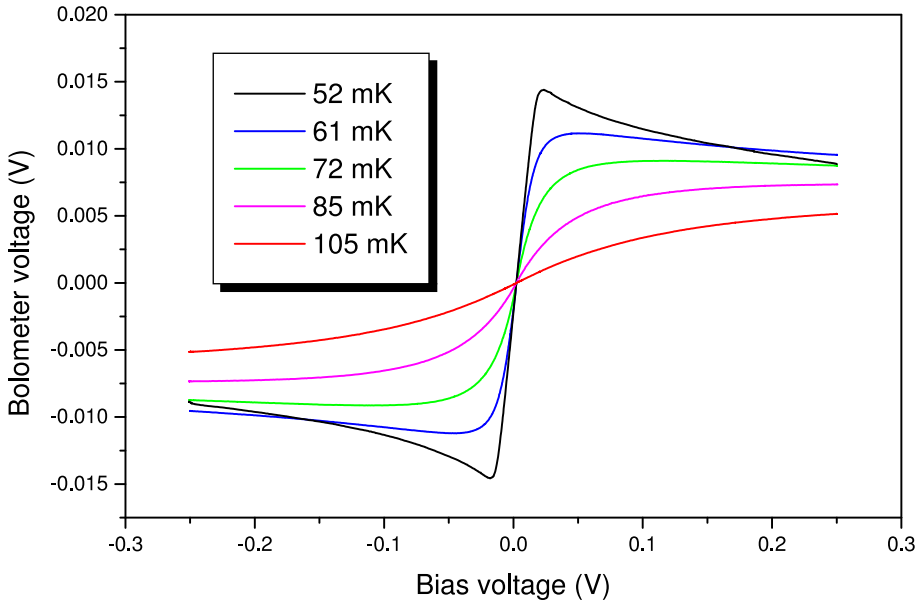

Figure 4.14: Load curves of one of the samples in the new-design array at five temperatures between 52 mK and 105 mK. A flattening of the curves with increasing bath temperature is evident, even in zero background conditions.

with an optical load, which unfortunately confirmed that the thermal conductance was too low (Fig. 4.15, bottom).

To measure the thermal conductance, G, one starts from the equilibrium equation 2.4, which is repeated here for convenience:

$$P + Q = G(T - T_0) \; . \tag{4.1}$$

The average thermal conductance, G, derived from this equation will be, in general, the sum of the contributions from the different materials used in the bolometer construction:

$$G \equiv \frac{1}{T - T_0} \int_{T_0}^{T} \sum_i g_i(T') dT' \; . \tag{4.2}$$

Measuring P and Q. The electrical power dissipated in the bolometer, $P = V \cdot I$, can be calculated from a load curve (see section 2.2). In a blind run this is the only contribution to the left-hand side of Eq. 4.1. This power is, in general, extremely small, and any possible light leak due to imperfect blind conditions will introduce a large error on the estimate of G. To reduce this uncertainity, one can estimate the optical background power, Q, by comparing load curves measured under blind and optical conditions (Fig. 4.15), as discussed in Section 2.9. One then uses the measured Q and P in Eq. 4.1 to determine G. From the blind and optical load curves we obtained a background power of about 60 pW.

Measuring T. The bolometer temperature, T, can be derived from the bolometer impedance, once the parameters R_0 and Δ in Mott's law (Eq. 2.58) are known. To determine the value of these two parameters, one requires a set of measurements

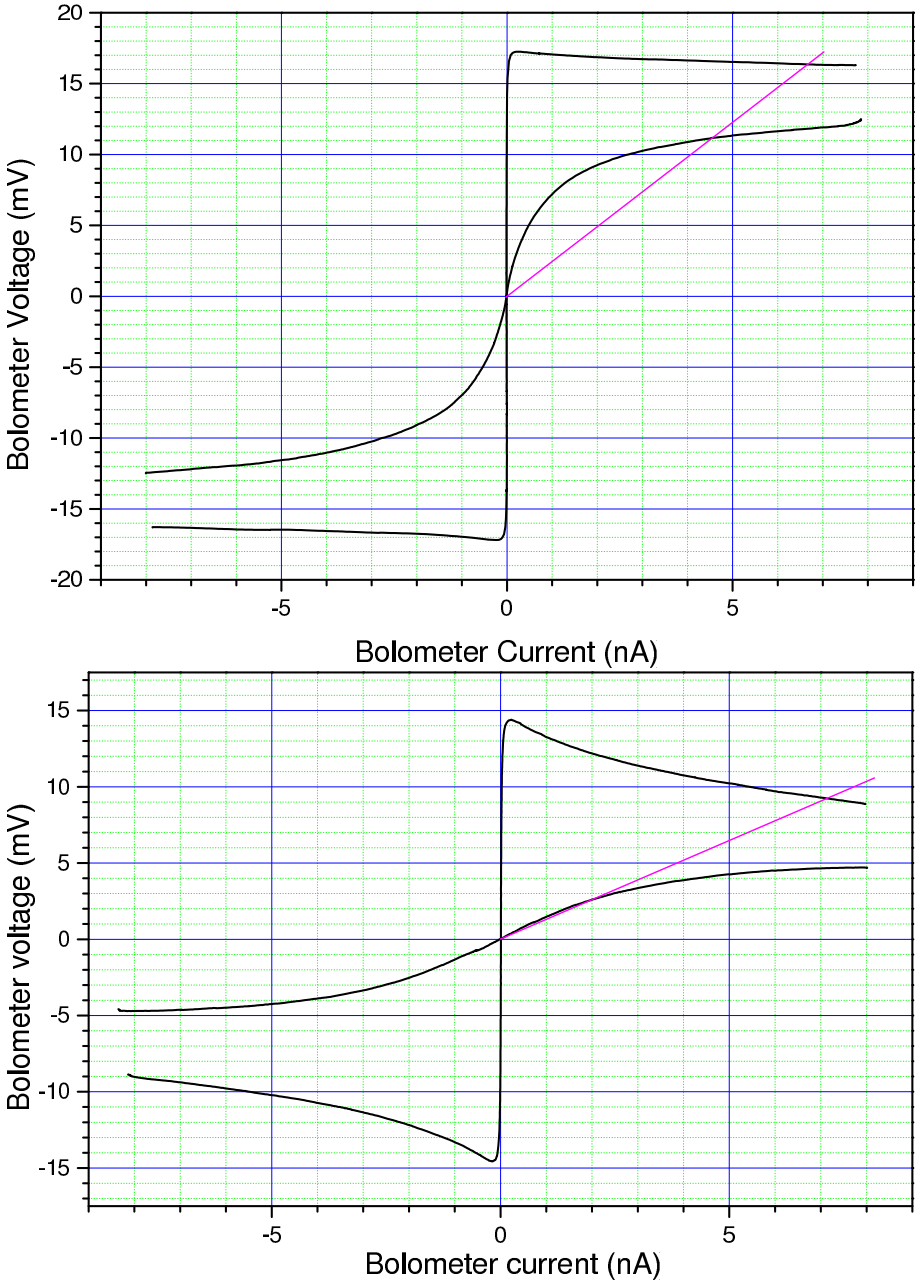

Figure 4.15: Estimate of the background power from the comparison of load curves taken in a blind run (*lower curves*) and in an optical run (*upper curves*). The straight line identifies on the curves points of equal bolometer resistance and therefore of equal temperature. The difference in the electrical power in the two points provides an estimate of the background. The calculation was done using both the old (*top diagram*) and the new array (*bottom diagram*). The background level is estimated in the worst case, i.e. for a background temperature of 300 K.

of bolometer impedance at known temperatures. A best fit is made to this set of measurements using the functional form 2.58 to derive R_0 and Δ. The evaluation of R must be made in the limit $V_{bias} \rightarrow 0$ V to prevent heating the bolometer above the

known temperature of the bath. Particular care must be taken to remove the offsets in

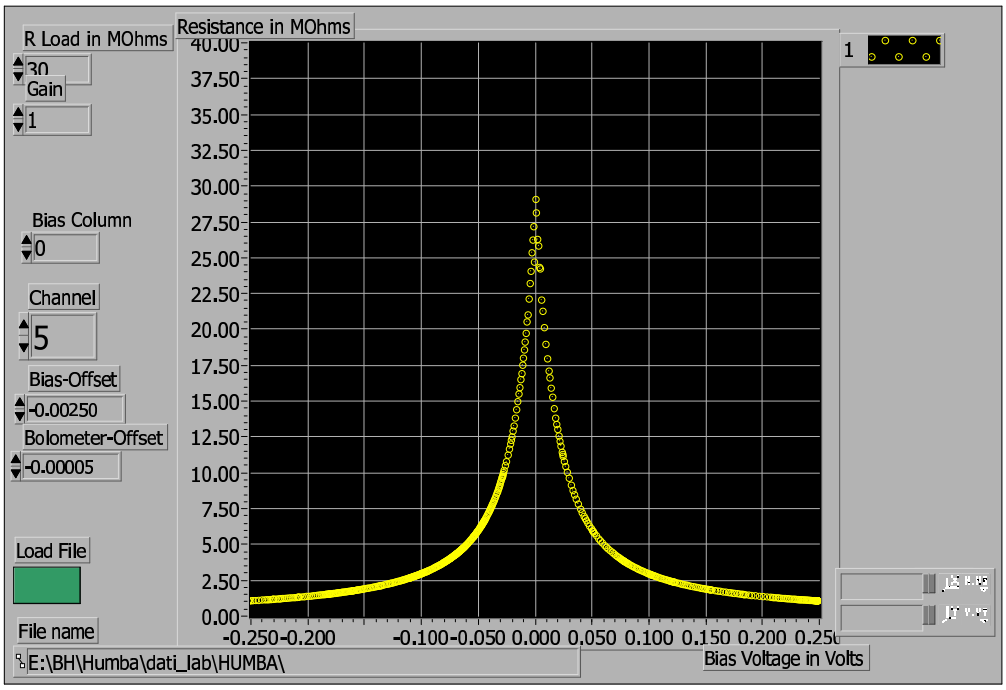

Figure 4.16: Resistance of the bolometer in MΩ vs bias voltage in volts. The rapid decrease of the resistance with increasing bias voltage is due to ohmic heating. The zero bias impedance is estimated as extrapolation from small values of the bias voltage.

the bias voltage, $V_{\mathrm{offset-bias}}$, and in the bolometer signal, $V_{\mathrm{offset-bolo}}$, when calculating

$$R = \frac{R_L(V_{\mathrm{bolo}} - V_{\mathrm{offset-bolo}})}{(V_{\mathrm{bias}} - V_{\mathrm{offset-bias}}) - (V_{\mathrm{bolo}} - V_{\mathrm{offset-bolo}})}$$

and

$$I = \frac{(V_{\mathrm{bolo}} - V_{\mathrm{offset-bolo}})}{R}$$

because of the very small numbers involved. The load resistance, R_{L}, is in our case 30 MΩ. The measured values of the zero bias impedances are very well fitted by a straight line in a $\log R$ vs. $1/\sqrt{T}$ diagram (Fig 4.17). The corresponding values of R_0 and Δ are reported in Table 4.1. It is worth noting that the measured values of zero-bias impedances are systematically higher than the resistance expected from NTD-19 Ge chips at these temperatures, although the agreement with the variable range hopping conduction law (Eq. 2.58) remains very good. This effect is probably generated by the stress induced by the glue on one side of the chips, which causes the parameter Δ to be higher than the value of about 16 K expected for the actual doping level.
At a given bolometer impedance R, the bolometer temperature is

$$T = \left(\frac{1}{\sqrt{\Delta}} \ln \frac{R}{R_0}\right)^{-2} . \tag{4.3}$$

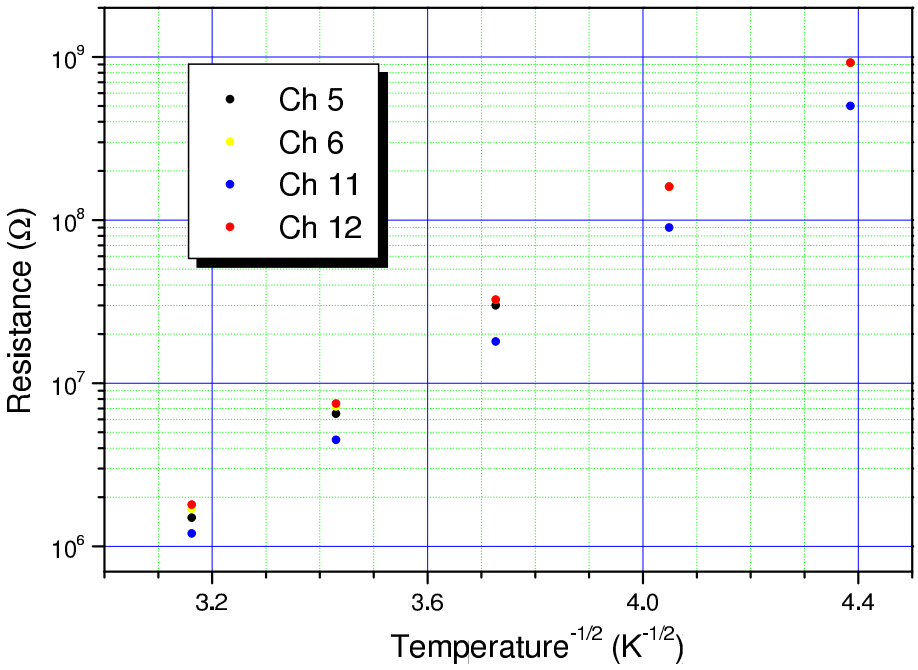

Figure 4.17: Bolometer zero bias resistance as function of the temperature. All samples agree very well with the theoretical behaviour described by the Mott's law, which is described by a straight line in a log vs. $1/\sqrt{T}$ diagram. Three of the samples have similar values of R(T). The different sample was probably bonded less tightly and therefore shows less effect of stress.

Channel	R_0 (Ω)	Δ (K)
5	0.122	26.89
6	0.205	25.65
11	0.189	24.41
12	0.239	25.20

Table 4.1: Calculated values of R_0 and Δ for the four samples.

Alternatively, since R_0 has large uncertainity, one can use $R^* = R(V = 0, T^*)$, being the zero-bias impedance measured at the temperature T^*, and then

$$T = \left(\frac{1}{\sqrt{\Delta}} \ln \frac{R}{R^*} + \frac{1}{\sqrt{T^*}} \right)^{-2} . \tag{4.4}$$

Deriving G. At a base temperature of 52 mK, one of the samples of this test array operated at a bolometer impedance of about 1.6 MΩ, corresponding to a bolometer temperature of 95 mK. From Eq. 4.1 we derived an average thermal conductance of about $1.4 \cdot 10^{-9}$ W/K. For comparison, the same calculation made for the old array with brass wires (Fig. 4.5b) gave a value a factor two higher. A number of approximations were required to calculate these values. For example, the electric field effect (Grannan

et al., 1992) was not taken into account and so the results might be underestimated and are only indicative for the real thermal conductance.
To compare the value derived for G with the theoretical prediction, we recall that the thin films of niobium, which provide the electrical connections to the bolometer, make a negligible contribution to the thermal conductance as the temperature is well below the superconducting transition temperature of the element (9.25 K). Therefore, the thermal connection is entirely provided by the silicon nitride membrane. In amorphous materials, such as low stress Si_3N_4 membranes, the phonon mean free path $\ell_{\rm eff}$ increases with decreasing temperature. At sufficiently low temperatures, $\ell_{\rm eff}$ can exceed the sample dimensions and then phonon surface scattering becomes important. A model analogous to radiative transfer between two blackbodies has been used to describe the thermal transport in the surface-scattering limit in crystalline dielectric samples with a thickness of a few millimeters (Klitsner & Pohl, 1987) to a few microns (Downey et al., 1984). Following Holmes et al. (1998) (hereafter H98), the thermal conductance can be written:

$$G = 4\sigma A T^3 \xi \tag{4.5}$$

where A is the cross sectional area of the membrane perpendicular to the direction of heat flow and $\sigma = \sum_i (\pi^5 k_{\rm B}^4 / 15 h^3 v_{\rm i}^2) = 15.7$ mW cm^{-2} K^{-4} is the Stefan Boltzmann constant obtained by summing over the two transverse and one longitudinal acoustic modes which have sound speeds $v_{\rm i}$. The numerical factor $\xi < 1$ gives the reduction in G due to diffuse surface scattering. An upper limit to G is obtained for the case of specular surface scattering where $\xi = 1$. A lower limit (Casimir, 1938) exists for complete diffuse surface scattering, and provides a value of G about two orders of magnitude lower. The ideal specular surface scattering can be compromised by the quality of the surface and its contamination. The value of thermal conductance that we derived is compatible with the theoretical prediction from Eq. 4.5 with $\xi = 0.26$. H98 find good agreement with the ideal specular reflection limit, starting at a temperature below 90 mK. The discrepancy between our measurement, requiring $\xi = 0.26$, and H98 finding $\xi = 1$ can be due to the larger width of our membranes (a factor 30 compared with those of H98), which can result in a residual diffuse phonon scattering. An additional source of discrepancy may come from the approximations mentioned earlier. For the old array, the surface contamination was large and so the contribution of the membrane to the thermal conductance was probably negligible, and the thermal transport properties were determined by the brass wires.

For the estimated background power, a bolometer temperature 1.3 times the bath temperature, and the desired bolometer impedance at which the current and voltage noise are minimum, the optimum thermal conductance is close to the value measured in the old array with brass wires. We therefore decided to upgrade that array to 19 channels for the tests at the telescope. However, the technology used in the new array results in more uniformity of performance among the detectors and an easier optimization of the sensitivity.

Chapter 5

First Runs at the 30 m Telescope

During late 2001 HUMBA has been installed and tested at the IRAM 30 m telescope (MRT). The telescope is located at 2900 m above sea level at Pico Veleta, in the Sierra Nevada (Spain). The diameter of the primary mirror, its surface accuracy (50 μm), together with the atmospheric conditions of the site, make of the MRT a unique telescope for mm and sub-mm astronomy.
HUMBA was first installed at the MRT during September 28 - October 8, 2001. A temperature instability was discovered and traced down to a thermal short between the 0.7 K shield and the 4.2 K shield, which was caused by a screw that vibrated loose during transport. When the problem was fixed and the system was cold again, high winds prevented a proper alignment using the platform in front of the subreflector. Standard tests on the sky were nevertheless performed and the goal of having HUMBA installed and operational at the 30 m was in principle achieved. To test HUMBA on weak sources, for which a proper alignment is required, we made a second run during November 23-30, 2001. In this and in the following chapter we report about the installation and observations during this second test period.

5.1 Installation

HUMBA was located in the front, right-hand corner of the receiver cabin. Due to its weight (150 kg for the cryostat, plus 100 kg of the gas handling rack) and to the complexity of the cryogenics, HUMBA had to be mounted in its final position in the receiver cabin before starting precooling with liquid nitrogen. The cryostat leans on a platform, supported by arms attached to the wall. Mechanical decoupling is provided by four shock absorbers between the cryostat and the platform. The installation on the support structure is complicated, because of the lack of a crane in the bolometer area of the cabin.

5.1.1 Cryogenics

About four days are necessary for the installation, evacuation of the cryostat, precooling with liquid nitrogen, helium transfer and start of the dilution process. Because of the lower atmospheric pressure at the MRT, the boiling points of liquid nitrogen and liquid

helium were lower than the normal 77 K and 4.2 K during laboratory experiments. This affected the circulation of ^{3}He in the dilution unit. The composition of the mixture had to be tuned to reach the desired operating temperature of 60 mK and to obtain a good temperature stability.

5.1.2 Optics

The beam coming from the telescope was reflected by the Nasmyth mirror M3 (Fig. 5.1) to the mirror M4 and then directed downward and rightward again, respectively by mirrors M5 and M6. A system of two HDPE lenses adapted the beam of the telescope

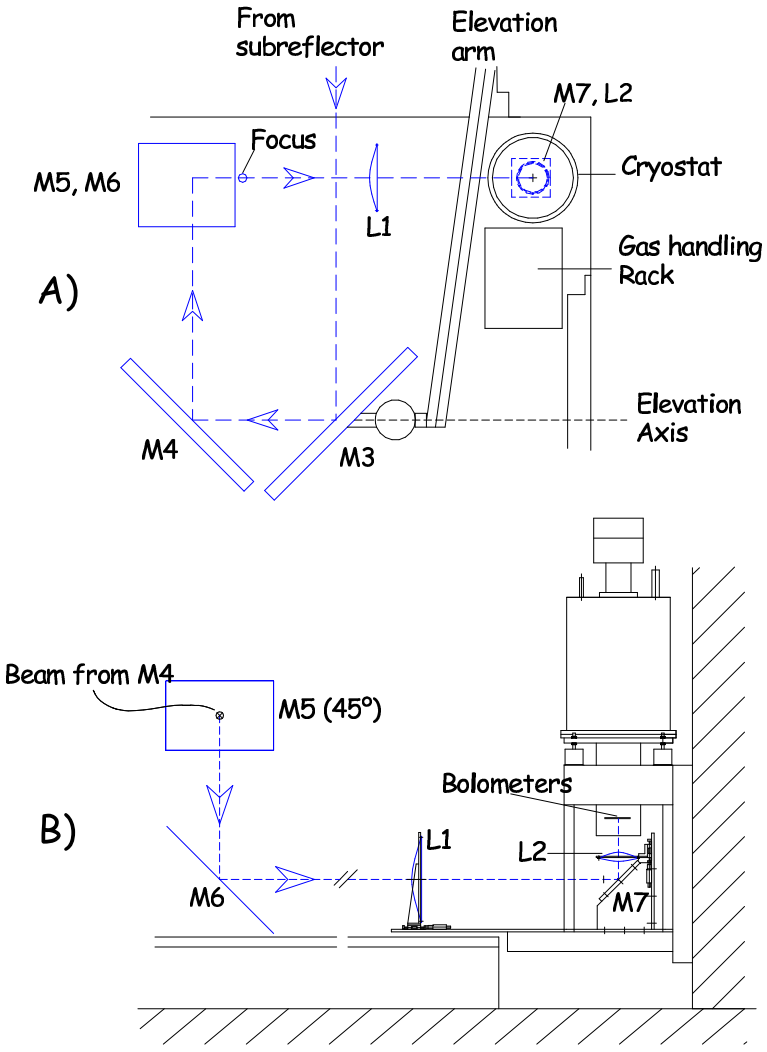

Figure 5.1: (A)Top and (B) side views of the optical system of the bolometer corner inside the MRT receiver cabin. Optical elements are in blue. The arrows indicate the direction of propagation of the beam.

to the horns of HUMBA, and a further mirror M7 fed the beam through the window

of the cryostat which faced downward. The lenses and the mirror M7 that was placed between them were mounted on a plate attached to the same support structure as the cryostat.
A proper optical alignment of the system requires the following steps:

- identification of the elevation axis and position of the center of the beam,
- alignment of the lens system with the center of the beam,
- centering of the central channel of the bolometer array on the subreflector.

The telescope is equipped with a laser installed on the elevation axis such that its beam is colinear with it. Removing the Nasmyth mirror M3 and mounting a double-beam laser between M3 and M4 it was possible to align this second laser with the first. Once the Nasmyth mirror was placed back in position, the spots that the double-beam laser projected on M3 and M4 could be marked for future reference, and the double-beam laser could be used to identify the correct position of the beam propagating after the M5 and M6 mirrors. During the second run at the telescope it was not possible to use the laser on the elevation axis. Assuming that the axis of the Nasmyth mirror coincides with the elevation axis, the latter could be identified experimentally, without having to remove the Nasmyth mirror, by adjusting the position of the double-beam laser until the projected spot on the center of the subreflector did not move with a change in the elevation.
The cryostat was shifted vertically to the theoretical distance from the beam axis, after reflection off M5 and M6. The beam axis vas visible as the laser spot projected on the wall below the support structure of HUMBA. To align the lens system with the beam, two transparent plexiglas plates with a small hole in the center were mounted in the frames in place of the lenses. The position of the support plate was then adjusted until the laser propagated though both holes. The cryostat window was approximately centered on the laser beam. The position of the frames along the beam was adjusted according to the optical design specifications and the plexiglas plates were replaced with the lenses.
With the telescope in stow position pointing to the horizon, it is possible to raise a platform in front of the subreflector. The use of this platform allows one to move a modulated source across the subreflector. The central channel of the bolometer array is centered on the subreflector by observing with HUMBA this modulated source in different positions symmetrical with respect to the center. The cryostat is shifted on its support until a good symmetry for the signals on the outer ring of bolometers is reached.

5.2 Tests on the Sky

Thanks to very good weather conditions, HUMBA could observe on the sky for the entire remaining available time, i.e. from November 28th until the morning of November 30th. Atmospheric opacity measured with skydips was very low, ranging between 0.07 and 0.11 (Fig. 5.2). We demonstrated that the traditional pointing, focus, on-off and

on-the-fly mapping modes using the wobbler as well as total power skydips and fast-scanning (Reichertz et al., 2001b) maps functioned with HUMBA.

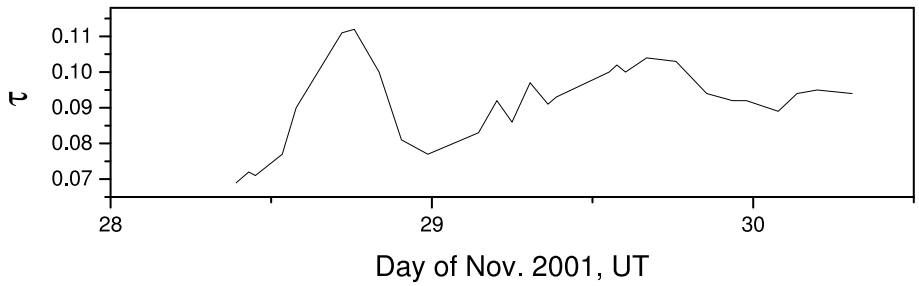

Figure 5.2: Variation of the zenith atmospheric opacity during the two days of observations. The difference in the opacity correction between the best and the worst condition is less than 5%.

5.2.1 Determination of Beam Parameters

Beam Profile

The telescope beamwidth can be estimated with pointing scans or maps. The FWHM of a cross scan is the convolution of the real beam with the source shape, therefore it is necessary to use point-like extragalactic sources for a correct beamwidth determination. For planets, whose size may be comparable with the size of the beam, it is possible to deconvolve the real beam under the assumption that the planet emission is well approximated by that of a uniform disk (Baars, 1973). From pointing scans across 1055+018 (Fig. 5.3) and a map of 3C 279 (Fig. 5.4) we measured an average beam of about 19" FWHM, in good agreement with the value expected for diffraction-limited conditions at the HUMBA wavelength. The same value was found using Uranus, whose size is small enough to make the error on the beam negligible, and Mars, after deconvolving the effect of the angular size of about 7".

Array Parameters

Mapping a point-like source allows one to determine the relative azimuth and elevation offsets of the 19 beams, as well as the relative sensitivity of the different bolometers. The result on Uranus are shown in Fig. 5.5 and in Fig. 5.6, respectively before and after the gain correction. Despite the efforts in the optical alignment, some of the outer pixels received less signal from the source than the others. The reason was not understood and needs further investigation. The difference remains even if the different intrinsic bolometer sensitivities measured in the laboratory is taken into account. For this reason, the problem is most likely in the optical system, but it is unclear whether it arises from inside (filters) or outside the cryostat (lenses). The peculiar pattern of the beam map seems to indicate that the sensitivity loss is possibly due to diffraction on more than one plane.

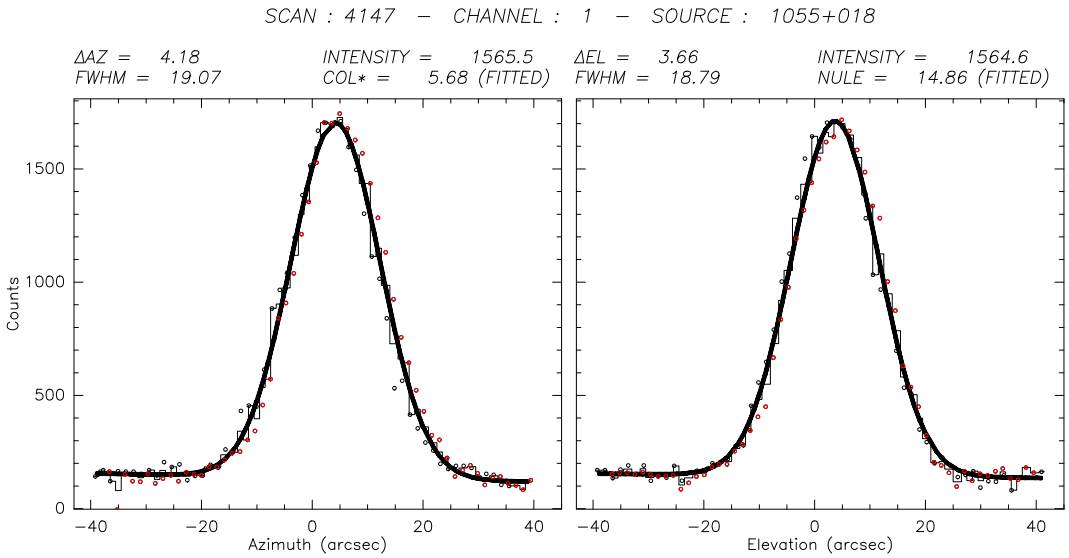

Figure 5.3: Pointing scans across 1055+018. The calculated beam FWHM is about 19".

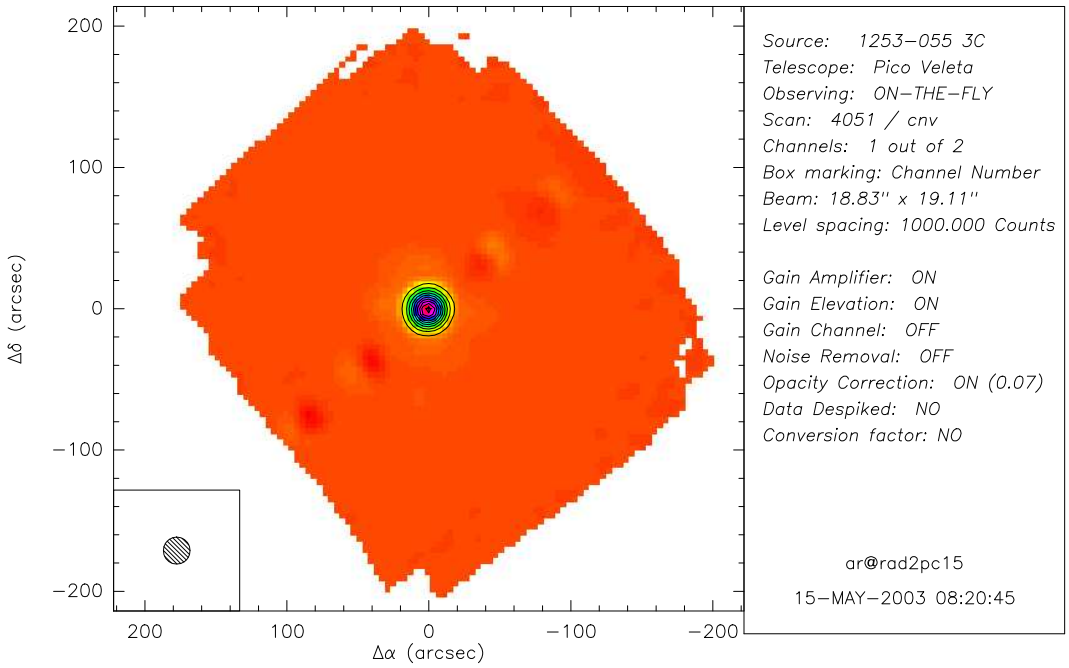

Figure 5.4: OTF map of 3C 279. The derived beam FWHM is about 19".

5.3 Calibration on Planets

To calibrate bolometer observations one needs to compare them with the measurement of a source with a well-known flux. The best calibrators are some of the planets (Mars, Uranus, Neptune), although there exist factors that can alter the precision with which their brightness temperatures are known. During the campaign in November 2001, on-off observations were performed on Mars, Saturn, Uranus, and Neptune. We give

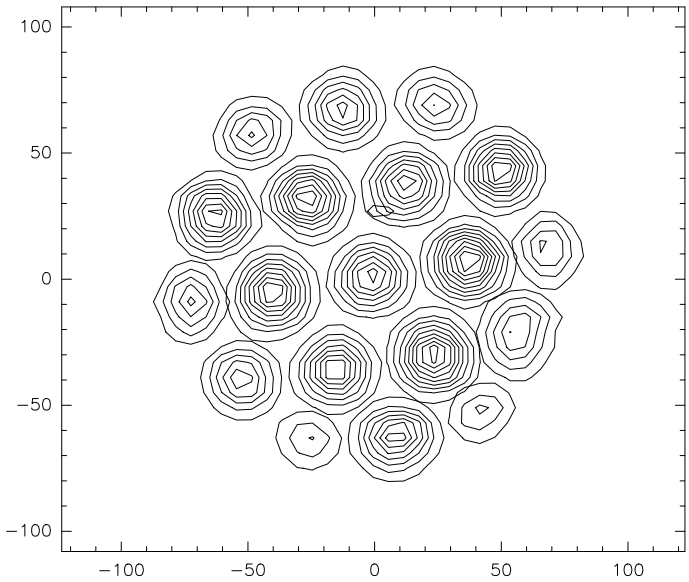

Figure 5.5: Beam mapping on Uranus at 37° of elevation. The sensitivity of the outer pixels is decreased due to a possible problem with the optics.

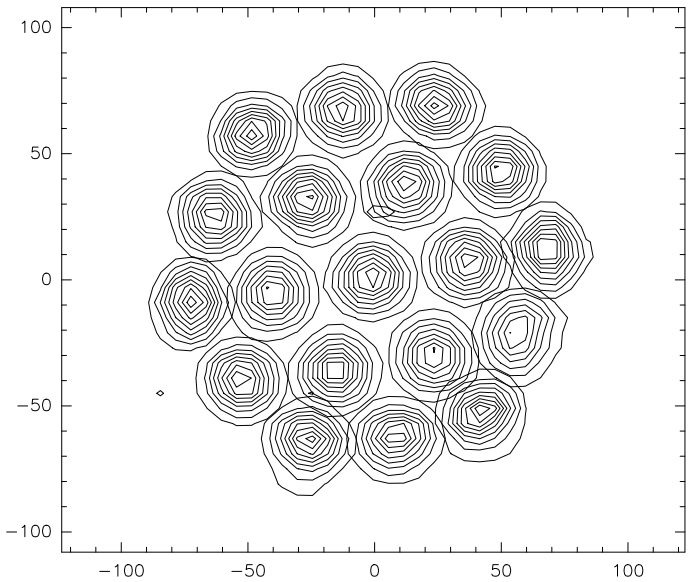

Figure 5.6: Beam mapping on Uranus after applying a correction to the bolometer gains measured on Uranus itself.

here short remarks about the quality of these planets as calibrators.

- **Mars**
  It is one of the two most important primary calibrators. Its diameter varies between 3" and 25". Measurements indicate that Mars is nearly a blackbody in the millimeter and submillimeter region because of its solid surface and tenuous atmosphere (Griffin et al., 1986), but dust storms might influence its brightness

temperature. Due to the pronounced eccenticity of its orbit, its temperature varies with heliocentric distance.

- **Saturn**
  Its diameter varies between 15" and 20", and the oblateness of the disk (ϵ=0.096, Hildebrand et al. 1985) is not negligible. The changing tilt angle of the rings as seen from the Earth leads to a variation of its emission.

- **Uranus**
  It is one of the two most important primary calibrators. Its diameter is ∼3", and its brightness temperatures in the millimeter/submillimeter region are well known.

- **Neptune**
  Its diameter is ∼3". There is a discrepancy between the temperatures presented by Griffin & Orton (1993) and those found by Marten et al. (1993) of several percent.

5.3.1 Effective Frequency

To convert the counts measured with the bolometer to the flux density of a source at a certain frequency, one has to take into account bolometer's broad bandpass (about 24 % in the case of HUMBA). It is useful to define an effective frequency as the frequency at which the monochromatic flux density would be equal to the average flux density observed in the entire bolometer bandpass. Obviously, this effective frequency depends on the spectral shape of the source, as well as on other frequency-dependent parameters such as atmospheric transmission.
The total observed flux density, $S_{\rm tot}$, of a source with spectrum $S(\nu)$ is:

$$S_{\rm tot} = \int_{\nu_1}^{\nu_2} S(\nu)A(\nu)T(\nu)d\nu \tag{5.1}$$

where $A(\nu)$ is the atmospheric transmission, $T(\nu)$ is the spectral response of the instrument with ν_1 and ν_2 being the lower and upper frequency limits. The average flux density, $\langle S\rangle$, observed in the bandpass is therefore:

$$\langle S\rangle = \frac{S_{\rm tot}}{\int_{\nu_1}^{\nu_2} A(\nu)T(\nu)d\nu} = \frac{\int_{\nu_1}^{\nu_2} S(\nu)A(\nu)T(\nu)\,d\nu}{\int_{\nu_1}^{\nu_2} A(\nu)T(\nu)d\nu}\ . \tag{5.2}$$

The effective frequency, $\nu_{\rm eff}$, is defined such that:

$$S(\nu_{\rm eff}) = \langle S\rangle\ . \tag{5.3}$$

For a planet, the spectrum in the millimeter regime can be described by the Rayleigh-Jeans approximation:

$$S(\nu) \propto \nu^2\ . \tag{5.4}$$

Together with equations 5.3 and 5.2 this yelds

$$\nu_{\mathrm{eff,pla}} = \sqrt{\frac{\int_{\nu_1}^{\nu_2} \nu^2 A(\nu) T(\nu) d\nu}{\int_{\nu_1}^{\nu_2} A(\nu) T(\nu) d\nu}} \; . \tag{5.5}$$

During the two days of observations the weather conditions were stable and good, with an atmospheric water content between 1.0 and 1.6 mm; we can therefore neglect the atmospheric transmission term in Eq. 5.5. After numerical integration, using the spectral response presented in Fig. 4.2, we obtained an effective frequency for the calibration on planets of

$$\nu_{\mathrm{eff,pla}} = 144.6 \text{ GHz} \; . \tag{5.6}$$

5.3.2 Conversion Factor

The four planets observed with HUMBA during the campaign in November were visible at the MRT from the afternoon through to the evening (Fig. 5.7). Three of them (Mars, Uranus and Neptune) were observed at similar elevations, between 31° and 37°. The flux densities per beam for our 19" beam, calculated using the sofware ASTRO (GILDAS working group, 1998), range between 5.84 Jy beam^{-1} of Neptune and 461.44 Jy beam^{-1} of Saturn. The planets data are summarized in table 5.1.

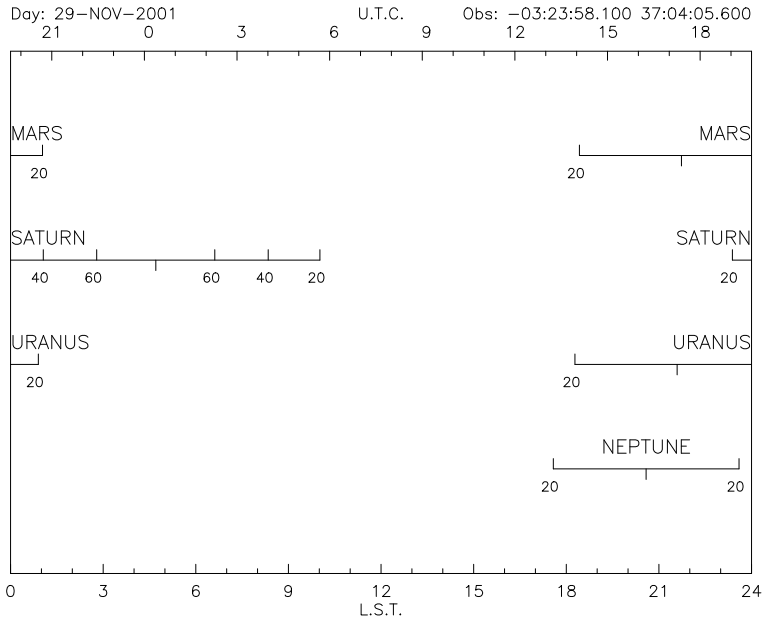

Figure 5.7: Chart of observability of Mars, Saturn, Uranus, and Neptune, during the last days of November 2001 at the MRT.

The angular diameter of Saturn was larger than the beam of HUMBA. This, combined with its oblateness and the presence of the rings makes Saturn unreliable for calibration. Because of the discrepancies in the brightness temperature of Neptune

Planet	Mean Diameter (")	Flux density per beam† (Jy beam^{-1})	Day and UT of observation	Elevation (°)
Uranus	3.41	15.27	28-11 17:12	37.91
			28-11 18:07	36.66
		15.25	29-11 15:52	34.41
			29-11 15:59	35.00
Saturn	19.57	461.44	29-11 00:13	73.14
			29-11 01:02	71.35
			29-11 01:25	68.74
Neptune	2.16	5.84	29-11 15:03	31.96
			29-11 15:07	32.25
			29-11 15:15	32.74
Mars	7.40	130.50	29-11 16:16	35.59

Table 5.1: Mean angular size and flux density of the observed planets and time and elevation of observation.† at 146.6 GHz, calculated using ASTRO (GILDAS working group, 1998).

reported in the literature (Section 5.3), and the availability and good agreement of both main calibrators, Mars and Uranus, we decided to calculate the conversion factor between counts and jansky based on them and to exclude Neptune. A comparison among the planet flux densities, normalized by their nominal values, shows that the flux densities of Saturn and Neptune are probably underestimated (Fig. 5.8). The uncertainty on brightness temperature of planets is generally of the order of 5%. This value must be added to the relative error of our measurement to obtain the total uncertainty on our calibration. The conversion factor used is 408 ± 29 counts/Jy.

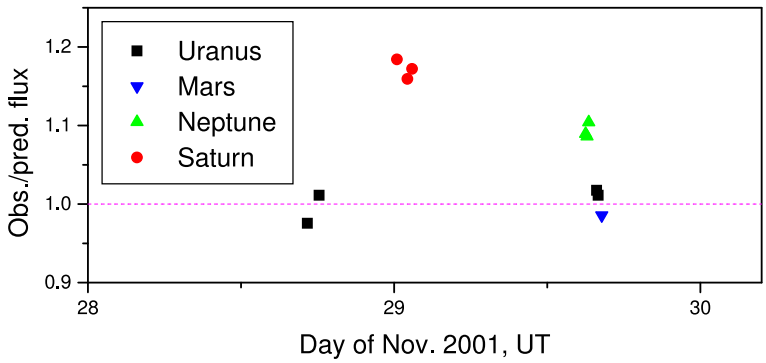

Figure 5.8: Observed/predicted flux density of planets during the two days of observation. The conversion factor of 408 counts/Jy was calculated using only the main calibrators, i.e. Mars and Uranus.

5.3.3 Sensitivity

Dividing the conversion factor by the noise level in counts $\sqrt{\text{s}}$, we calculated a sensitivity of 34 mJy $\sqrt{\text{s}}$ per beam for the central channel and 22 mJy $\sqrt{\text{s}}$ per beam for the best one. This value shows that in principle it is possible, with the current technology, to improve the sensitivity by at least 60 %. The scatter in the sensitivity among different pixels in the array will possibly be improved by using photolithographed wires for the bolometers instead of the brass wires that were used in the current array.

Assuming that the new array will have a sensitivity equal to that of the best channel in this campaign, we can estimate the time, t, required to produce high-resolution and low noise level maps:

$$t = \left(\frac{\text{Sensitivity}}{\text{Desired r.m.s.}} \right)^2 \cdot \frac{1}{\text{number of pixels}} \cdot \frac{\text{Map size}}{\text{Beam size}} , \tag{5.7}$$

where

$$\text{Map size} = \text{Map size (az)} \times \text{Map size (el)}$$

and

$$\begin{aligned} \text{Map size (az)} &= \text{Source size (az)} + \text{Array size} + \text{Wobbler throw} \\ \text{Map size (el)} &= \text{Source size (az)} + \text{Array size} . \end{aligned}$$

HUMBA could produce an image of $3' \times 3'$ with a 1 σ noise level of 0.3 mJy per beam in about 30 hours of integration. This expected capability of HUMBA can be compared to the performance of other existing bolometer cameras at 2 mm. Pointecouteau et al. (1999) presented a $2' \times 1'$ map of the cluster RXC J1347-1145 with a resolution of $25''$ and a 1 σ noise level of 1 mJy beam^{-1}, which was obtained in about 20 hours of integration at the MRT. In the same time, HUMBA could produce an image $4' \times 4'$ of the same cluster with a noise level of 0.4 mJy and a somewhat better resolution. The same cluster has been observed also with NOBA, the bolometer camera at the Nobeyama telescope, in Japan. Komatsu et al. (2001) reported a $1'.9 \times 1'.9$ image with a beam-size of $20''.6$ and a noise level of 1.3 mJy beam^{-1}. The same image could be produced by HUMBA in 3.6 ks, compared to the 81.2 ks of integration that were necessary with NOBA.

Chapter 6

First Scientific Results

We report here on the results of the two days of observations made during the second campaign at the IRAM 30 m telescope during Nov. 2001. The main goal was to test the capability of HUMBA to detect faint sources and to make preliminary observations of the SZ effect in clusters of galaxies. We observed three compact clusters selected from the NORAS catalogue (Böhringer et al., 2000) for having high X-ray luminosity. The results of these observations are discussed in Sec. 6.2 together with a comparison with existing X-ray data.
Comet C/2000 WM1 (LINEAR) had its closest approach to the Earth, at a geocentric distance of 0.32 AU at the end of Nov. 2001. We measured the strength of its emission which is determined by mm-size ice and dust particle.
A short integration was made on Pluto, yielding a significant detection. As far as we know, this is the first observation of this planet at 2 mm.
A few selected low-flux-density stellar objects were also observed, and the results are compared with the flux density extrapolated from other frequencies, using the spectral-index estimates that are available in the literature.
We measured the 2 mm flux density of some of the astronomical objects that are normally used as secondary calibrators. These data can be useful for future reference. Observations of few a other known Galactic and extra-Galactic objects are also presented. Table 6.1 shows the list of observed sources, divided into extra galactic, Galactic, and Solar System objects.

6.1 Data Reduction

Data acquired from HUMBA were stamped with the exact time of observation using software from IRAM (the merger) that merges instrument data with the telescope data after observing. After analysing the observations, the IRAM staff communicated the existence of a problem with the merger, the software that merges the data acquired from the instrument with the telescope data, and supplied a corrected version of the software. We re-merged and re-reduced our data.

Two software packages are available for reducing data from observations with bolometers: *NIC*, written at MPIfR and IRAM/Grenoble (Broguiére et al., 1995), and *MOPSI*, written by Robert Zylka (Zylka, 1998). *NIC* is in general simpler to use

EXTRA GALACTIC SOURCES				
source	alternate name	type	R.A. (J2000)	Decl. (J2000)
1226+023	3C 273	QSO	12 29 06.698	+02 03 08.58
1253-055	3C 279	QSO	12 56 11.1665	-05 47 21.523
1334-127		BL Lac	13 37 39.7828	-12 57 24.6932
1413+135		BL Lac	14 15 58.8175	+13 20 23.7126
1510-089		QSO	15 12 50.533	-09 05 58.99
RXC 1023.6+0411	Zw 3146	Galaxy Cluster	10 23 38.808[(1)]	+04 11 11.4[(1)]
RXC 1401.0+0252	A1835	Galaxy Cluster	14 01 02.28[(1)]	+02 52 48.36[(1)]
RXC 2228.6+2036		Galaxy Cluster	22 28 37.104[(1)]	+20 36 31.32[(1)]
GALACTIC SOURCES				
source	alternate name	type	R.A. (J2000)	Decl. (J2000)
α Aur		Stellar disk	05 16 41.36	+42 59 52.8768
α Ori	Betelgeuse	Stellar disk	05 55 10.2737	+07 24 25.393
Ceph A		Massive Star Forming region	22 56 17.8735	+62 01 49.793
G45.1		Massive Star Forming region	19 13 22.0201	+10 50 53.392
GL 490		Star Forming region	03 27 38.8342	+58 47 00.719
HH12-1		Pre main seq. star	05 36 22.85214	-06 46 06.5536
HL Tau		Pre main seq. star	04 31 38.4437	+18 13 57.978
K3-50A		Massive Star Forming region	20 01 45.6374	+33 32 43.548
NGC 7538		Massive Star Forming region	23 13 45.3318	+61 28 10.572
ρ Per		Stellar disk	03 05 10.5934	+38 50 24.986
T Tau		Pre main seq. star	04 21 59.45877	+19 32 06.2014
W3(0H)		Massive Star Forming region	02 27 03.8653	+61 52 24.829
SOLAR SYSTEM OBJECTS				
source		type		
Pluto		Planet		
C/2000 WM1		Comet		
Ceres		Asteroid		

Table 6.1: List of observed sources. [(1)]From the NORAS catalogue (Böhringer et al., 2000).

and better documented than *MOPSI*, but is less flexible, especially for the subtraction of the correlated noise. With *MOPSI* it is possible to remove the correlated noise in the different pixels on the single phases of an on-off observation, i.e. before subtracting the off-source measurement from the on-source measurement. This improves the final signal to noise ratio and has a great advantage especially for the reduction of observations of faint sources.
We initially used *NIC* but, for weak sorces, we could test different reduction strategies with *MOPSI* and therefore obtained better results. Cosmic rays and electric interference may produce spikes in the acquired signal. These have a characteristic feature on very short time scale, and thus can be identified and removed. After despiking, atmospheric opacity correction was applied and the signal was converted from counts to Jy using the conversion factor calculated in Sec. 5.3.2 from observation of planets.

6.2 Galaxy Clusters

For our observations, we selected the three most compact and luminous clusters in the NORAS (Northern *ROSAT* All Sky) galaxy cluster survey (Böhringer et al., 2000). Table 6.2 summarizes their characteristics.

Due to the limited time available at the telescope, it was not possible to map the clusters, and we had to observe in on-off mode. We used a 2 Hz wobbling frequency

cluster	z	$L_{\rm x}$	$r_{\rm c}^{(1)}$	$r_{\rm c}$	β	y_0
RXC J1023.6+0411	0.2850	29.91	0.0	9.3 [(2)]	0.569 ± 0.025 [(2)]	$3.69 \cdot 10^{-4}$ [(2)]
RXC J1401.0+0252	0.2528	32.56	0.5	n.a.	n.a.	n.a.
RXC J2228.6+2036	0.4120	29.62	1.0	18.9 ± 2.3 [(3)]	0.54 ± 0.03 [(3)]	$2.4 \cdot 10^{-4}$ [(3)]

Table 6.2: Properties of the observed clusters. Redshift z, rest frame X-ray luminosity $L_{\rm x}$ of the cluster in the 0.1-2.4 keV energy band, in units of 10^{44} erg s^{-1}, core radius $r_{\rm c}$ ($'$) reported in the NORAS catalogue, and core radius r_c ($''$), β, and central Comptonization parameter, y_0, according to an isothermal β-model when available. [(1)]Best-fitting core radius for the King-model fit; these are only a qualitative measure for the source extent, since the fitting grid was coarsely spaced. [(2)]From Böhringer (2002). [(3)]From Pointecouteau et al. (2002).

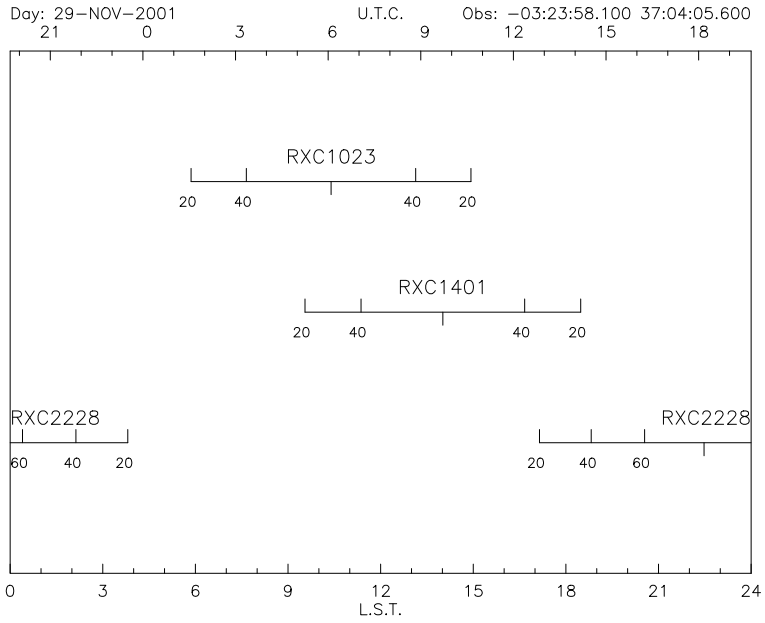

Figure 6.1: Observability chart for the selected clusters.

and the maximum beamthrow that was possible without a significant increase in the mechanical noise, i.e. $100''$. Since the clusters were more extended than the beamthrow, the reference beam (off position) remained within the source. This had some important consequences. First, some fraction of the signal was subtracted away when differencing the measurement, depending on how steeply the cluster emission decreased with the angular distance from the cluster center. Second, since the on-off observation is a combination of wobbling of the secondary mirror and nodding of the telescope, the outer beams of the array measured an average of the signals in three points on the sky at different distances from the center of the cluster. Last, if the observation is slightly off-centered from the cluster, the daily rotation of the sky produces a further asymmetric averaging of the signals in the outer channels. This may easily occur when observing an extended source in on-off mode, and was actually the case for our observations due to the offset between the coordinates that we used (from the

NORAS catalogue) and the optical center of the cluster. We took account of this when calculating the expected Comptonization parameter measured from X-ray data. The results reported in the following paragraphs used only the single central channel of the array.
Attempts to improve the signal to noise ratio using the correlated sky noise subtraction from the single phases failed because the the outer beams did not observe an empty sky but received a fraction of the signal that was present at the cluster center. The correlation was therefore due not only to sky noise but also to the signal itself. To avoid these limitations one would need only to map a region large enough that the outer edges of the map do not contain a signal from the cluster. Furthermore, the map would use data from the whole array and so the integration time required to reach the same level of sensitivity would decrease by a factor equal to the number of pixels, i.e. 19.

6.2.1 RXC J2228.6+2036

This cluster shows an extended and slightly elongated morphology, and is most probably one of the hottest clusters known. It is the most X-ray luminous cluster that does not display the features of a strong cooling flow. A ROSAT-HRI image of the inner region of the cluster is shown in Fig. 6.2. Due to the large extent of this

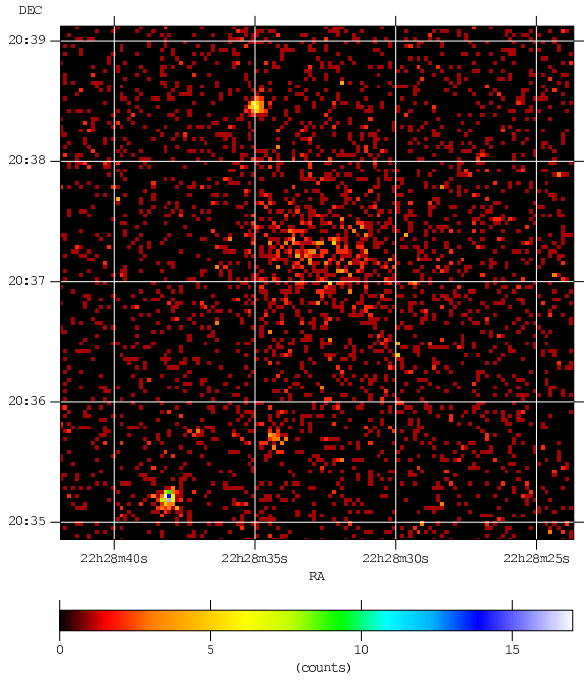

Figure 6.2: ROSAT-HRI image of the inner region of RXCJ 2228.6+2036. From the Heasarc Data Archive.

source, the on-off mode causes a large reduction of signal (35 %), and therefore we

integrated a long time on this object with the hope of obtaining a significant detection. In a total integration time of about 13500 s, we measured -0.84 mJy with a 1 σ random uncertainity of 0.33 mJy estimated from the scatter in the time series of on-off measurement and a 7 % systematic calibration uncertainity. This measurement is at the 2.5 σ level and so is not formally significant. However, it is suggestive, and is worth confirming. The results are presented in Fig. 6.3. The source extent caused the zero level reference calculated on the outer pixel (blue solid line in Fig. 6.3) to be negative, and caused the cumulative dispersion (blue dashed line in Fig. 6.3) to stabilize at a constant value rather than continuing to decrease with increasing integration time. An

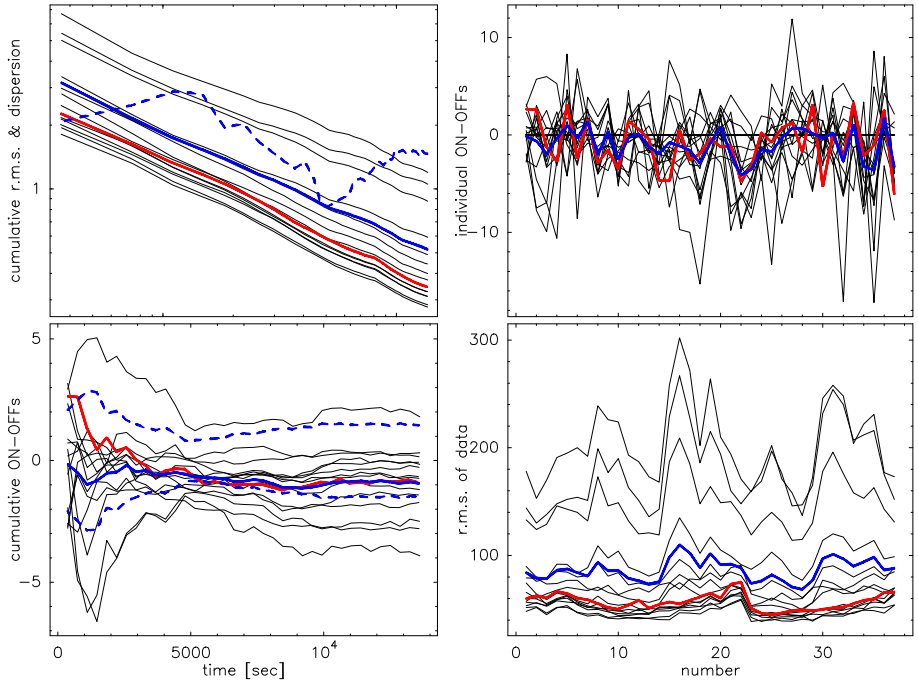

Figure 6.3: Individual and cumulative on-offs and r.m.s. of data for the cluster RXC J2228.6+2036. *Top Left*: shows the standard error of the mean of the on-off differences for each channel, shown as a function of accumulated time during the observation. Red is for the central channel. Blue solid line is for the average of the outer pixels. Black lines are for the outer channels. *Bottom Left*: shows the average of the on-off differences for each channel as a function of the time interval from the start of the observation included in the average. A significant detection of signal in the central channel would appear as a departure of the red line from zero by more than 3× the r.m.s. indicated by the red line in the plot at top left. *Top Right & Bottom Right*: show the difference signal and r.m.s. of the individual on-off scans.

upper limit to the Comptonization parameter, y, can be calculated using Eq. 1.5, which we recall here for convenience:

$$\Delta I = y f(x) I_0 \,. \tag{6.1}$$

The numerical value of I_0 is given in Eq. 1.6. The function $f(x)$ (Eqs 1.7, 1.8, 1.9) must be evaluated at the effective frequency of observation, which is implicitly defined

by Eq. 5.3, and can be calculated in a way anologous to Eq. 5.5:

$$f(\nu_{\mathrm{eff,SZ}}) = \frac{\int_{\nu_1}^{\nu_2} f(\nu)T(\nu)d\nu}{\int_{\nu_1}^{\nu_2} T(\nu)d\nu} \tag{6.2}$$

where the spectral response of the instrument $T(\nu)$ is presented in Fig. 4.2. Numerical solution of Eq. 6.2 yields a value of $f(x) = -3.89$ for an effective frequency $\nu_{\mathrm{eff,SZ}} = 147.8$ GHz.
To be used in Eq. 6.1, our flux-density limit must be referred to unitary solid angle (or alternatively, I_0 must be calculated for the solid angle corresponding to our beam). The *flat-top* solid angle, Ω, can be estimated for a beam with a Gaussian profile with:

$$\Omega \simeq 1.133 \cdot (FWHM)^2 = 9.6 \cdot 10^{-9} \text{ sr} . \tag{6.3}$$

We obtain a 3 σ upper limit of:

$$y_{\mathrm{obs}} < 1 \cdot 10^{-4} .$$

We can now compare this result with the value predicted according to the isothermal β-model. The Comptonization parameter has the same profile as the SZ intensity (Eq. 1.18), and therefore can be expressed as:

$$y(r) = y_0 \cdot \left[1 + \left(\frac{r}{r_c}\right)^2\right]^{-\frac{3\beta}{2}+\frac{1}{2}} . \tag{6.4}$$

The y profile for this cluster is plotted in Fig. 6.4, using the parameters reported in Table 6.2. To compare with our observation, the profile from Eq. 6.4 must be convolved with the beam, and the value corresponding to the reference (off) position must be subtracted. After a numerical integration, we obtain $y = 1.4 \cdot 10^{-4}$, which is slightly larger than the measured upper limit. We do not consider this a serious disagreement since there are uncertainities in the adopted model.

This massive and luminous cluster is an ideal candidate to study the IC plasma. It has been observed with the Nobeyama 45 m radio telescope at 21 GHz and with ROSAT/HRI (Pointecouteau et al., 2002). Higher resolution images are required to obtain an accurate picture of the density and temperature of the IC medium. We proposed 30 ks observation with XMM-Newton (Böringer et al., 2003) and we plan to image this cluster with HUMBA during the next campaign at the MRT.

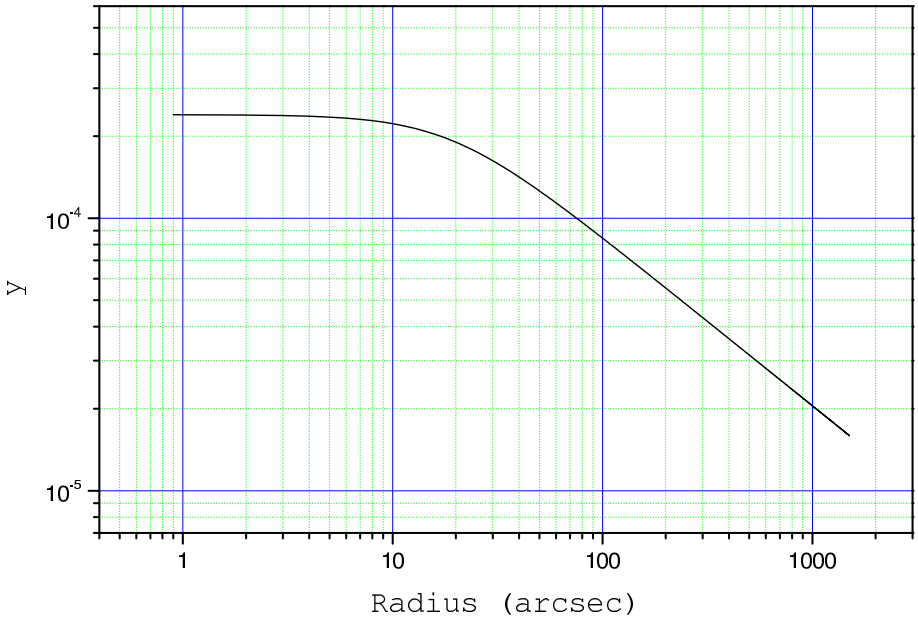

Figure 6.4: Comptonization parameter profile, according to the isothermal β-model, as a function of the radius from the center for the cluster RXC J2228.6+2036.

6.2.2 RXC J1023.6+0411

The X-ray data of RXC J1023.6+0411 show that the cluster contains the most massive known cooling flow (Edge et al., 1994). The highly peaked X-ray emission in the core of the cluster is visible in Fig. 6.5. Results from the bolometer observations are

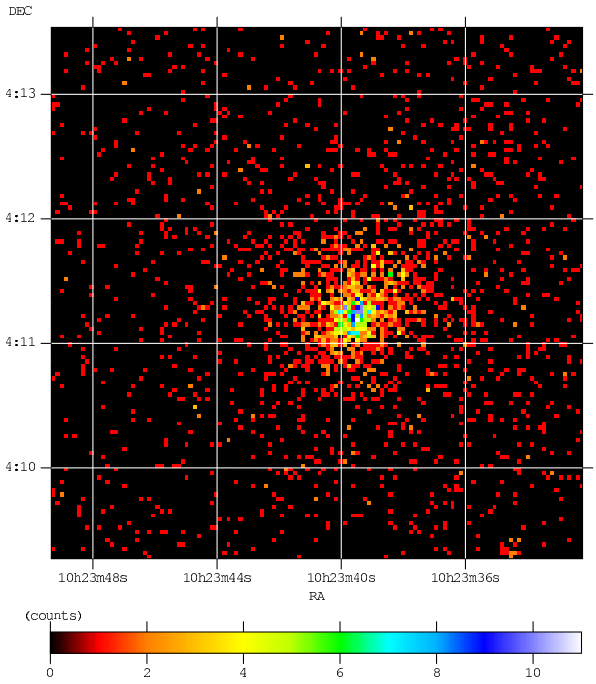

Figure 6.5: ROSAT-HRI image of the inner region of RXC J1023.6+0411. From the Heasarc Data Archive.

presented in Fig. 6.6. Again, we note that the reference zero-level is negative, and that the cumulative dispersion stabilizes at a constant value instead of decreasing with increasing integration time. We integrated on this cluster for 10500 s and detected a SZ decrement of -1.55 mJy, with a 1 σ random uncertainity of 0.33 mJy and a 7 % systematic uncertainity. This corresponds to a Comptonization parameter $y = (1.5 \pm 0.4) \cdot 10^{-4}$. The angular offset between the center of our observations and the coordinates of the optical center of the cluster was in this case comparable with the beam. We have to take account of this when comparing with the predicted value of the Comptonization parameter.

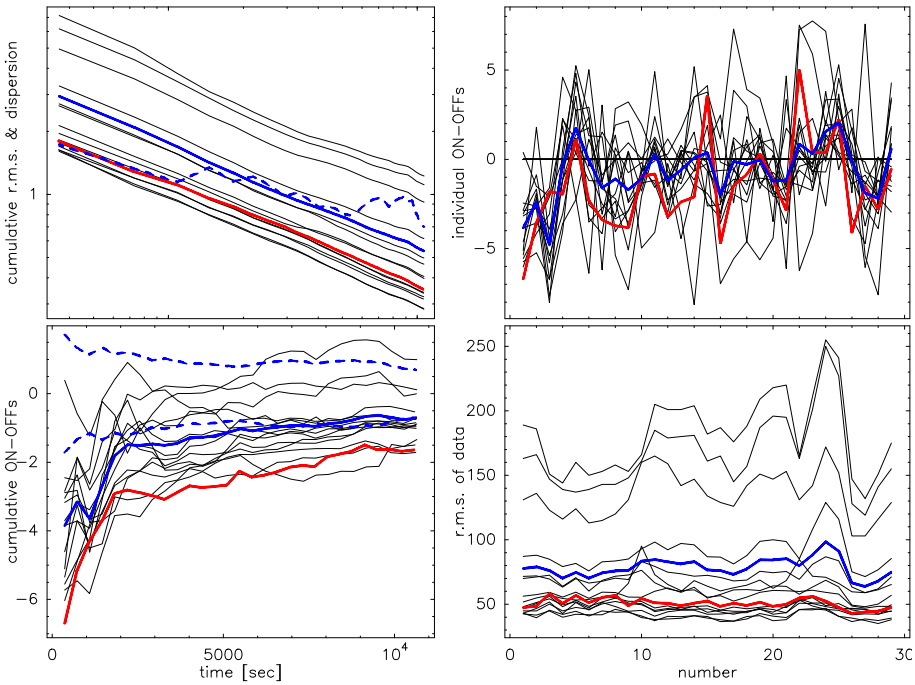

Figure 6.6: Same as Fig. 6.3 for the cluster RXC J1023.6+0411.

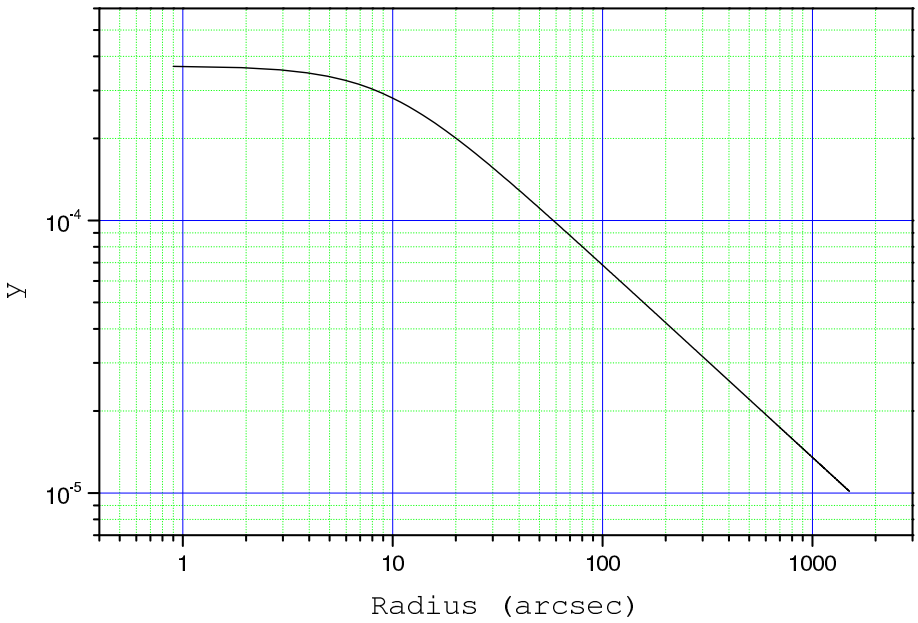

Figure 6.7: Comptonization parameter profile, according to the isothermal β-model, as a function of the radius from the center for the cluster RXC J1023.6+0411.

The y profile derived from the values in Table 6.2 for this cluster is plotted in Fig. 6.7. We apply the same procedure used in last section, i.e. convolution with the beam, and subtraction of the reference (off) signal, shifting the center of observation to include the mentioned offset. The expected Comptonization parameter for our observation mode is $y = 1.2 \cdot 10^{-4}$, in good agreement, within the errors, with that detected.

6.2.3 RXC J1401.0+0252

The highest priority for observation was given to our best candidates, RXC J2228.6+2036 and RXC J1023.6+0411. For this reason, RXC J1401.0+0252 was observed during only a small fraction of the time during which it was visible. Nevetheless, thanks to the high X-ray luminosity and compactness of this cluster, we were able to detect a SZ signal in less than 6000 s of integration (Fig. 6.9). The measured flux density was -1.48 mJy, with a 1 σ random uncertainity of 0.47 mJy and a systematic uncertainity of 7 %, corresponding to a Comptonization of $(1.5 \pm 0.6) \cdot 10^{-4}$. For this cluster, unfortunately, the position offset between observation center andcluster center was relatively large, though still within the cluster. Therefore, the measured value of the SZ decrement is only indicative and could be used for comparison with X-ray observations only after a more detailed analysis.

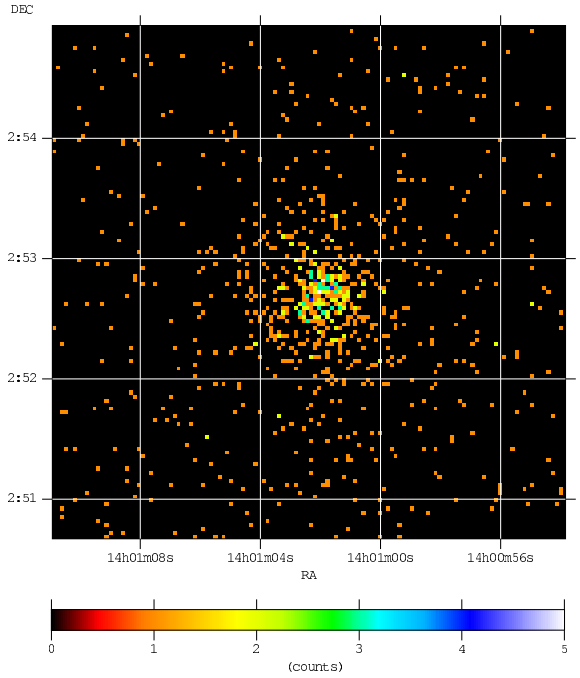

Figure 6.8: ROSAT-HRI image of the inner region of RXC J1401.0+0252. From the Heasarc Data Archive.

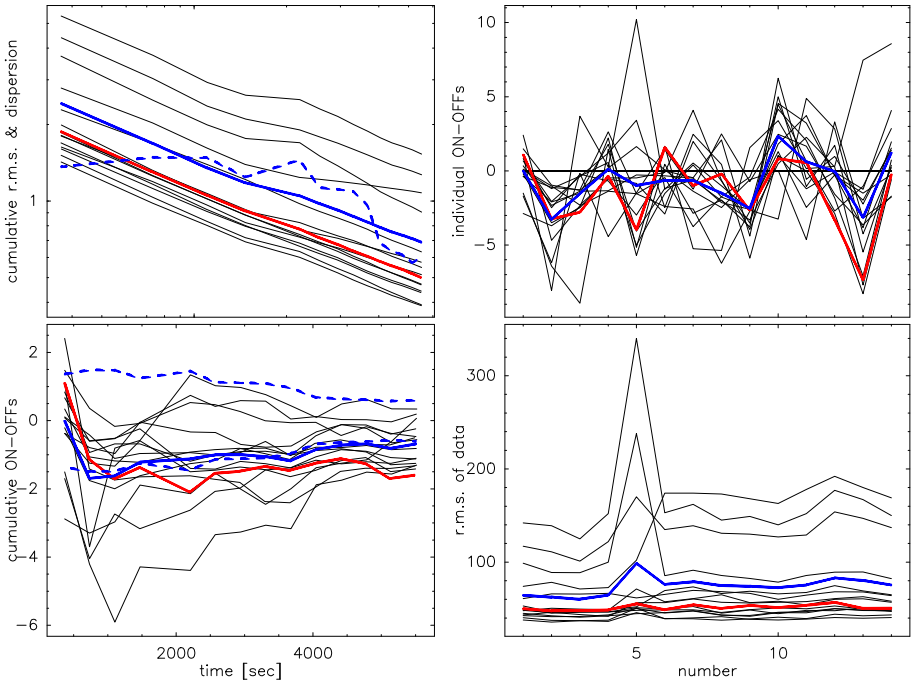

Figure 6.9: Same as Fig. 6.3 for the cluster RXC J1401.0+0252.

6.3 Stars

To test HUMBA on some weak sources, we selected a sample of six stars from the survey at 250 GHz carried out by Altenhoff et al. (1994b). We observed for about 400 s on each star and detected them all. The measured flux densities are given in Table 6.3. We compared our measurements with the values extrapolated using the spectral indeces reported by Altenhoff et al. (1994b). Most of the measured flux densities are in very good agreement with the values extrapolated from 250 GHz, and the only discrepancy is for T Tauri. The value of 1.0 reported by Altenhoff et al. (1994b) for the spectral index

Star	S_{250} mJy	Spectral index	S_{145} mJy (Predicted)	S_{145} mJy (Measured)
Alf Aur	23 ± 4	1.3	12	11 ± 3
Alf Ori	351 ± 25	1.3	173	169 ± 14
HH1 2-1	422 ± 42	2.25 ± 0.10	124	130 ± 11
HL Tau	961 ± 96	2.4	260	240 ± 20
RHO Per	28 ± 3	1.4 ± 0.1	13	14 ± 3
T Tau	296 ± 25	1.0	172	98 ± 9

Table 6.3: Data for a sample of stars selected from Altenhoff et al. (1994b): measured flux at 250 GHz, spectral index, estimated and measured flux at 145 GHz.

of T Tauri was taken from Schwartz et al. (1986), and was based on observations at low-frequency (between 1.4 GHz and 15 GHz). Schwartz et al. suggested that this spectral dependance could come from a modified stellar wind. A later work (Weintraub et al., 1999) reports a spectral index of 2.7 from measurements at submillimeter wavelengths, consistent with the emission expected from cool dust radiating as a blackbody with a frequency-dependent emissivity (Beckwith et al., 1990). Our flux density measurement shows that this spectral behavior continues to 2 mm, if the extended nature of T Tauri is taken into account to extrapolate our flux density to the higher frequencies.

6.4 Pluto

In our observation of Pluto, we measured a flux density of (4.0 ± 1.2) mJy. Altenhoff (2002) provided a theoretical estimate of the expected flux density by applying the rapid rotation model (Altenhoff et al., 1994a) to the system of Pluto and Charon. The predicted flux density at 2 mm is 5.5 mJy, with a large uncerainity due to the poor knowledge of the albedo, which may vary by as much as 20 % and has yet to be obtained by optical measurement. Our measurement agrees with this estimate within the errors.

6.5 Comet C/2000 WM1

The potential of radio and millimeter wavelength continuum detection of comets has been recently demonstrated with the observations of Comets C/1996 B2 (Hyakutake) and C/1995 O1 (Hale-Bopp) (Altenhoff et al., 1999; de Pater et al., 1998; Jewitt & Matthews, 1997, 1999). The interpretation of these observation is complicated, but allows study of the mm-sized ice/dust particles.
We carried out two series of scans on C/2000 WM1, the first in the evening of Nov. 29, and the second in the early morning of Nov. 30. In a total integration time of 4800 s, we measured a signal of 1.98 mJy, with a 1 σ random uncertainity of 0.46 mJy and 7 % of systematic uncertainity. Fig. 6.10 reports the details of the data reduction. This detection has yet to be combined with the observations that where performed at 1.3 mm with MAMBO immediately after the HUMBA campaign, in December 2001, and further interpretation must await that combination.

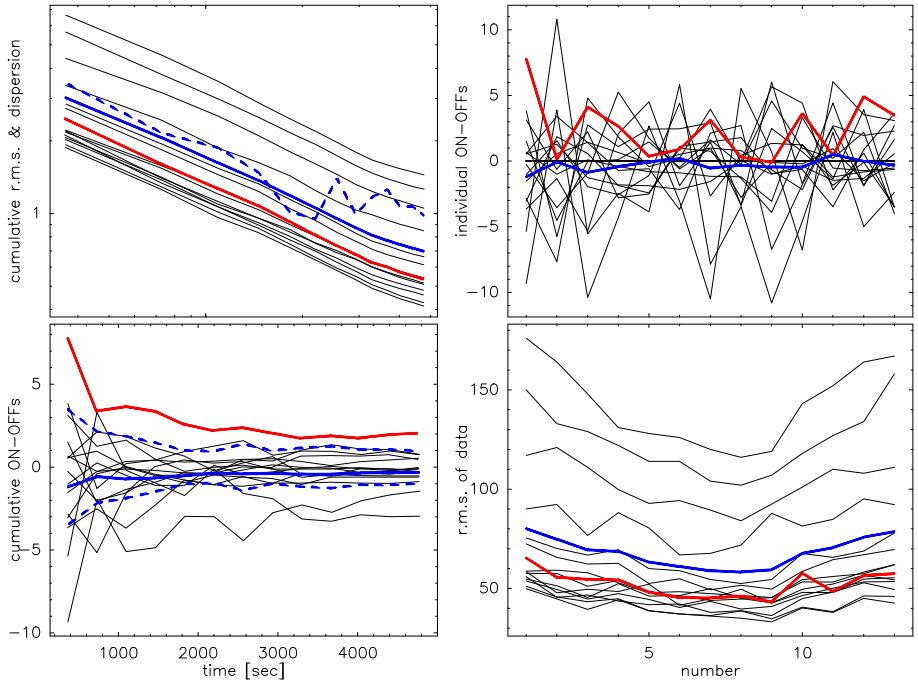

Figure 6.10: Same as Fig. 6.3 for the comet C/2000 WM1.

6.6 Other Objects

When planets are not visible for calibration, it is desirable to have a group of secondary calibrators observable at any LST, i.e. objects with a constant flux density, which can be calibrated against planets. We report in Table 6.4, for future reference, the measured flux densities at 2 mm of some of the secondary calibrators generally used for MAMBO

Source	Flux density (Jy)
Ceph A	1.22 ± 0.09
G 45.1	1.44 ± 0.10
GL 490	0.66 ± 0.05
NGC 7538	3.47 ± 0.25
W3(OH)	4.53 ± 0.32

Table 6.4: Measured flux densities of secondary calibrators.

at 1.3 mm. Also the stars presented in Table 6.3 are suitable for this purpose. Finally, a map of the star-forming region K3-50A is shown in Fig. 6.11 and the measured flux densities of some objects with variable emission (five AGNs and one asteroid) are presented in Table 6.5.

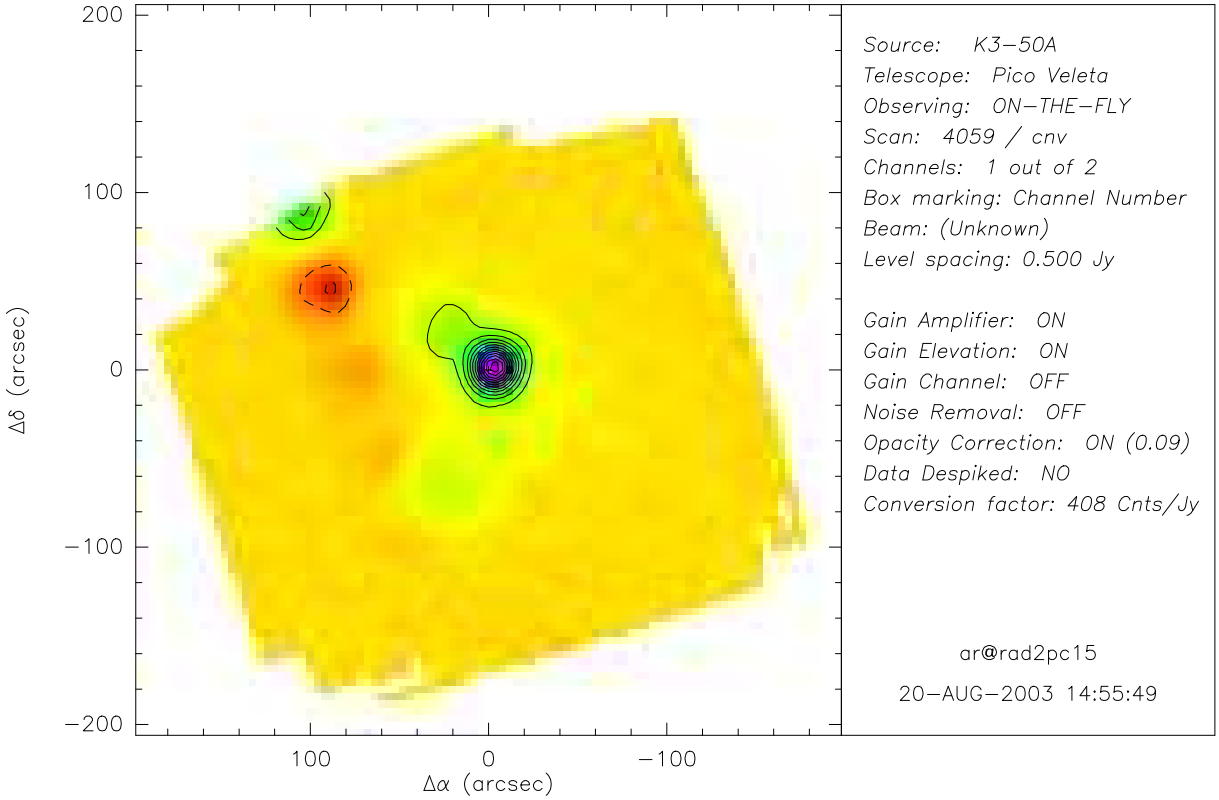

Figure 6.11: On-the-Fly Map of K3-50A. The circular features on the left-side of the source are fake features due to the map being too small and covering only partly the source at the top-left edge.

Source	Flux density(Jy)	JD
1226+023	9.03 ± 0.63	2452241.8815
1253-055	27.4 ± 1.9	2452241.9598
1334-127	4.41 ± 0.34	2452241.8983
1413+135	0.69 ± 0.05	2452242.9170
1510-089	1.15 ± 0.08	2452241.9101
Ceres	0.28 ± 0.02	2452243.1113

Table 6.5: Flux density and Julian day of observation for sources with variable flux density.

Conclusions

High-resolution SZ images offer a powerful tool to investigate clusters of galaxies, and in combination with other types of observations (optical, X-ray, gravitational lensing) allow one to resolve some of the degeneracies between the effects of temperature, density, and depth along the line of sight on the measured signal, all of which are seen projected on the two-dimensional sky.

The Hundred Millikelvin Bolometer Array (HUMBA), built by the Bolometer Development Group of the MPIfR, is a unique instrument devoted to the observation of the SZ effect in the 2 mm band. To operate with background-limited sensitivity even under excellent weather conditions, the system noise is greatly reduced by cooling the bolometers below 100 mK by means of a ^{3}He/^{4}He dilution refrigerator.

HUMBA was first installed and tested at the Heinrich-Hertz-Telescope on Mount Graham, Arizona, in February 1998, and provided first atronomical results in November 1998, including a preliminary detection of SZ effect in the cluster CL0016+16.

The performance of the system was seriously limited by an excess of low-frequency noise in the detectors. This thesis started with the investigation of the nature and the cause of this noise.

The excess of low-frequency noise was found to be correlated with the helium inside the 1 K pot of the dilution unit being superfluid. A microphone installed on the top flange of this pumped helium chamber allowed the noise-generation mechanism to be identified as mechanical vibrations. Different possible sources of vibrations have been investigated. I proved that the vibrations were related to 1 K pot being continuously replenished from the main bath of liquid helium thow a flow impedance. The injection of normal helium (HeI) into the superfluid helium (HeII) bath inside the 1 K pot deposits a large heat load onto a relatively small surface area of HeII. This large heat current locally destroys the superfluid state, which generates turbulence that results in an acoustic vibration of the pot. The mechanical vibrations are transmitted down to the low-temperature stage, where they are converted into heat by the bolometer membrane. The high-frequency temperature variations are integrated by the bolometer. Therefore, the resulting temperature fluctuations appear in the detectors as low-frequency noise. The noise can be eliminated by converting the helium into the superfluid state before introducing it into the 1 K pot. The thermalization of the helium coming from the main bath to the pot temperature, below T_λ, was obtained by means of a heat exchanger internal to the pot.

This work was presented at two international conferences, "9$^{\text{th}}$ International Workshop on Low Temperature Detectors" (July 23-27, 2001) in Madison, Wisconsin, and

"Experimental Cosmology at millimetre wavelengths" (July 9-13, 2001) in Cervinia, Italy. Other groups whose experiments were affected by noise of the same nature became aware of this solution and have implemented it in their systems, providing further evidence of its effectiveness. The improvement to the dilution refrigerators to eliminate this vibrational noise originating in the continuously replenished 1 K pots has been covered by a patent application.

We tested a new array in which the electrical connections to the bolometers were provided by photolithographated niobium wires. The thermal conductance of this array proved to be too low, which overloaded the detectors. I estimated the thermal conductance from load curves to be $1.4 \cdot 10^{-9}$ W/K. The approximations required in the derivation and the uncertainity on the estimate of the optical background power suggested that the thermal conductance could possibly be underestimated. The derived value is a factor of four lower than the theoretical prediction based on values reported in the literature. This could be explained by the mentioned uncertainities or by the different size of our silicon nitride membrane compared to that on which the theoretical prediction was based. Indeed, a larger width of the membrane can result in a residual diffuse phonon scattering that reduces the thermal transmission properties of the silicon nitride.
An old array with electrical connections provided by traditional brass wires has been upgraded from 7 to 19 detectors, and the estimated thermal conductance was close to the optimum value for the assumed optical background conditions.

In late 2001, HUMBA was installed and tested at the IRAM 30 m telescope (MRT) at Pico Veleta. During the first run, from September 28 to October 8, 2001, the goal of having HUMBA installed and operational at the telescope was reached. We demonstrated that the traditional pointing, focus, on-off and on-the-fly mapping modes using the wobbler as well as total power skydips and fast-scanning maps functioned with HUMBA. However, high winds prevented a proper optical alignement using the platform in front of the subreflector. To test HUMBA on weak sources, we had a second campaign during November 23-30, 2001. Installation required a week. During the two days of observations on the sky we measured the beam FWHM to be 19", as expected form diffraction-limited conditions with the 30 m dish. We performed calibrations on planets, and we measured a sensitivity of 34 mJy $s^{1/2}$ and 22 mJy $s^{1/2}$ respectively on the central and on the best channel. The scatter among the sensitivities of the different channels is partly due to the bolometer technology. However, we observed a reduced sensitivity in some of the outer pixels, which was probably due to a problem in the optical system, possibly diffraction on more than one plane.

We observed the three bright, compact clusters of galaxies RXC J2228.6+2036, RXC J1023.6+0411, and RXC J1401.0+0252 and dectected a SZ signal for two of them. Because of the limited time available it was not possible to make maps and we had to observe them in on-off mode. Due to the extent of these sources, this observation mode caused the loss of a fraction of the signal and also forced us to use only the central pixel of the array. For two of the clusters the values of the comptonization parameters derived from the 2 mm data agreed with those derived from existing X-ray data using

an isothermal β-model. We detected the comet C2000/WM1, and the measurement will be combined with the data from MAMBO observations of this comet at 1.3 mm and published later. Observation of Pluto and of a sample of stars gave flux densities that confirmed predicted values. Finally, we measured the 2 mm flux densities of some of the secondary calibrators for future reference.

Before taking HUMBA back to the MRT we plan to test new arrays with photolithographated electrical wires, which would provide more uniform performance among the pixels. To increase the thermal conductance, gold will be used instead of niobium. The behaviour of the optics that caused the decreased sensitivity in some of the outer pixels will also have to be investigated, and if necessary a new lens system will be designed. The FWHM beam of HUMBA matches fairly well the resolution of the X-ray satellite XMM-Newton, which suggests the combination of the observations with these two instrument as a powerful tool to study galaxy clusters. We proposed the observation with XMM of RXC J2228.6+2032, one of our selected clusters, and we plan to image this cluster with HUMBA during the next campaign at the MRT. If we assume that the new array will have a sensitivity equal to that of the best channel during last campaign, i.e. 22 mJy $s^{1/2}$, we estimate that it will be possible to image a region of 180" $\times$ 180" with a sensitivity of 0.3 mJy in 30 hours. Therefore, in four weeks of observations, it would be possible to produce high resolution SZ images of about 15 clusters.

Bibliography

Altenhoff, W. J. 2002, Private communication

Altenhoff, W. J., Bieging, J. H., Butler, B., Butner, H. M., Chini, R., Haslam, C. G. T., Kreysa, E., Martin, R. N., Mauersberger, R., McMullin, J., Muders, D., Peters, W. L., Schmidt, J., Schraml, J. B., Sievers, A., Stumpff, P., Thum, C., von Kap-Herr, A., Wiesemeyer, H., Wink, J. E., & Zylka, R. 1999, A&A, **248**

Altenhoff, W. J., Johnston, K. J., Stumpff, P., & Webster, W. J. 1994a, A&A, **287**, 641

Altenhoff, W. J., Thum, C., & Wendker, H. J. 1994b, A&A, **281**, 161

Andreani, P., Böhringer, H., Dall'Oglio, G., Martinis, L., Shaver, P., Lemke, R., Nyman, L.-A., Booth, R., Pizzo, L., Whyborn, N., Tanaka, Y., & Liang, H. 1999, ApJ, **513**, 23

Andronikashvili, E. 1990, Reflections on liquid helium (AIP)

Baars, J. W. M. 1973, IEEE Transactions on Antennas and Propagation, **Ap-21**, 4

Bartlett, J. G. 2002, in ASP Conf. Ser. 268: Tracing Cosmic Evolution with Galaxy Clusters, 101

Beckwith, S. V. W., Sargent, A. I., Chini, R. S., & Güsten, R. 1990, AJ, **99**, 924

Benford, D. J., Hunter, T. R., & Phillips, T. J. 1998, Int. J. of IR and Millimeter Waves, **19**, 931

Bennemann, K. H. & Ketterson, J. B. 1976, The Physics of liquid and solid Helium (J. Wiley & Sons)

Bennett, C. L., Bay, M., Halpern, M., Hinshaw, G., Jackson, C., Jarosik, N., Kogut, A., Limon, M., Meyer, S. S., Page, L., Spergel, D. N., Tucker, G. S., Wollack, E., & Wright, E. L. 2003a, ApJ, **583**, 1

Bennett, C. L., Halpern, M., Hinshaw, G., Jarosik, N., Kogut, A., Limon, M., Meyer, S. S., Page, L., Spergel, D. N., Tucker, G. S., Wollack, E., Wright, E. L., Barnes, C., Greason, M. R., Hill, R. S., Komatsu, E., Nolta, M. R., Odegard, N., Peirs, H. V., Verde, L., & Weiland, J. L. 2003b, astro-ph/0302207

Berglund, P. 1995, http://na47sun05.cern.ch/target/outline/dilref.html

Bhatia, R. S., Bock, J. J., Ade, P. A. R., Benoit, A., Bradshaw, T. W., Crill, B. P., Griffin, M. J., Hepburn, I. D., Hristov, V. V., Lange, A. E., Mason, P. V., Murray, A. G., Orlowska, A. H., & Turner, A. D. 1999, Cryogenics, **39**, 701

Birkinshaw, M. 1999, Phys. Rep., **310**, 97

Birkinshaw, M., Huges, J. P., & Arnaud, K. A. 1991, ApJ, **379**, 466

Blain, A. W. 1998, MNRAS, **297**, 502

Böhringer, H. 2002, Private communication

Böhringer, H., Voges, W., Huchra, J. P., McLean, B., Giacconi, R., Rosati, P., Burg, R., Mader, J., Schuecker, P., Simiç, D., Komossa, S., Reiprich, T. H., Retzlaff, J., & Trümper, J. 2000, ApJss, **129**, 435

Böringer, H., Hattori, M., Pointecouteau, E., Bertoldi, F. andRaccanelli, A., Schücker, P., & Zhang, Y. 2003, Proposal for XMM-Newton Observations

Broguiére, D., Neri, R., Sievers, A., & Wiesemeyer, H. 1995, IRAM internal report

Bucci, C. 2002, Private communication

Burkert, A. 2003, Private communication

Carli, B. & Iorio Fili, D. 1981, J. Opt. Soc. Am., **71**, 1020

Carlstrom, J. E., Holder, G. P., & Reese, E. D. 2002, ARAA, 40, 643

Casimir, H. 1938, Physica (Amsterdam), **5**, 495

Cavaliere, A. & Fusco-Femiano, R. 1976, A&A, **49**, 137

Clark Jones, R. 1953, J. Opt. Soc. Am., **43**, 1

Conte, R. R. 1970, Éléments de Criogénie (Masson & C.)

Coron, N., Dambier, G., & Leblanc, J. 1971, Infrared Detector Techniques for Space Research (D. Reidel, Dordrecht-Holland), 121

Cryovac GmbH. Heuserweg 14, D-53824, Troisdorf, Germany

de Pater, I., Forster, J. R., Wright, M., Butler, B., Palmer, J. P., Veal, J. M., A'Hearn, M. F., & Snyder, L. E. 1998, AJ, **116**, 987

Doré, O., Bouchet, F. R., Mellier, Y., & Teyssier, R. 2001, A&A, **375**, 14

Downey, P. M., Jeffries, A. D., Meyer, S. S., Weiss, R., Bachner, F. J., Donnelly, J. P., Lindley, W. T., Mountain, R. W., & Silversmith, D. J. 1984, Appl. Opt., **23**, 910

Ebner, C. & Edwards, D. O. 1971, Phys. Rep., **2**, 2

Edge, A. C., Fabian, A. C., Allen, S. W., Crawford, C. S., White, D. A., Böringer, H., & Voges, W. 1994, MNRAS, **270**, L1

Edge, A. C., Stewart, G. C., & Fabian, A. C. 1992, MNRAS, **258**, 177

Fabian, A. C. 1994, ARAA, **32**, 277

Fischer, M. & Lange, A. E. 1993, ApJ, **419**, 433

Fixsen, D. J., Cheng, E. S., Gales, J. M., Mather, J. C., Shafer, R. A., & Wright, E. L. 1996, ApJ, **473**, 576

Gaffney, J. & Clement, J. R. 1955, Rev. Sci. Inst., **26**, 620

GILDAS working group. 1998, IRAM internal report

Grannan, S. M., Lange, A. E., Haller, E. E., & Beeman, J. W. 1992, Phys. Rev. B, **45**, 4516

Grannan, S. M., Richards, P. L., & Hase, M. K. 1997, Int. J. of IR and Millimeter Waves, **18**, 319

Griffin, M. J., Ade, P. A. R., Orton, G. S., Robson, E. I., Gear, W. K., Nolt, I. G., & Radostitz, J. V. 1986, Icarus, **65**, 244

Griffin, M. J. & Holland, W. S. 1988, Int. J. of IR and Millimeter Waves, **9**, 861

Griffin, M. J. & Orton, G. S. 1993, Icarus, **105**, 537

Gromke, J. 2000, PhD thesis, Bonn

Gromke, J., Esch, W., Gemünd, H.-P., Kreysa, E., & Reichertz, L. A. 2001, Nucl. Instr. Meth. Phys. Res., **A444**, 404

Haller & Beeman Assoc. Inc. CA 94803, 5020 Santa Rita Rd., El Sobrante

Haller, E. E., Palaio, N. P., Rodder, M., Hansen, W. L., & Kreysa, E. 1984, Neutron Transmutation Doping of Semiconductor Materials (Plenum Press, New York and London)

Hansen, V. 1998, Private communication

Heasarc Data Archive. http://heasarc.gsfc.nasa.gov/docs/corp/data.html

Hildebrand, R. H., Loewenstein, R. F., Harper, D. A., Orton, G. S., Keene, J., & Whitcomb, S. E. 1985, Icarus, **64**, 64

Holmes, W., Gildemeister, J. M., & Richards, P. L. 1998, Appl. Phys. Lett., **72**, 18

Holzapfel, W. L., Arnaud, M., Ade, P. A. R., Church, S. E., Fischer, M. L., Mauskopf, P. D., Rephaeli, Y., Wilbanks, T. M., & Lange, A. E. 1997, ApJ, **480**, 449

Horowitz, P. & Hill, W. 1989, The art of electronics (Cambridge University Press, Cambridge)

Hoskinson, E. 2002, Private communication

Hristov, V. V. 2001, Signal Processing of NTD-Ge Cryogenic Bolometric Sensors, unpublished.

Huges, J. P. & Birkinshaw, M. 1998, ApJ, **501**, 1

Jewitt, D. C. & Matthews, H. E. 1997, AJ, **113**, 1145

—. 1999, AJ, **117**, 1056

Johnson, J. B. 1928, Phys. Rev., **32**, 97

Kaastra, J. S., Ferrigno, C., Tamura, T., Paerels, F. B. S., Peterson, J. R., & Mittaz, J. P. D. 2001, A&A, **365**, L99

King, I. 1972, ApJ, **174**, L123

Kittel, C. 1958, Elementary Statistical Physics (John Wiley & Sons, Ney York)

—. 1969, Thermal Physics (John Wiley & Sons, Ney York)

Klitsner, T. & Pohl, R. O. 1987, Phys. Rev. B, **36**, 12

Kochfar, S. 2003, PhD thesis, Heidelberg

Komatsu, E., Matsuo, H., Kitayama, T., Hattori, M., Kawabe, R., Kohno, K., Kuno, N., Schindler, S., Suto, Y., & Yoshikawa, K. 2001, PASJ, **53**, 57

Kompaneets, A. S. 1956, Zh. Eksp. Fiz. Teor., **31**, 876

Kreysa, E., Gemünd, H.-P., Raccanelli, A., Reichertz, L. A., & Siringo, G. 2001, in Experimental Cosmology at Millimetre Wawelengths: 2K1BC Workshop (Breuil-Cervinia, Valle d'Aosta, Italy), Vol. 616 (AIP Conference proceedings), 262

Lamarre, J. M. 1986, Appl. Opt., **25**, 870

Lane, C., Fairbank, H., Schultz, H., & Fairbank, W. 1946, Phys. Rev., **70**, 431

—. 1947, Phys. Rev., **71**, 600

Lane, C. T. 1962, Superfluid Physics (McGraw-Hill, New York)

Lawes, G., Zassenhaus, G. M., Koch, S., Smith, E. N., Reppy, J. D., & Parpia, J. M. 1998, Rev. Sci. Inst., **69**, 4176

Leiden Cryogenics B.V. Galgewater n.21, 2311 VZ Leiden, The Netherlands

London, H. 1951, in Proc. Int. Conf. on Low Temp. Phys., Oxford

Lounasmaa, O. V. 1974, Experimental principles and Methods Below 1 K (Academic Press, London)

Low, F. J. 1961, J. Opt. Soc. Am., **51**, 1300

Marten, A., Gautier, D., Owen, T., Sanders, D. B., Matthews, H. E., Atreya, S. K., Tilanus, R. P. J., & Deane, J. R. 1993, ApJ, **406**, 285

Martin, D. H. & Puplett, E. 1969, IR Phys., **10**, 105

Mather, J. C. 1982, Appl. Opt., **21**, 1125

—. 1984a, Appl. Opt., **23**, 584

—. 1984b, Appl. Opt., **23**, 3181

McCarthy, I. G., West, M. J., & Welch, G. A. 2002, ApJ, **567**, 762

Mohr, J. & Majumdar, S. 2003, *AAS*, **202**, 23

Mónzon, J. J. & Sánchez-Soto, L. L. 1994, Appl. Opt, **33**, 5137

Mott, N. F. 1969, Philos. Mag., **19**, 835

Munshi, D., Porciani, C., & Wang, Y. 2003, astro-ph/0302510

Nyquist, H. 1928, Phys. Rev., **32**, 110

Padman, R. & Murphy, J. A. 1991, IR Phys., **31**, 441

Peterson, J. R., Paerels, F. B. S., Kaastra, J. S., Arnaud, M., Reiprich, T. H., Fabian, A. C., Mushotzky, R. F., Jernigan, J. G., & Sakelliou, I. 2001, A&A, **365**, L104

Pirro, S., Alessandrello, A., Brofferio, C., Bucci, C., Cremonesi, O., Coccia, E., Fiorini, E., Fafone, V., Giuliani, A., Nucciotti, A., Pavan, M., Pessina, G., Previtali, E., Vanzini, M., & Zanotti, L. 2001, Nuc. Inst. Meth. Phys. Res., **A444**, 331

Pobell, F. 1996, Matter and Methods at Low Temperatures (Springer-Verlag, Berlin)

Pointecouteau, E., Giard, M., Benoit, A., Désert, F. X., Aghanim, N., Coron, N., Lamarre, J. M., & Delabrouille, J. 1999, ApJ L., **519**, L115

Pointecouteau, E., Hattori, M., Neumann, D., Komatsu, E., Matsuo, H., Kuno, N., & Böhringer, H. 2002, A&A, **387**, 56

Raccanelli, A. 1997, Un criostato a lunga durata per l'esperimento BOOMERanG (A Long Duration Cryostat for the BOOMERanG Experiment), Tesi di Laurea, Roma

—. 1999, Rapporto interno N.265, Te.S.R.E.-C.N.R., Bologna

Raccanelli, A., Reichertz, L. A., & Kreysa, E. 2001a, Cryogenics, **41**, 763

Raccanelli, A., Reichertz, L. A., & Kreysa, E. 2001b, in Ninth International Workshop on Low Tempeature Detectors (Madison, Wisconsin), Vol. 605 (AIP Conference proceedings), 391

Raccanelli, A., Reichertz, L. A., & Kreysa, E. 2001c, in Experimental Cosmology at Millimetre Wawelengths: 2K1BC Workshop (Breuil-Cervinia, Valle d'Aosta, Italy), Vol. 616 (AIP Conference proceedings), 303

—. 2001d, Verfahren und Vorrichtung zur Tieftemperaturkühlung, Deutsche Patentanmeldung **101 30 171.5**

Reese, E. D., Mohr, J. J., Carlstrom, J. E., Joy, M., Grego, L., Holder, G. P., Holzapfel, W. L., Hughes, J. P., Patel, S. K., & Donahue, M. 2000, ApJ, **533**, 38

Reichertz, L. A., Esch, W., Gemünd, H.-P., Gromke, J., & Kreysa, E. 2001a, Nucl. Instr. Meth. Phys. Res., **A444**, 423

Reichertz, L. A., Weferling, B., Esch, W., & Kreysa, E. 2001b, A&A, **379**, 735

Rephaeli, Y. 1995, ARAA, **33**, 541

Richards, P. L. 1994, J. Appl. Phys., **76**, 1

Sarazin, C. L. 1986, Rev. Mod. Phys., **58**, 1

Schwartz, P. R., Simon, T., & Campbell, R. 1986, ApJ, **303**, 233

Simmonds, R. W., Loshak, A., Marchenkov, A., Backhaus, S., Pereversev, S., Vitale, S., Davis, J. C., & Packard, R. E. 1998, Phys. Rev. Lett., **81**, 1247

Sunyaev, R. A. & Zel'dovich, Y. B. 1972, Comm. Astrophys. Space Phys, **4**, 173

Taconis, K. W., Beenakker, J. J. M., & Nier, A. O. C. 1949, Physica, **15**, 733

Tamura, T., Kaastra, J. S., Peterson, J. R., Paerels, F. B. S., Mittaz, J. P. D., Trudolyubov, S. P., Stewart, G., Fabian, A. C., Mushotzky, R. F., Lumb, D. H., & Ikebe, Y. 2001, A&A, **365**, L87

Van der Ziel, A. 1970, Noise (Prentice Hall, New Jersey)

Weintraub, D. A., Sandell, G., Huard, T. L., Kastner, J. H., van den Ancker, M. E., & Waters, R. 1999, ApJ, 517, 819

White, G. K. 1979, Experimental Techniques in Low-Temperature PhYsics (Oxford University Press)

Winston, R. 1970, J. Opt. Soc. Am., **60**, 245

Zhang, P., Murakami, M., Wang, R. Z., & Inaba, H. 1999, Cryogenics, **39**, 609

Zylka, R. 1998, MPIfR internal report

Aknowledgements

This thesis was written at the Max-Planck-Institut für Radioastronomie, in the Bolometer Technology Division of the Millimeter and Submillimeter group. I sincerely thank my advisor, Dr. Ernst Kreysa, and my Referents Prof. Dr. Karl Menten and Prof. Dr. Uli Klein. I really enjoyed the subject of my thesis, which touched on a large range of topics from low temperature physics to galaxy cluster astronomy, and I enjoyed the freedom I had in directing my research.

I am grateful to Prof. Dr. Klaas S. de Boer and to Prof. Dr. Johannes Schmid-Burgk for precious advice and useful suggestions.

For his great support, for having me introduced to the world of dilution refrigeration, for the constant help both in Bonn and from Berkeley, I am most grateful to Dr. Lothar Reichertz, with whom it was a pleasure to work. The friendship with Lothar and Dorothee is one of the greatest gifts I received during my stay in Bonn.

I am grateful to Dr. Hans Boehringer for making himself kindly availabile and for fruitful help on clusters of galaxies and X-ray data analysis, and to Dr. Wilhelm Altenhoff for providing a sample of weak sources for the tests of HUMBA and for the estimate of the flux density of Pluto. I also profited from many useful discussions with Dr. Jürgen Kerp, Prof. Dr. Jean Eilek, Dr. Endrik Krügel and Prof. Dr. Andreas Burkert. I thank Dr. Frank Bertoldi for his help with MOPSI.

I owe quite a bit to Dr. Alan Roy for discussions, advice, help, for proof-reading and commenting my thesis and for his moral support. No words could fully express my gratitude.

I have enjoyed being a member of the Bolometer Division during my doctoral time and would like to thank all members for the friendly working atmosphere. A special thanks to Dr. Hans-Peter Gemünd and to Walter Esch for their help with the research and for their practical assistance with many things.

I thank Dr. Giorgio Siringo for help with the installation of HUMBA at the IRAM 30 m telescope during the first campaign in September 2001, Alessio Medici for promptly providing a solution to most of my problems with LaTeX, and Dr. Johannes Gromke, who worked on HUMBA before me, for discussing some parts of his thesis. A special thanks to Alessandra Bertarini for helping me in many ways since I first moved to Bonn.

Doing a thesis in a Max-Planck Institute and the MPG PhD student network gave me the possibility to meet very interesting people and to start some great friendships. I wish to thank all friends for the great time that we shared and I look forward to work with them on the interesting projects that we started.

Last but not least, thanks a lot to my family, to whom I dedicate this work, for

all their support I received over the years. In particular, I thank my beloved wife and daughter, Laura and Sofia, and I apologize to them for my unbearable mood and for the time I did not devote to them in the last stages of the work.

List of Figures

List of Tables